Institutional Repository - Research Portal
Dépôt Institutionnel - Portail de la Recherche

researchportal.unamur.be

UNIVERSITÉ DE NAMUR

University of Namur

THESIS / THÈSE

DOCTOR OF SCIENCES

Mechanical properties of coatings based on amorphous carbon and metallic glasses

Bagherpour, Alireza

Award date:
2024

Awarding institution:
University of Namur

Link to publication

General rights
Copyright and moral rights for the publications made accessible in the public portal are retained by the authors and/or other copyright owners and it is a condition of accessing publications that users recognise and abide by the legal requirements associated with these rights.

- Users may download and print one copy of any publication from the public portal for the purpose of private study or research.
- You may not further distribute the material or use it for any profit-making activity or commercial gain
- You may freely distribute the URL identifying the publication in the public portal ?

Take down policy
If you believe that this document breaches copyright please contact us providing details, and we will remove access to the work immediately and investigate your claim.

Download date: 28. Apr. 2024

University of Namur – Faculty of Sciences

Namur Institute of Structured matter (NISM)

Mechanical properties of coatings based on amorphous carbon and metallic glasses

Dissertation presented by

Alireza Bagherpour

for the degree of doctor of sciences

Jury members:

Prof. Stéphane LUCAS (Supervisor)
Laboratoire d'Analyse par Réactions Nucléaires (LARN - NISM)
UNamur, Namur, Belgium

Prof. Robert SPORKEN
Namur Institute of Structured Matter (NISM)
UNamur, Namur, Belgium

Prof. Thomas PARDOEN
Institute of Mechanics, Materials and Civil Engineering (IMMC)
UCLouvain, Louvain-la-Neuve, Belgium

Prof. Philippe STEYER
laboratoire de Science des Matériaux (MatéIS)
INSA, Lyon, France

Dr. Andreas PFLUG
Fraunhofer Institute for Surface Engineering and Thin Films (IST)
Braunschweig, Germany

Dr. Matteo GHIDELLI
Laboratoire des Sciences des Procédés et des Matériaux (LSPM)
CNRS, Villetaneuse, France

UNamur - 2024

Science may set limits to knowledge but should not set limits to imagination.

Bertrand Russell

Dedicated to my parents,

I am truly grateful to God for creating selfless parents like you through His mercy. You have been the nurturing roots that allowed me to thrive under the shade of your fruitful existence. From your essence, I have grown branches and leaves, and I strive to learn and acquire knowledge in the shadow of your presence.

Being your child is a crown of honor upon my head, and your name is the reason for my existence. After the Almighty, you have been the source of my being. You took my hand and taught me how to walk in this valley of life, filled with ups and downs.

You have been my teachers, giving meaning to life and humanity for me.

تقدیم به پدر و مادرم

خدای را بسی شاکرم که از روی کرم، پدر و مادری فداکار نسیبم ساخته تا در سایه درخت پربار وجودشان بیاسایم و از ریشه آن‌ها شاخ و برگ گیرم و از سایه وجودشان در راه کسب علم و دانش تلاش نمایم.

والدینی که بودنشان تاج افتخاری است بر سرم و نامشان دلیلی است بر بودنم، چرا که این دو وجود، پس از پروردگار، مایه هستی ام بوده اند دستم را گرفتند و راه رفتن را در این وادی زندگی پر از فراز و نشیب آموختند. آموزگارانی که برایم زندگی و انسان بودن را معنا کردند.

Acknowledgments

First and foremost, I am extremely grateful to my supervisor, Prof. Stéphane LUCAS, for his invaluable advice, continuous support, and patience during my Ph.D. study. His immense knowledge and plentiful experience have encouraged me throughout my academic research and daily life. I would also like to thank Prof. Thomas PARDOEN for his guidance and full support during this time and for the great ideas he gave me to reach my goal in this project.

I will also thank Dr. Marie-Stéphane COLLA, Dr. Paul BARAL, and Dr. Emile HAYE for their great technical and scientific support while performing mechanical tests and analyzing data. To the members of my thesis jury, I would like to sincerely thank you for your time, knowledge, and careful assessment of my work. Your insightful observations and helpful feedback have greatly improved the quality of my thesis. Your commitment to the development of knowledge in this area is much appreciated, and I thank you for it.

I would like to thank all the members of LARN laboratory and my friends for their great support and the joyful moments they made for me during this time. Their kind help and support have made my study and life in Belgium wonderful. I have very special thanks to my friend Razieh, who, without her, I would not overcome the difficult situations I encountered in Belgium at the beginning of my Ph.D. We overcame all our problems and celebrated our success together, even if it was small. I want to thank my colleagues, who were more than colleagues to me and become my family in this country, Essam and Shalini. You really did much for me during this path. Essam THE BOY, you were also my gym bro. Shalini, THE GIRL, I never forget your help while writing my articles and those delicious foods you cooked for Essam and me. Dear Davoud, I am happy that before finishing my Ph.D. I had the chance to know you. Davoud, your bright ideas always make me feel special and someone out of this world. While some may call them "stupid" ideas, but I would like to name them Davoud-type-brilliant-money-maker ideas. We had a great time in Namur and still have much to do bro. I would also like to thank Emile, Negin, Fahime, Fabio, Sajjad, Parisa, Mahsa, Marjan, Tarcius, Tais and Manel for cheering up my life in Belgium and never let me feel alone. Your friendship has been a priceless gift, and I am truly fortunate to have you in my life.

Finally, I would like to thank the most important persons in my life, Maman and Baba, for their unconditional love, support, and encouragement throughout my journey towards completing this doctoral thesis. Their constant trust in my abilities, their sacrifices, and constant presence have been very effective in my academic success. To my sisters, Roza and Rozita, thank you for encouraging me and providing a sense of stability throughout this challenging endeavor. Your encouragement and understanding are invaluable to me. I have special thanks to my partner Zahra for her constant patience,

love, and encouragement during this academic path. From the countless late nights filled with research and writing to the moments of self-doubt and stress, you were there, offering encouragement, a listening ear, and a comforting presence. Your sacrifices, the missed dates, the postponed vacations, and the times when I was preoccupied with my studies do not go unnoticed. Your patience and understanding were a testament to your commitment and love. You were the only one who could make me smile, even during the most stressful times.

پدر و مادر عزیزم به خاطر محبت، حمایت و تشویق بی دریغتان در تمام مراحل زندگی تشکر و قدردانی میکنم. اعتماد همیشگی شما به توانایی های من، فداکاری هایتان و حضور مداومتان برای من بسیار باارزش است. رزا و رزیتای عزیزم که همیشه همراه و پشتیبان من بودید، بدون شما رسیدن به این هدف ممکن نبود.

Abstract

The need to understand the complex behaviors and properties of thin films has made their research an important field in materials science in recent years. Since their mechanical characteristics are so important in determining their usability in a wide range of possible applications, a great deal of study has been dedicated to clarifying them. This calls for a thorough investigation of how they behave in various loading scenarios, including compression, tension, and bending. Moreover, a complex interaction of characteristics such as composition, layer thickness, and deposition parameters has a significant effect on mechanical properties.

One of the main forces behind materials development is the growing need for highly specialized coatings that are suitable for specific industrial applications. The main goal is to empower different sectors by providing customizable coatings that are specifically tailored to their own operating circumstances and requirements. Our study started a thorough investigation with the goal of developing a methodical approach to coating customization, which would go beyond the traditional trial-and-error method, in answer to this critical need.

Despite its crucial significance, fracture—a major failure mode—has surprisingly received comparatively little attention in previous coatings-related research. This thesis thus focuses on coating modification, with special attention to the fracture behavior of two different coating groups.

The first part of this study is to improve our understanding of the mechanical properties of amorphous carbon coatings. Using fracture energy, strength, and stiffness performance indices as primary evaluators, the research carefully adjusts deposition parameters such as bias voltage and deposition pressure. The objective is to engineer coatings exhibiting a targeted critical energy release rate spanning from 5 to 125 J/m² while preserving desirable yield strength (σ_y) (1.6-2.7 GPa) and elastic limits ($^{\sigma_y}/_{E}$) (approximately 0.05) with the tensile strain range between 0.003 and 0.15.

The subsequent phase of this research scrutinizes the fracture behavior of Cu-Zr thin film metallic glasses (TFMGs). Here, through a methodical examination of experimental evidence and meticulous analysis, previously overlooked fracture characteristics are uncovered. Intriguingly, the revelation that even a small amount of oxygen content (as low as 3-4 at.%) during the production of pure metallic glass (MG) films significantly impacts fracture behavior underscores the paramount importance of oxygen content in shaping fracture features.

This Ph.D. thesis aims to further the domains of materials science and surface engineering by providing new insights into the fracture characteristics of amorphous coatings based on amorphous carbon and

metallic glasses. The development of high-performance coatings with modifiable mechanical characteristics and a better comprehension of their fracture behavior under various circumstances might benefit greatly from these findings.

Table of contents

Acknowledgments III

Abstract V

List of Figures XII

List of Tables XVII

Chapter 1 1

1. Introduction 1

1.1. Thin films 2

1.2. Thesis outline 4

Chapter 2. 6

2. Thin film production 6

2.1. Thin film deposition 7

2.1.1. Theory of plasma 8

2.1.2. Sputter deposition 10

2.1.3. Magnetron sputtering 12

2.1.4. Thin film growth mechanism 14

2.2. Summary 17

Chapter 3. 18

3. Amorphous coatings 18

3.1. Introduction to amorphous materials 19

3.1.1. Amorphous carbon 21

3.1.2. Cu-Zr metallic glass 24

3.2. Characterization of amorphous coatings 28

3.2.1. Characterization of a-C coatings 28

3.2.2. Characterization of Cu-Zr thin film metallic glasses........ 30

3.3.Mechanical properties of coatings........ 33

3.3.1. Mechanical properties of a-C coatings 33

3.3.2. Mechanical properties of Cu-Zr based coatings 36

3.4. General comparison of a-C:H and Cu-Zr based thin films 40

3.5. Summary 42

Chapter 4. 43

4. Methodology 43

4.1. Thin film deposition 44

4.1.1. a-C:H:Cr thin film deposition 44

4.1.2. Cu-Zr thin film deposition 45

4.2. Thin film microstructure investigation 47

4.2.1. X-Ray Diffraction (XRD) 47

4.2.2. X-Ray Photoelectron Spectroscopy (XPS) 47

4.2.3. Scanning Electron Microscopy (SEM) 48

4.2.4. Transmission Electron Microscopy (TEM)........ 48

4.2.5. Raman Spectroscopy........ 48

4.2.6. Atomic Force Microscopy (AFM) 48

4.3. Thin film mechanical properties 49

4.3.1. Nanoindentation and micro-scratch test 49

4.3.2. Fracture toughness and crack density 50

Chapter 5. 53

5. Tailoring mechanical properties of a-C:H:Cr coatings 53

Abstract 54

5.1. Introduction 55

5.2. Results 56

5.2.1. Structure, composition and surface morphology 56

5.2.2. Mechanical and tribological properties 61

5.2.2.1. Nano-indentation 61

5.2.2.2. Wear behavior 63

5.2.2.3. Uniaxial tensile tests 66

5.2.2.3.1. In-situ SEM tensile tests 66

5.3. Discussion 68

5.3.1. Effect of process parameters on hardness, Young's modulus, and activation volume 68

5.3.2. Effect of process parameters on wear resistance 69

5.3.3. Effect of process parameters on fracture behavior 70

5.4. Conclusions 72

Chapter 6. 73

6. Vein pattern vs. columnar fracture shape in Cu-Zr thin film metallic glasses: Driving force and mechanism 73

Abstract 74

6.1. Main Text 75

6.2. Conclusion 81

Chapter 7. 82

7. General conclusions 82

Chapter 8. 85

8. Perspectives 85

Chapter 9. 88

9. Annex 88

9.1. Thin film microstructure investigation 89

9.1.1. X-Ray Diffraction (XRD) 89

9.1.2. X-Ray Photoelectron Spectroscopy (XPS) 89

9.1.3. Scanning Electron Microscopy (SEM) 89

9.1.4. Transmission Electron Microscopy (TEM) 90

9.1.5. Raman Spectroscopy 90

9.1.6. Atomic Force Microscopy (AFM) 91

9.2. Thin film mechanical properties 92

9.2.1. Nanoindentation and micro-scratch test 92

9.2.2. Tensile testing on polymer substrate 94

9.3. Additional findings about Cu-Zr TFMGs 95

9.4. In-situ SEM tensile tests 98

Chapter 10. 99

10. References 99

Abbreviations list 126

List of publications 128

Journal articles 129

Conference contributions 129

List of Figures

Figure 1-1. Global industry analysis by type, application, region, key players, and thin film technology forecast (2021-2029) [4]. 2

Figure 1-2. Schematic of the Ph.D. thesis outline. 5

Figure 2-1. Categorization of the primary thin film deposition methods 7

Figure 2-2. Illustration of the sputtering process. The first step listed (I) backscattered and neutralized ions, followed by (II) collisions and implantation, and (III) sputtering. These three mechanisms also produce secondary electron emission [32] 11

Figure 2-3. Schematic presentations of the three regimes of sputtering according to Sigmund [33]. 12

Figure 2-4. The principles of magnetron sputtering (reactive magnetron sputtering). 13

Figure 2-5. Typical thin film growth process (Figure adapted from [38]) 14

Figure 2-6. Illustration of the development mechanisms of thin films and coatings according to (a) Volmer-Weber, (b) Frank-Van Der Merwe, and (c) Stranski-Krastanov on a substrate surface [39]. 15

Figure 2-7. Structure zone model representing the effects of homologous substrate temperature and Ar discharge-gas pressure on the structure of metal films deposited by magnetron sputtering [42]. 17

Figure 3-1. Cooling paths from liquid to solid. Path 1 routes to crystalline structure, and Path 2 and 3 routes to amorphous structure with different cooling rate effects on T_g [50]. 20

Figure 3-2. Carbon allotropes: diamond, graphite, lonsdaleite, C60-fullerene, graphene, amorphous carbon, C540-fullerite, and single-walled carbon nanotube (Figure adapted from [54]). 21

Figure 3-3. Hybridizations of carbon a) sp^3,b) sp^2, and c) sp^1 configuration (Figure adapted from [53]). 22

Figure 3-4. Ternary phase diagram of various amorphous carbon forms (Figure adapted from [57]). 23

Figure 3-5. Binary Cu–Zr MG phase diagram (Figure adapted from [17]). 26

Figure 3-6. Heats of formation values for the Cu–Zr binary system intermetallic compounds [77,84–88]. 27

Figure 3-7. XRD pattern of amorphous carbon (Figure adapted from [93])..29

Figure 3-8. SEM image of (a) top view and (b) cross-section besides (c) AFM image of the a-C film (Figure adapted from [94])..29

Figure 3-9. Raman spectra of a-C film (Figure adapted from [95])..30

Figure 3-10. (a) XRD patterns of the as-deposited Zr–Cu thin films deposited on the glass substrate (b) The equivalent lattice spacing and hump peak position change with the Cu content in Cu-Zr monolithic TFMG (Figure adapted from [63,72])..31

Figure 3-11. The surface morphology (AFM images) and the microstructure in cross-section (SEM images) of (a) the pure Zr film, the Cu-Zr films with (b) 49 at.% and (c) 69 at.% Cu and (d) the pure Cu film deposited at the high power density conditions (Figure adapted from [101]).............................32

Figure 3-12. (a) columnar and (b) vein-like cross-section morphologies of Cu-Zr based TFMGs. 32

Figure 3-13. (a) the hardness of the a-C:H:Cr layers and (b) critical load during scratching (LC1, LC2, and LC3 represent the occurrence of the first microcrack, a significant portion of peeling flake and full coating removal, respectively) as a function of the doping agent (Figure adapted from [43]). 34

Figure 3-14. contour plot of the (a) hardness and (b) Young's modulus plotted against the C_2H_2 flow rate and applied bias voltage (Figure adapted from [108]). 35

Figure 3-15. The hardness of $Cu_{45}Zr_{55}$/Zr nanolayers (red points). $Cu_{45}Zr_{55}$/Cu (black dot-lines with points) as a function of thickness of the Cu or Zr layer. Hardness of nanocrystalline Zr (black dot-lines), $Cu_{45}Zr_{55}$ thin film metallic glass (blue dash-lines), and Cu (orange dash-lines is shown for comparison. The inset shows elastic modulus (*E*) values of Zr (black dot-lines), $Cu_{45}Zr_{55}$ (blue dash-lines), and $Cu_{45}Zr_{55}$/Zr (red points) using the same marker and line style convention as that of the main plot (Figure adapted from [116]). 36

Figure 3-16. Hardness plot for different compositions in the binary Cu–Zr system, extracting at depths of 100, 200, and 300 nm using the Oliver–Pharr method (Figure adapted from [115]). 37

Figure 3-17. (a) SEM image of 10 scratches on CuZr/Zr-40. The red rectangle represents the region of FIB cross-sectioning. (b) 10 penetration depth profiles for CuZr/Zr-40 measured during scratch loading, demonstrating the repeatability of the measurements. (c) Penetration depth profiles for each sample were measured during scratch loading. The inset at the top right shows the residual scratch depths, as measured by AFM at ~20-μm intervals along selected scratches. (d, e) Scratch track profiles were

measured by AFM on selected scratches at locations of 250 mN and 400 mN loading, respectively. (c–e) have the same color coding (Figure adapted from [116]). 38

Figure 3-18. Typical load versus deflection curves of each microcantilever (Figure adapted from [123]). 39

Figure 3-19. The materials property map presents the elastic limit against the critical energy release rate. The results are obtained from the literature where a-C are shown with blue dot lines and Cu-Zr based metallic glasses with red dot lines [114,127,148–162]. 41

Figure 4-1. Schematic of the deposition process for a-C:H:Cr film deposition with magnetron coater. 45

Figure 4-2. Schematic of the (a) magnetron sputtering and (b) reactive magnetron sputtering process for Cu-Zr film deposition. 46

Figure 4-3. Specimen geometry for tensile testing of a-C:H:Cr films on kapton. 50

Figure 5-1. XRD pattern of the as-deposited amorphous films with different deposition conditions. The inset shows the high resolution TEM micrograph and a diffraction pattern typical of amorphous film. 57

Figure 5-2. (a) Raman spectra of the a-C:H:Cr films. (b) Variation of the I_D/I_G intensity ratio and the G peak positions under different deposition conditions. 58

Figure 5-3. Chemical composition obtained by XPS depth profiling as a function of the film thickness for a) 5 mTorr / floating and b) 5 mTorr / -100V, c) 20 mTorr / floating, and d) 20 mTorr / -100V conditions. 59

Figure 5-4. AFM images of a-C:H:Cr films a) 5 mTorr / floating, b) 5 mTorr / -100V, c) 20 mTorr / floating, and d) 20 mTorr / -100V. 60

Figure 5-5. SEM micrographs on top views and cross-sections of a-C:H:Cr films: a) 5 mTorr / floating, b) 5 mTorr / -100V, c) 20 mTorr / floating and d) 20 mTorr / -100V. 61

Figure 5-6. Comparison of the performance indices: $\sigma y E'$ and $\sigma y 3 E' 2$ for the four conditions investigated in this study. The error bars represent the standard deviation calculated over 16 experiments. 62

Figure 5-7. Effect of the deposition parameters on the physical activation volume and associated number of atomic sites of a-C:H:Cr thin film. 63

Figure 5-8. Results from the nanoscratch tests: (a) typical scratch profile with the displacement during loading as a black plain line and the profile of the wear track after loading in a dashed black line. The black arrow indicates the location of the critical load; (b) variation of the elastic recovery as a function of the sliding distance; (c) average critical load measured for each coating, error bars indicate the standard deviation; (d) variation of the coefficient of friction as a function of the sliding distance. ... 64

Figure 5-9. Typical wear track after nano-scratch testing of (a) 5 mTorr / floating, (b) 5 mTorr / -100 V, (c) 20 mTorr / floating, (d) 20 mTorr / -100 V. The white arrows indicate the location of the critical load. The blue box highlights in (e) the formation of a chip just after the critical load on a 5 mTorr / -100 V sample. The red box displays in (f) the crack features of the chip. The dashed white lines highlight the step-like pattern produced during the formation of the chip. 65

Figure 5-10. (a-d) Evolution of crack density with in-situ strain for different samples (e) typical high magnification SEM top-view observation of a crack. 67

Figure 5-11. Materials property map presenting the ratio yield strength over Young's modulus against critical energy release rate. The results are obtained from the literature and compared to the four a-C:H:Cr thin films produced in this study [114,127,148–162]. 71

Figure 6-1. Schematic representation of the crack propagation configuration for Cu-Zr TFMGs deposited on the Si wafer with two different patterns observed by SEM. The loading configuration resembles a three-point bending test. 75

Figure 6-2. (a,b) cross-sectional SEM micrograph of the columnar and vein-like patterns simultaneously in two samples deposited in different conditions with the (c,d) same initial columnar growth evident on the top-view. 76

Figure 6-3. a) SEM micrograph of columnar / vein pattern, and b) XPS graph integrated with SEM cross-section as proof of oxygen influence on fracture shape. 78

Figure 6-4. (a) XRD analysis of amorphous Cu-Zr TFMGs and SEM topography of b) 5 mTorr/floating, c) 5 mTorr/-100V, d) 20 mTorr/floating, e) 20 mTorr/-100V with XPS analysis inset to the figs....... 80

Figure 6-5. (a) XRD analysis of amorphous Cu-Zr TFMGs and SEM topography of (b) 0 sccm, (c) 3 sccm, (d) 5 sccm, (e) 7 sccm, with XPS analysis inset to the figs. 80

Figure 9-1. Diagram of the Rayleigh and Raman scattering processes [271]. 91

Figure 9-2. Schematic of an atomic force microscope with (I) laser beam reflected by a cantilever, (II) position sensitive photodetector to measure the deflection, (III) piezoelectric scanner to position the sample with Å accuracy, (IV) sample's Z-axis controller [273]. 92

Figure 9-3. The schematic of a load-displacement curve for indentation [69]. 93

Figure 9-4. Stress-Strain diagram. 94

Figure 9-5. SEM micrograph of multilayered Cu-Zr TFMG with and without oxygen. 95

Figure 9-6. Conversion of (a) columnar fracture patterns to (b) vein-like feature after laser treatment. (c) shows higher magnification of the fracture cross-section with vein patterns. 97

Figure 9-7. Fragmentation mechanism of a-C:H:Cr films on polymer substrate during tensile testing. 98

List of Tables

Table 2-1. Typical processes occur in low-temperature plasmas [30]. 9

Table 3-1. Comparison of major properties of amorphous carbons with those of reference materials: diamond, graphite [57]. 24

Table 3-2. Crystal structures of phases in the binary Cu–Zr system [77]. 27

Table 5-1. a-C:H:Cr films mean column diameter and surface RMS roughness measured by AFM. 60

Table 5-2. Nano-indentation and micro-scratch related results: hardness, Young's modulus, resistance to plastic deformation, wear resistance, and critical load values for different deposition conditions. 66

Table 5-3. Traction related results: Fracture strain and stress, Saturation crack density at 1mm of crosshead displacement, critical fracture energy release rate, fracture toughness, and fracture plastic zone size values for different deposition conditions. 68

Table 5-4. a-C:H:Cr films deposited by PECVD method with CH_4 and C_2H_2 precursor gases or graphite target and nano-indentation results in comparison with recent work 70

Table 9-1. Comparison in mechanical properties of single layer (SL) and multilayer (ML) with and without oxygen injection during the deposition process. (a) SL0 (b) SL3, and (c) ML0/3. 96

Table 9-2. Comparison in fracture behavior of single layer (SL) and multilayer (ML) with and without oxygen injection during deposition. (a) SL0 (b) SL3, and (c) ML0/3 extracted from vein patterns width. 96

Table 9-3. Comparison of fracture toughness and fracture energy release rate. 96

Chapter 1.

1. Introduction

This first chapter gives a general overview of the importance of coatings technology in different industries, together with the significant need for customizable coatings. Moreover, it will discuss the advantages of amorphous coatings and our motivation in pursuing this study.

1.1. Thin films

Given the potential for reducing component size and increasing efficiency, especially in high-tech applications, the use of thin-film technology has emerged as the main method of manufacturing these thin layers ranging from sub-nanometers to several micrometers thick. They have become the material of choice for a multitude of purposes, including but not limited to hard coatings, decorative elements, electrical devices, and optical coatings [1,2]. One of the unique features of thin films lies in their capability to be applied in extremely thin layers. This characteristic enables the creation of lightweight and compact components, aligning perfectly with the prevailing trend toward smaller and more streamlined devices. The ability to maintain functionality while reducing size is particularly advantageous and meets the ever-growing demand for portable and space-efficient technologies. Thin film technology, therefore, not only meets the requirements of current industries but also aligns seamlessly with the evolving preferences in the design and functionality of modern devices [3].

Figure 1-1 shows the key players in the thin films industry and the future perspective of the dramatic increase in thin film's market share from 2021 to 2029, whereby 2029, it is expected that thin films will play a major role in electronics and military and defense fields.

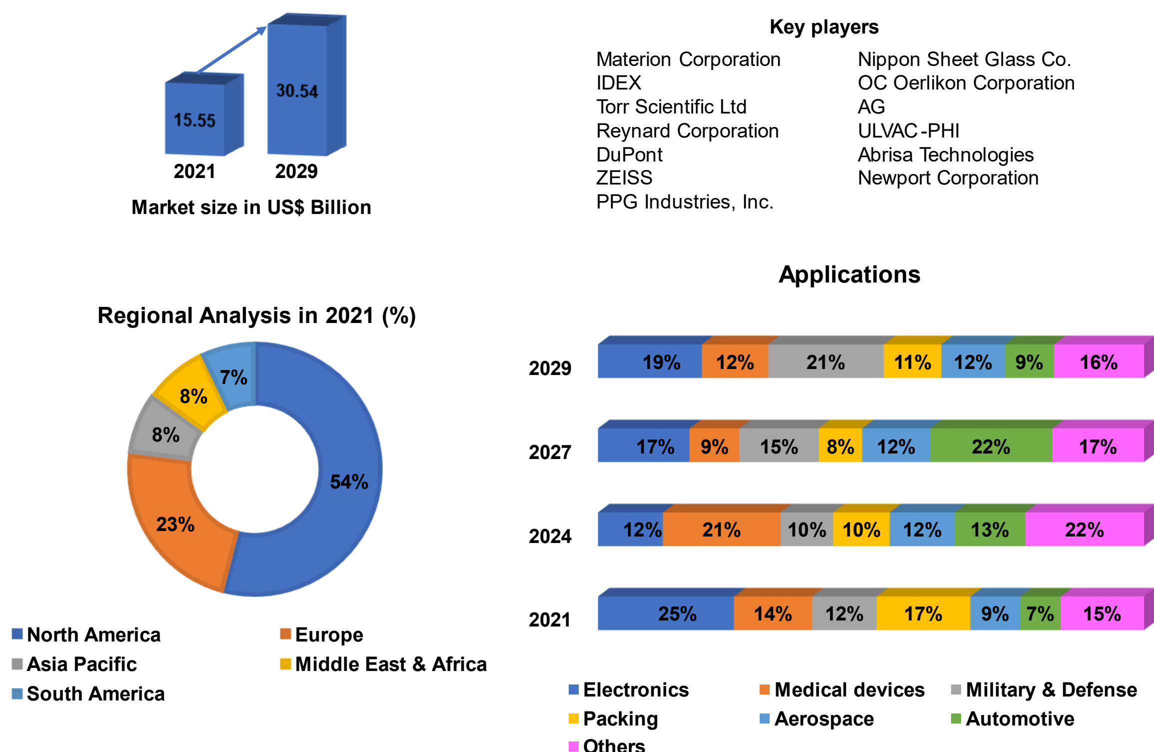

Figure 1-1. Global industry analysis by type, application, region, key players, and thin film technology forecast (2021-2029) [4].

One of the most amazing aspects of thin films is how precisely their properties may be altered. Engineers can precisely tailor properties such as mechanical strength, optical properties, and electrical conductivity, making customizable coatings invaluable for personalized solutions, enhancing aesthetics, satisfying environmental regulations, improving manufacturing efficiency, and product protection. It also encourages sustainability and complies with industry norms [5–7]. This ensures compatibility, prevents problems like stress-induced deformation or fracture in integrated circuits and magnetic disks, and increases electronic components' tensile strength and reliability where performance is important due to their flexibility to be modified [8–11].

While different methods, such as material selection, thickness adjustment, compositional change, nanostructuring, heat treatment, etc., can modify the coatings' mechanical characteristics [11], they may be expensive, time-consuming, and inaccurate. For example, when a coating's composition or material is altered, there may occasionally be issues with compatibility with the substrate or other components of the system. On the other hand, heat treatment is not a good option for all types of coatings; for instance, in amorphous coatings, getting out of the glass transition temperature range (T_g) will result in the transition from a rigid state to a more mobile or rubbery state or exceeding the onset temperature of crystallization (T_x) will result in recrystallization of the coating and losing the desired properties. In order to achieve the necessary coating qualities, fine-tuning deposition parameters stands out as a more precise, effective, and adaptable strategy [12].

Recent scientific focus has shifted towards amorphous coatings over conventional alloy coatings due to their ability to be used in severe environments with high friction and wear as well as high corrosive conditions like acid and alkali. Thus, these coatings possess high hardness (4 to 24 GPa), wear resistance ($<20 \times 10^{-6}$ mm^3/Nm), and corrosion resistance (0.1 μm/year to 10 μm/year) as the protective layer of the substrate due to the lack of crystalline defects like grain boundaries and dislocations, which are vulnerable to corrosion [13–16].

This thesis aims to conduct an extensive investigation into two distinct categories of amorphous coatings, delineating their structural compositions: one resembling polymers and the other exhibiting characteristics akin to metallic and glassy materials. Building upon foundational research that highlighted the significance of hydrogenated amorphous carbon (a-C:H) and Cu-Zr thin film metallic glasses (TFMGs) [17–25], this study endeavors to delve profoundly into their intricate nuances.

Previous research has offered some insight into thin-film mechanical characteristics. Nevertheless, significant deficiencies remain with respect to the well-informed choice of coatings determined by critical indices and a thorough understanding of the complex microstructural details and fracture mechanics included in these coatings. Therefore, this investigation's main scientific goal is to

comprehend the complex interactions between controlled oxidation processes, precursor gas manipulation, and deposition conditions that influence the fracture behavior of these amorphous coatings.

To address this critical question, a multifaceted approach integrating meticulous experimentation and advanced characterization techniques will be employed. The focal point lies in exploring a broad spectrum of deposition parameters such as substrate biasing, precursor gas flow, and deposition pressure. This systematic manipulation aims to unravel their direct influence on the resultant microstructure and subsequent fracture behavior when subjected to varied loading conditions.

Furthermore, the goal of this research is to clearly identify relationships between particular deposition parameters and the mechanical characteristics that emerge. Through a detailed analysis of these underlying mechanisms, our research hopes to provide both theoretical and practical insights that can guide the strategic engineering and design of very durable, application-specific coatings that meet a range of industrial needs.

By means of this detailed research, a more clear path for the systematic design and optimization of amorphous coatings is to be established, perhaps leading to an advancement in the field of material engineering. The objective of this work is to provide the market with customized materials that exhibit improved mechanical performance and durability, therefore satisfying the requirements of a wide range of applications and operating situations.

1.2. Thesis outline

The schematic of the thesis' structure is shown in Figure 1-2, which will be followed in this thesis. Main deposition methods along with the necessary introduction of plasma coating and thin film growth, are discussed in Chapter 2. The basics of amorphous coatings and their characterization are discussed and compared in Chapter 3. Chapter 4 delves into the primary experimental methodologies employed for assessing coatings. Using the introduced methodology, Chapter 5 and Chapter 6 present novel approaches to tailor the mechanical properties of a-C:H:Cr coatings to answer the specific applications' needs and the novel approach to deeply understanding the driving force and mechanism causing the vein patterns and columnar fracture shape in Cu-Zr thin film metallic glasses, respectively. Finally, the general conclusions of this work are summarized in Chapter 7, and future prospects have been mentioned in Chapter 8.

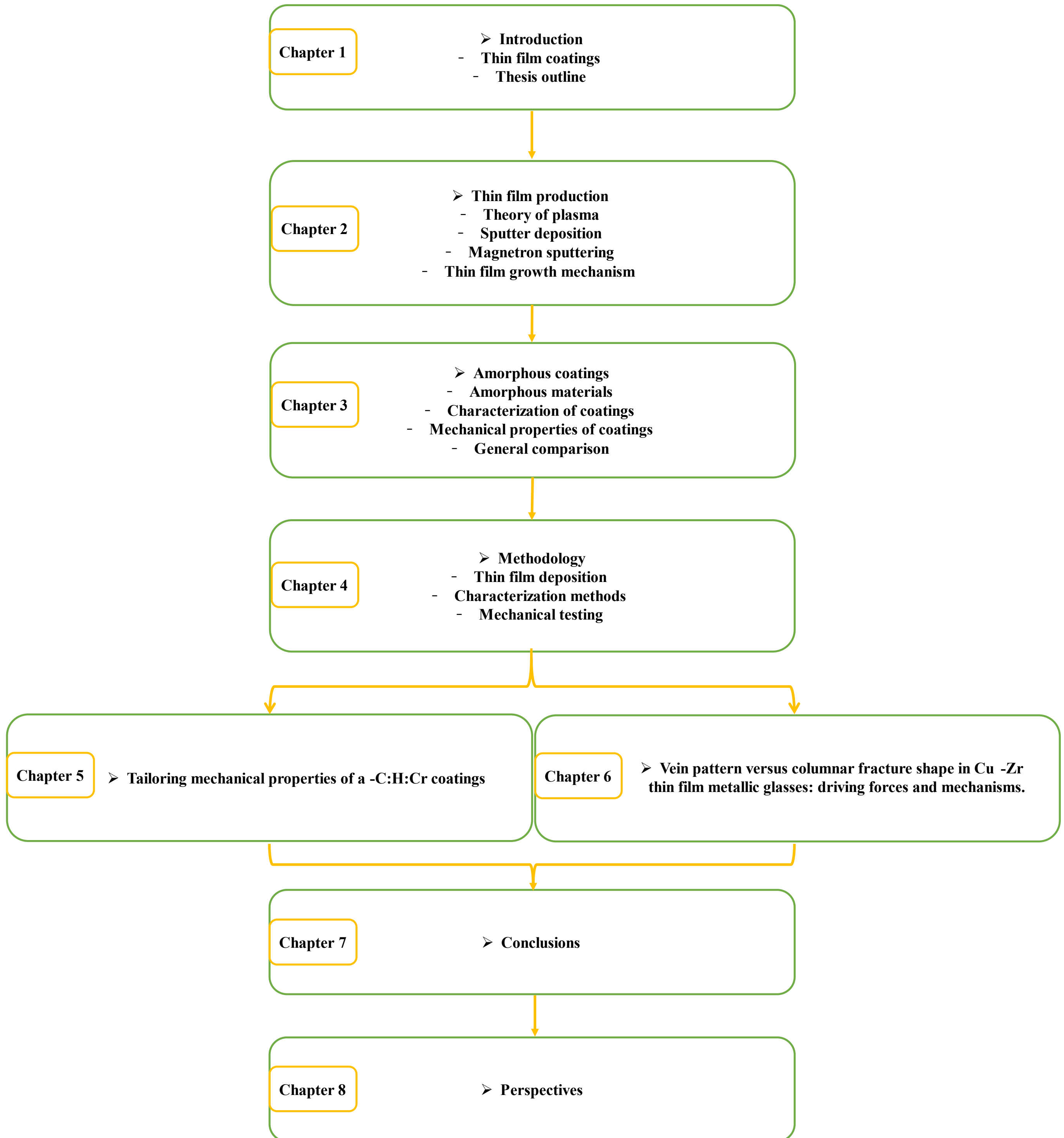

Figure 1-2. Schematic of the Ph.D. thesis outline.

Chapter 2.

2. Thin film production

This chapter focuses on the thin film deposition technique that has been used in this study and gives a general overview of the basics of plasma deposition and thin film growth mechanism.

2.1. Thin film deposition

Thin film deposition techniques are usually sorted out into two prominent families: wet or dry. Typical deposition methods of thin films are shown in Figure 2-1.

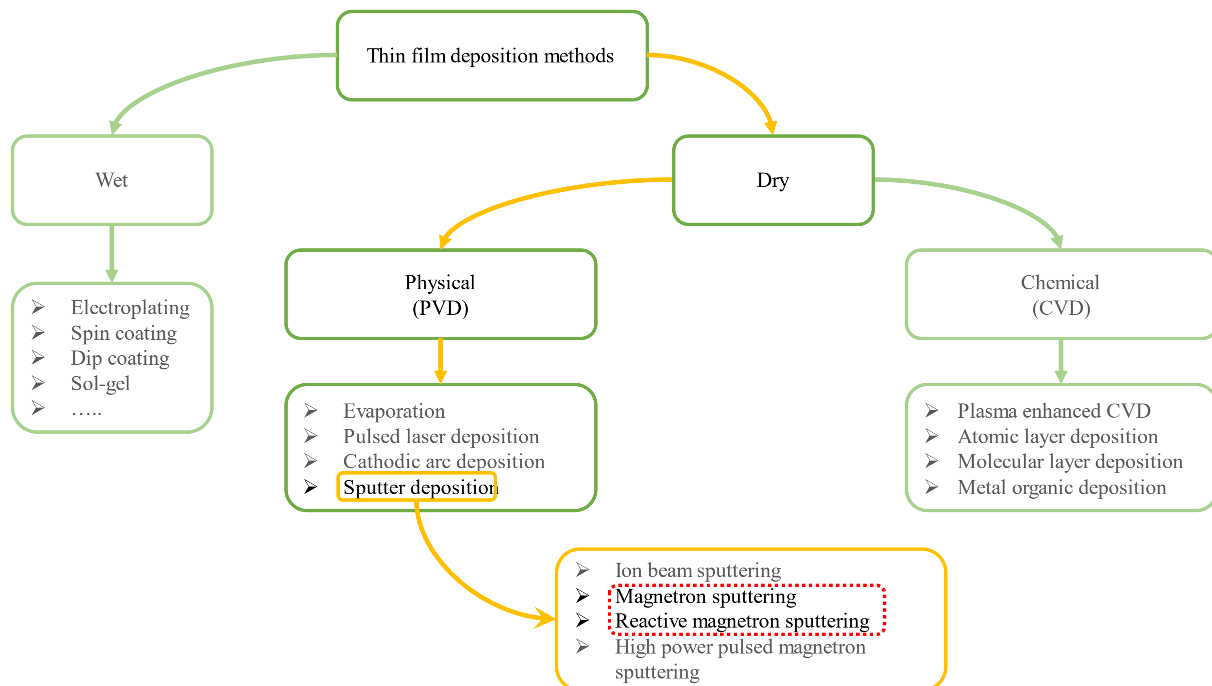

Figure 2-1. Categorization of the primary thin film deposition methods.

In a wet deposition, a liquid solvent coats the surface. In this method, a fluid precursor undergoes chemical reactions at the substrate's surface to produce a solid layer. Electroplating is one of these methods. It includes immersing the item to be plated, also known as inserting the substrate in a solution that contains the metal ions that will be deposited. On the other hand, spin coating involves applying a small quantity of coating material to the substrate's center and rotating it quickly afterward. A thin, uniform coating of liquid is created on the surface of the substrate thanks to centrifugal force. In dip coating, a substrate is submerged into a liquid solution or suspension containing the appropriate coating material. Sol-gel is another sub-technique in the wet deposition method that involves dissolving metal alkoxides or other precursors in a solvent, usually water or alcohol. The sol changes into a gel by the processes of hydrolysis and condensation, and more heating will solidify the gel [26].

In contrast to wet deposition, the dry deposition techniques include methods that utilize the coating material in a vapor phase. By operating under a vacuum, which reduces the quantity of impurities, these techniques lead to improved regulation of the coating composition. There are two basic categories into which dry deposition methods can be divided. Chemical vapor deposition (CVD) methods encompass a suite of techniques where precursor gases containing the source material are introduced into a

specialized reactor. Within this controlled environment, these precursor gases come into contact with the substrate surface. Through chemical reactions or decomposition triggered by heat or other energy sources, these gases break down, depositing the desired material onto the substrate in a controlled manner. However, one particular kind of CVD method that involves the production of a plasma from the interacting gases is called plasma-enhanced chemical vapor deposition, or PECVD. In addition to depositing the thin films from a gas state into a solid, this plasma causes chemical processes that assist eliminate impurities, improving the mechanical and electrical qualities of the film. Fast deposition rates may be achieved using PECVD without sacrificing film quality [27].

On the other hand, physical vapor deposition (PVD) operates on a different principle. It involves the vaporization of a solid or liquid source material into individual atoms or molecules. This vaporized material then traverses through a vacuum or low-pressure gaseous environment to reach the substrate. Upon reaching the substrate surface, the vapor condenses, forming a thin film or coating. PVD processes, such as evaporation or sputtering, rely on physical mechanisms rather than chemical reactions to deposit material onto the substrate. According to the technique used to evaporate the source material, such as heating (evaporation) or ion bombardment (sputtering), the PVD process may also be divided into subcategories. Both the vapor transfer from the source material to the substrate and the deposition process (vapor condensation) are physical processes that entail little to no chemical interactions [26]. The PVD process will be the main focus of this study, with a specific emphasis on the sputtering technique since it allows for better control during the film deposition and can operate under vacuum, which reduces the amount of contaminants.

2.1.1. Theory of plasma

Plasma, often referred to as the fourth state of matter, is an ionized gas consisting of a collection of free electrons, positive ions, neutral atoms, and molecules. Plasma has a quasi-neutral state, which means that while charges may build locally, the plasma is neutral globally. Various methods can generate plasma, including thermal ionization, electrical discharges, and electromagnetic radiation.

Several parameters characterize the behavior of plasma:

Electron Density (n_e): It represents the number of free electrons per unit volume and is typically expressed in units of cm^{-3}. Electron density plays a vital role in determining the plasma's conductivity and other electrical properties.

Electron Temperature (T_e): It is related to the average kinetic energy of electrons in the plasma. The electron temperature determines the degree of ionization and influences the energy transfer processes within the plasma.

Ion Density (n_i): The ion density affects the rate of ionization and recombination processes.

Ion Temperature (T_i): The ion temperature influences the energy distribution of ions.

Plasma Frequency (ω_p): It describes the characteristic frequency at which charged particles oscillate in the plasma. The equation gives the plasma frequency [28]:

$$\omega_p = \sqrt{n_e \,.\, e^2 \,/\, (\varepsilon_0 \,.\, m_e)}\,, \qquad \text{[Hz]} \qquad (2\text{-}1)$$

where e is the elementary charge, ε_0 is the vacuum permittivity[1] (8.854 × 10^{-12} farads per meter) and m_e is the electron mass.

Debye Length (λ_D): It represents the spatial scale over which the electrical potential in the plasma changes significantly. The Debye length is given by [29]:

$$\lambda_D = \sqrt{(\varepsilon_0 \,.\, k \,.\, T_e) \,/\, (n_e \,.\, e)}, \qquad \text{[m]} \qquad (2\text{-}2)$$

where k is Boltzmann's constant.

The processes of plasma-internal collisions are described in Table 2-1. It's noteworthy to observe that the second reaction causes atom A to be excited before going through a process of photon emission to return to its ground state. Thus, the plasma emits light that can be seen, and the energy of the photon relies on the atomic energy levels to reveal the composition of the plasma [30].

Table 2-1. Typical processes occur in low-temperature plasmas [30].

Electrons	
1.Ionization	$e^- + A \rightarrow A^+ + 2e^-$
2.Excitation	$e^- + A \rightarrow A^* + e^-$
3.Penning ionization	$e^- + A^* \rightarrow A^+ + 2e^-$
4.Elastic collision	$e^- + A \rightarrow e^- + A$
5.Dissociation	$e^- + A_2 \rightarrow e^- + 2A$
6.Dissociative ionization	$e^- + A_2 \rightarrow 2e^- + A^+ + A$

[1] The vacuum's ability to permit the electric field.

7.Dissociative attachment	$e^- + A_2 \rightarrow A^- + A$
8.Dissociative recombination	$e^- + A_2^+ \rightarrow A + A$
Ions	
1.Charge exchange	$A^+ + B \rightarrow A + B^+$
2.Elastic collision	$A^+ + B \rightarrow A^+ + B$
3.Ionization	$A^+ + B \rightarrow A^+ + B^+ + e^-$
4.Recombination	$e^- + A^+ + B \rightarrow A + B$
5.Dissociation	$A^+ + BC \rightarrow A + B + C$
6.Chemical reaction	$A + BC \rightarrow AB + C$

2.1.2. Sputter deposition

A well-known thin film deposition method is sputter deposition. Commercially, it is utilized for larger-scale manufacturing since it can create homogenous films on surfaces up to several square meters in size. Vacuum requirements, line-of-sight deposition, and challenges in growing films thicker than a few micrometers can all be disadvantages for specific applications.

Different steps for thin film deposition by this method are as follows [31]:

1) Target material: The target material (cathode) is mounted such that it faces the substrate.
2) Vacuum pumping: In order to create a high vacuum environment, the chamber pumps down to low pressure (10^{-7} Torr) using a vacuum pump.
3) Introduction of inert gas: Argon gas as an inert gas is introduced into the deposition chamber as the sputtering medium.
4) Reactive gas atmosphere: In reactive sputtering, a reactive gas (e.g., oxygen, nitrogen, or a halogen gas) is introduced into the sputtering chamber in controlled amounts. This reactive gas is typically at a lower pressure than the inert sputtering gas, but its presence is essential for the chemical reaction.
5) Plasma generation: A high voltage (a few hundred volts to several kilovolts) is applied to the cathode to overcome the Ar ionization energy (15.76 eV). Since the mass of ions is at least 1000 times more than that of electrons, the energy is mostly transferred to electrons. Ions' temperature (T_i) is low, around 0.025 eV, and they rapidly exchange energy with the background gas. On the other hand, electrons have a higher temperature (T_e) of around 1 eV which is sufficient to ionize and dissociate

molecules in the plasma. As a result of the temperature differential between electrons and ions ($T_e \gg T_i$) the plasma is called "cold" or "non-equilibrium plasma.

6) Sputtering: As the energetic Ar^+ collides with the target material, atoms will be ejected from a cathode during the physical sputtering process due to impinging energetic particles. In reactive sputtering, the electric field accelerates electrons in the plasma, leading to increased collisions near the target material and high ionization. (I) Ions may backscatter after being neutralized or (II) produce a series of collisions prior to being implanted. (III) Due to this series of collisions, some target atoms may sputter. The sputtering process can be seen in Figure 2-2.

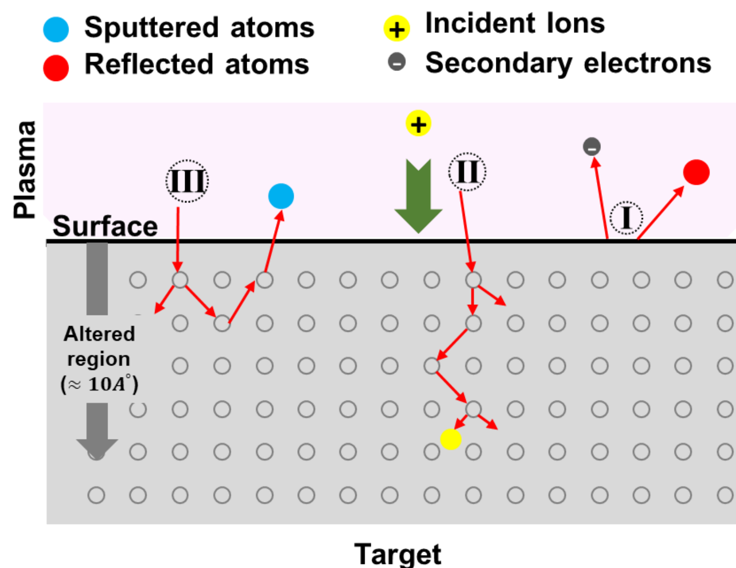

Figure 2-2. Illustration of the sputtering process. The first step listed (I) backscattered and neutralized ions, followed by (II) collisions and implantation, and (III) sputtering. These three mechanisms also produce secondary electron emission [32]

The most significant result of an ion entering a target surface is the development of a collision cascade, where elastic collisions between the energetic ion and the target atoms characterize the scattering process. Three distinct regimes may be distinguished based on the incoming ion's energy. A single knock-on regime happens for low-energy Ar ions (<100 eV). In this scenario, the energy of the initial recoils is insufficient to produce subsequent recoils. The initial knock-on recoil at intermediate Ar^+ energy (~300 eV) causes secondary recoils, which in turn will cause many collisions. A small portion of the recoils are spread towards the target surface, while the majority are diffused further into the target. Recoils can depart the target and be sputtered if they are close to the surface and have enough energy to break through the surface-binding energy barrier. In the spike regime, the rebound density is sufficiently high during sputtering with heavy and/or energetic ions (>10 keV to a few MeV) that atom

collisions are possible. However, the linear cascade regime predominates since the Ar^+ energy is generally in the range of 400 eV during DC magnetron sputtering [33].

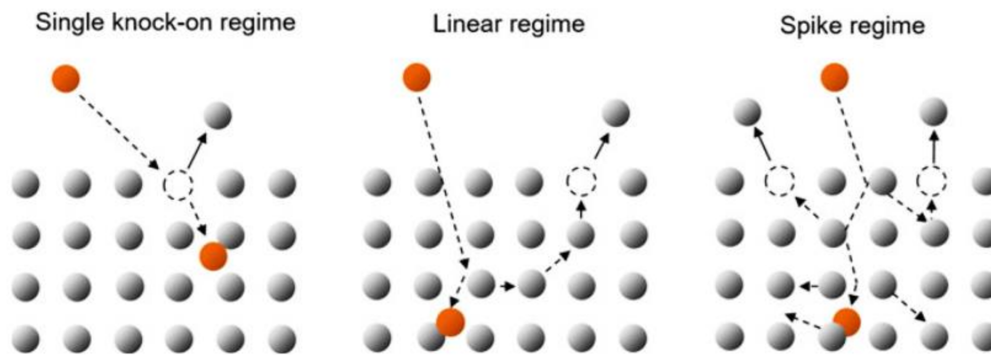

Figure 2-3. Schematic presentations of the three regimes of sputtering according to Sigmund [33].

7) Film deposition: In pure metallic film deposition, the ejected particles from the target material deposit onto the substrate, forming a thin film. In reactive magnetron sputtering, chemically active species react with the sputtered target atoms, forming compounds. For example, in the case of reactive sputtering with oxygen, metal atoms from the target combine with oxygen ions to form metal oxides, and then deposited species adhere to the substrate, forming a thin film with the desired composition. The film thickness and other properties can be controlled by adjusting the sputtering parameters, such as the target voltage, gas pressure, and substrate temperature.

2.1.3. Magnetron sputtering

Due to its industrial scalability, high deposition rate, material purity, repeatability, and strong coating adherence, magnetron sputtering (reactive magnetron sputtering) is the method that we utilize in this thesis. The low ionization efficiency of the secondary electrons in a traditional sputtering system is a serious issue since it necessitates high process pressure and high target voltage. A poor deposition rate is caused by the low ion production, which is further decreased by losses to the surrounding surfaces (through gas phase scattering due to the high pressure). This issue is mostly resolved in magnetron sputtering by positioning powerful permanent magnets (0.1 to 0.5 Wb/m^2) behind the target. The secondary electrons are "trapped" by the magnets' strong parallel magnetic field that is introduced near the target surface, allowing for more effective use of the secondary electrons. The Lorentz force causes the electrons to spiral around the magnetic field lines, lengthening their paths in the process. This significantly increases the likelihood of ionizing collisions near the target [34,35].

The intended stoichiometry of each element can vary if a deposition process uses two magnetrons and two targets (co-sputtering). The ultimate composition will be determined by the current applied to each

target. Typically, larger currents will result in higher deposition rates (i.e., how thicker the coating gets per unit of time) [2,36,37].

In this study, we focus on three types of magnetron design, including direct current (DC), pulsed DC, and reactive magnetron sputtering processes [30,31]:

Direct Current (DC) mode: The conductive target (cathode) is connected directly to the negative potential of the power supply, and the substrate (anode) is mounted in a low-pressure vacuum chamber.

Pulsed DC mode: This technique is helpful when there is a chance of arc discharge damage, such as during reactive ion sputtering procedures. Operating parameters for pulsed DC magnetron sputtering include pulsing frequencies (generally between 10 and 350 kHz) and duty cycles (often between 50 and 90 percent).

Reactive Magnetron Sputtering: Using magnetron sputtering in a reactive gas environment makes it possible to deposit dielectric materials. This technique creates films by co-depositing and reacting the components or reacting the deposited species with the surrounding gaseous or vapor environment. The principle of the magnetron sputtering method (whatever the power generation mode) is illustrated in Figure 2-4. The schematic and detailed explanation of the semi-industrial chamber used in this study will be discussed in Chapter 4.

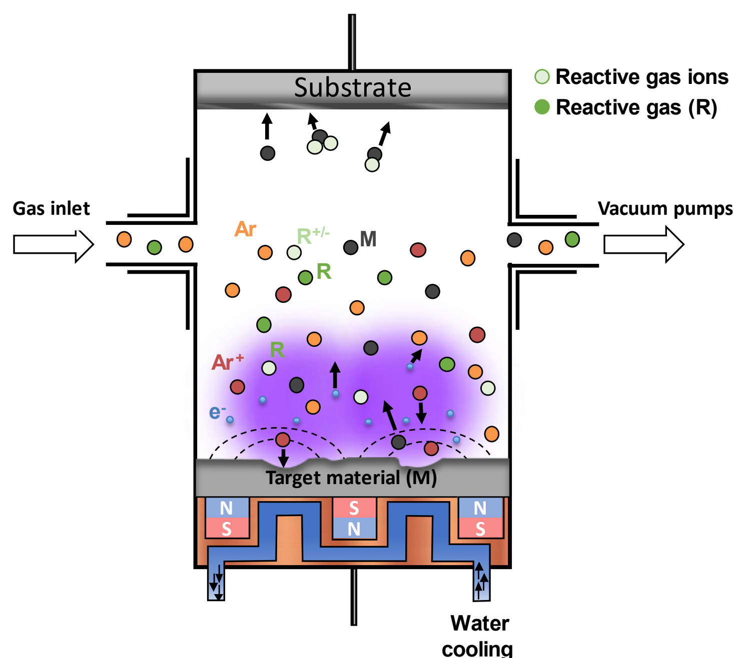

Figure 2-4. The principles of magnetron sputtering (reactive magnetron sputtering).

2.1.4. Thin film growth mechanism

Understanding the principles behind forming thin films is essential to optimize their various characteristics. On the substrate's surface, nucleation and growth take place in order to generate a continuous film. Film growth can be subdivided into multiple stages: adsorption (vapor condensation on the growing surface), desorption (re-evaporation or reemission) from the surface, diffusion of the atoms, formation of stable clusters of atoms, coalescence into islands, and finally, the formation of a continuous film. Those processes are illustrated in Figure 2-5.

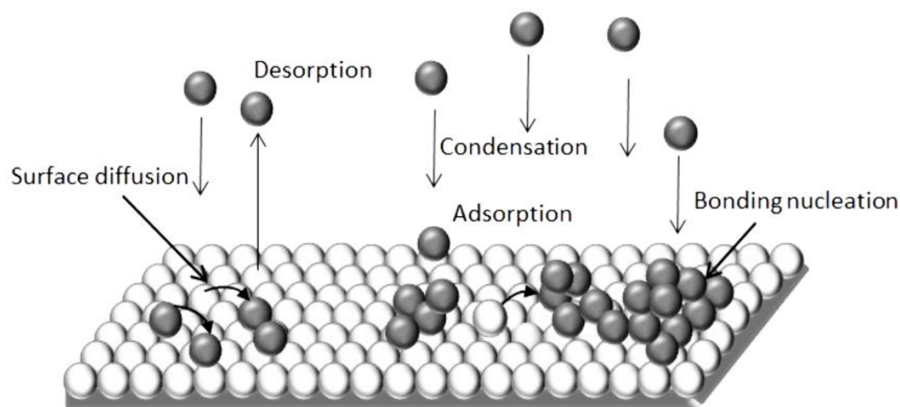

Figure 2-5. Typical thin film growth process (Figure adapted from [38]).

The collision between incident atoms or ions and substrate atoms depends on the energy of the impacting particle, as can be categorized below [38]:

1) An inelastic collision occurs between arriving atoms/ions and substrate atoms if the impacting atom or ion has very low energy. The incoming atom/ion will exchange energy with the atoms on the surface of the substrate, and this atom or ion will be adsorbed.
2) In the relatively higher energy, the collision between the incident atom or ion and the atoms on the substrate surface can still be inelastic. The incident atom or ion will initially become adsorbed on the surface before re-evaporating from it due to the energy exchange.
3) The atoms on the substrate surface will collide with the incident atom or ion in a perfectly elastic collision if the atom's or ion's energy is further raised. Since there can be no energy exchange between the incident atom/ion and the substrate's atoms, the incident atom/ion will be reflected off the substrate surface.
4) The incident atom or ion has enough kinetic energy to cross any potential energy barriers that the substrate atoms may provide at extremely high energies thus, it will penetrate the substrate rather than being reflected by the substrate atoms, which is the implantation process.

Thin film formation in non-equilibrium processes may be explained by one of three main growth modes, depending on the thermodynamic characteristics of the deposition and the substrate surface contact between the adatoms and the substrate material (see Figure 2-6) [39]:

Volmer-Weber mode (3D-island growth): Small, stable clusters may develop on the substrate, expand in three dimensions, and eventually form islands. This form of growth occurs when deposited molecules' binding energy is higher than the substrate's.

Frank-van der Merwe mode (2D-layer growth): In this mode, the growth takes place in two dimensions, filling up one atomic layer before forming the next one, and the atoms are more strongly bonded to the substrate than to each other.

Stranski-Krastanov mode: The production of a few layers precedes the subsequent formation of islands in this combination of layer and island growth. Due to the unfavorable conditions for continued layer development after establishing the first monolayer, islands begin to form.

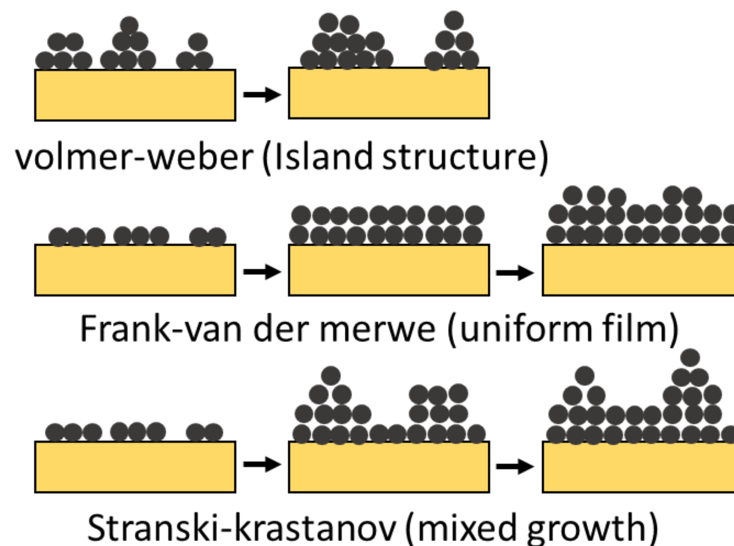

Figure 2-6. Illustration of the development mechanisms of thin films and coatings according to (a) Volmer-Weber, (b) Frank-Van Der Merwe, and (c) Stranski-Krastanov on a substrate surface [39].

The morphology of films and the main influencers on film morphology are categorized into four growth regimes or modes according to the structural zone model (Thornton model) for sputter-deposited films (Figure 2-7). The working gas pressure and the ratio of the substrate temperature to the sputtered material's melting point have the most effects on these growth types. Four growth modes are named: Zone 1, Zone T, Zone 2, and Zone 3. Each zone is connected to circumstances where a certain mechanism dominates the physics of coating development.

- Growth in Zone 1 is achieved at a low $\frac{T_s}{T_m} < 0.1\ or\ 0.2$ ratio at discharge pressure < 3.75 mTorr and $\frac{T_s}{T_m} < 0.4$ at a discharge pressure of 30 mTorr. Adatoms with poor mobility mainly drive this type of growth. Here, T_s is the substrate temperature and T_m is the melting temperature of the material being deposited. Grown film in this zone commonly has cauliflower morphology with dome tops and comprises tapering columns divided by voids. The resultant films exhibit self-shadowing properties and are either amorphous or nanocrystalline.
- Transition morphology occurs in zone T at 0.1 or 0.2 < $\frac{T_s}{T_m}$ < 0.3 to 0.4 at discharge pressure < 3.75 mTorr and at 0.4 < $\frac{T_s}{T_m}$ < 0.5 to 0.55 at a discharge pressure of 30 mTorr. Dense fibrous grains with a very smooth surface make up its distinguishing features. The grain boundary diffusions are severely constrained in these films, which can be either amorphous or nanocrystalline. This promotes competitive grain development and V-shaped grains with a heterogeneous grain structure. Dense films with big grains form at higher temperatures because of bulk diffusion and recrystallization.
- Zone 2 can be observed at 0.3 to 0.35 < $\frac{T_s}{T_m}$ <0.7 for discharge pressure < 3.75 mTorr and at 0.5 to 0.55 < $\frac{T_s}{T_m}$ < 0.7 at a discharge pressure of 30 mTorr. It displays a dense columnar structure separated by grain boundaries. Because the columnar grain size increases with $\frac{T_s}{T_m}$ in agreement with the activation energies for these mass-transport modes, surface and grain-boundary diffusion appears to play an increasingly significant role in the evolution of this structure.
- Within Zone 3 (0.75 <$\frac{T_s}{T_m}$ for the entire discharge gas pressure range) the structural configuration manifests as equiaxed (globular) three-dimensional grains. This characteristic signifies a discontinuous progression in crystal development, suggesting periodic halting or interruption in the growth process. Such a distinctive construction pattern is frequently observed under conditions of heightened substrate temperatures. This phenomenon implies that the elevated temperature range prevailing within this zone plays a pivotal role in dictating and influencing the formation of this particular grain structure [40–43].

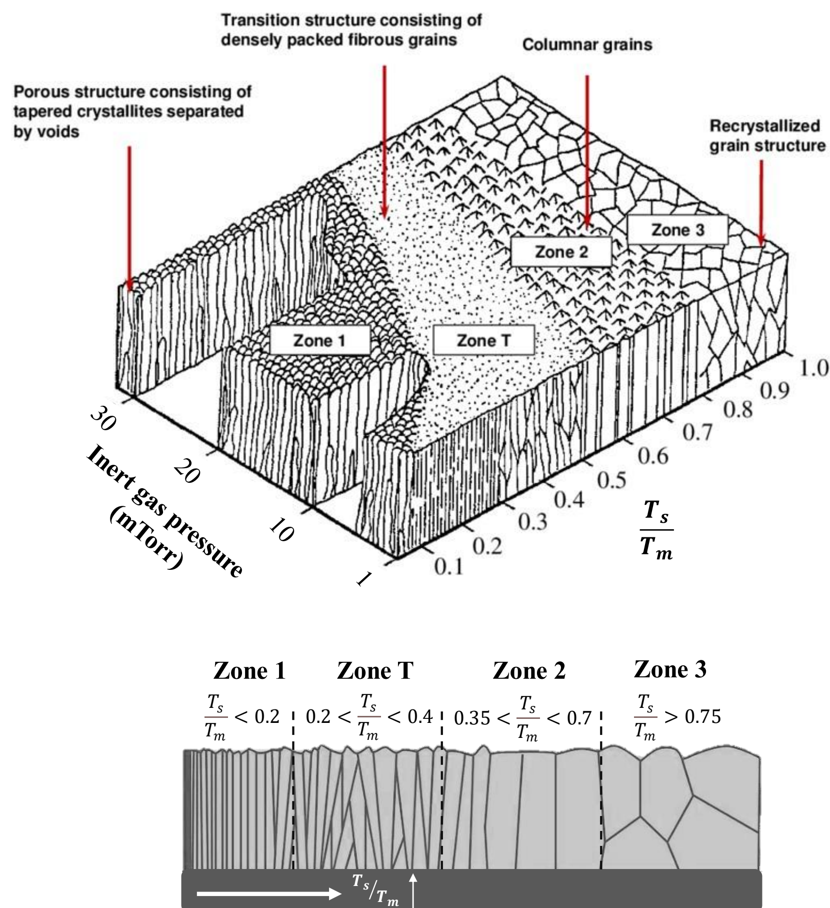

Figure 2-7. Structure zone model representing the effects of homologous substrate temperature and Ar discharge-gas pressure on the structure of metal films deposited by magnetron sputtering [42].

2.2. Summary

The wet and dry thin film deposition methods were fully examined in this chapter, and (reactive) magnetron sputtering was emphasized for its industrial scalability, high deposition rate, material purity, repeatability, and excellent coating adhesion.

The theory of plasma, a crucial element in many deposition processes, is also covered in detail in this chapter. It highlights the common low-temperature plasma processes and their importance in thin film deposition.

A detailed explanation of the sputter deposition process has been covered with an explanation of the different steps.

The chapter also covered the influence of ion energy on sputtering and thoroughly described the morphologies of thin film formation.

Chapter 3.

3. Amorphous coatings

This chapter gives a general overview of the amorphous materials and the motivation of the author to study the amorphous coatings, especially a-C:H and Cu-Zr thin film metallic glasses. Moreover, it will provide a literature review on the physical-chemical characterization and mechanical properties of the mentioned coatings group.

3.1. Introduction to amorphous materials

Amorphous and crystalline materials share fundamental traits inherent to solid-state matter, such as rigidity, incompressibility, and the capability to uphold a distinct shape, defining their classification as solids. Nonetheless, their crucial disparity resides in their atomic-level organization. In the crystalline state, atoms assume equilibrium positions structured within a well-defined, extensive, repetitive pattern, exhibiting long-range order (LRO). Conversely, in the amorphous state, atoms exhibit a disordered arrangement without extensive, repetitive patterns, and have short-range order (SRO) [44,45].

The genesis of amorphous materials dates back to the 1960s, marked by the discovery facilitated through the rapid solidification of molten liquids. This breakthrough method enabled the creation of non-crystalline materials, leading to the identification and exploration of materials exhibiting disordered atomic structures. This innovation revolutionized our understanding of material science by introducing a distinct class of solids characterized by their unique atomic-level arrangements, distinct from traditional crystalline structures. These materials possess enhanced strength and hardness (i.e., compressive strength up to 6 GPa for metallic glasses and up to 70 GPa for the amorphous carbon and hardness up to 130 GPa [46,47]), owing to the absence of the long-range order. The absence of long-range order results in a high degree of structural disorder and numerous structural defects, including irregularities in atomic packing. These defects act as barriers to the movement of dislocations, which are one of the primary mechanisms by which crystalline materials deform under stress. The metastable nature of amorphous materials and their random atomic packing give rise to distinct structural and mechanical properties [48].

The transition from liquid to a solid state is seen in Figure 3-1 where matter volume is plotted versus the temperature. The volume of the matter continuously reduces as it cools. The slope of the volume-temperature curve represents the liquid's thermal expansion coefficient (a measure of how much a material expands or contracts when its temperature changes). The transition from liquid to solid occurs when the temperature falls below the melting point (T_m)(except liquid helium). The volume-temperature curve's sudden volume contraction and discontinuity indicate the transition from liquid to solid. If the cooling rate is fast enough, the liquid state can be preserved up to the glass transition temperature (T_g). The second solidification event is the change from liquid to amorphous phase. Numerous investigations have demonstrated the strong connection between the cooling rate and T_g, demonstrating the kinetic character of the T_g. High cooling rates cause the liquid to become "frozen" at higher temperatures (T_{g1}) because the atoms won't have enough time to arrange themselves. An exceptionally (meta) stable glassy structure with a higher energy and free volume content is the final product. Reduced cooling rates let a certain amount of atomic organization occur in the supercooled area prior to freezing, which also leads to a denser structure and a lower value of T_g (T_{g2}) [49,50]. The

cooling rate is a crucial process parameter that determines the microscopic structural arrangement rate required to maintain equilibrium during cooling. It is connected to the nature of atomic bonds. Polymers can turn to an amorphous state rapidly at low cooling rates because they are made of long macromolecular chains (covalent bonds) with little spatial mobility (10^{-2} Ks^{-1}). Longer periods of atomic organization are required for polymers to crystallize, which increases their glass-forming ability (GFA[1]). However, in order to undergo the glass transition, liquid metals with non-directional bonding and significant melt mobility require a faster cooling rate. Depending on the composition of the alloy, typical values range from 10^3 to 10^8 Ks^{-1}, indicating that these materials have a high crystallization capacity and a lower GFA than a covalent glass [44,51,52].

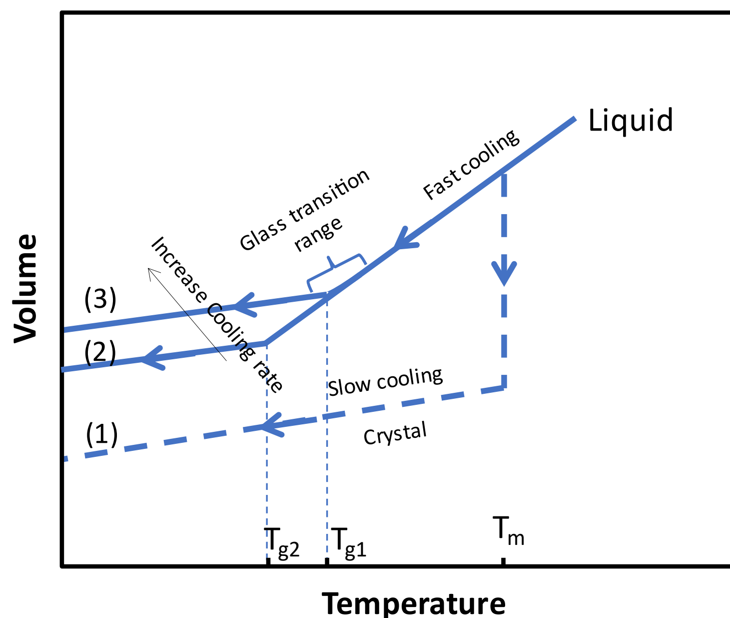

Figure 3-1. Cooling paths from liquid to solid. Path 1 route to crystalline structure, and Path 2 and 3 routes to amorphous structure with different cooling rate effects on T_g [50].

Since only two groups of amorphous thin films will be studied within this thesis, we will focus on a short introduction of each group, their characterization, and their properties, which have been studied in the literature.

[1] GFA is the capacity of a material to remain amorphous in the absence of any crystallization. A balance between kinetic, thermodynamic, and topological considerations is shown by the GFA's preference for mixtures where the liquid is comparatively stable in relation to crystalline phases.

3.1.1. Amorphous carbon

Carbon can be categorized into several types of allotropes based on how the C-C bonds are hybridized, including sp (carbyne), sp^2 (graphite, graphene), and sp^3 (diamond). The structure of different allotropes is illustrated in Figure 3-2. Five key parameters categorize the carbon films: (i) the sp^3 content; (ii) the sp^2 phase clustering; (iii) the sp^2 phase orientation; (iv) the film cross-sectional nanostructure; and (v) the overall hydrogen content. The hydrogen concentration and the sp^2/sp^3 ratio have a relationship with the tribo-mechanical characteristics of carbon films. The chemical, mechanical, and tribo-mechanical characteristics of the films are influenced by the hydrogen concentration, whilst the sp^2/sp^3 ratio controls the mechanical properties and the films' adherence to other surfaces. Nevertheless, there is a complicated link between these factors and the films' tribo-mechanical characteristics. For instance, a higher sp^2 concentration in the films may produce softer films, but a higher sp^3 level may produce harder films. Similarly to this, adding more hydrogen can make the films more resistant to wear, but too much hydrogen decreases the films' hardness and young's modulus. The sp^2 clustering, sp^2 orientation, or cross-sectional nanostructure mainly affects the optical and electronic properties. To get the appropriate tribo-mechanical properties of the films, a delicate balance between these parameters is needed [22,23,53].

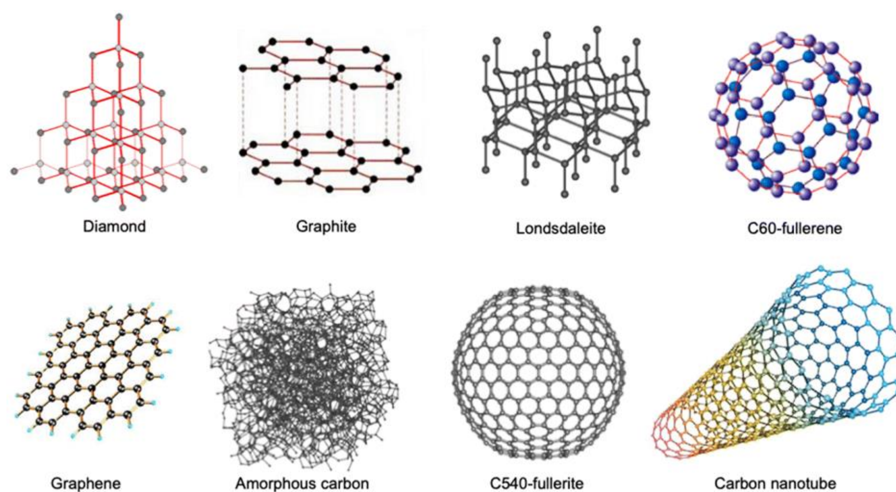

Figure 3-2. Carbon allotropes: diamond, graphite, lonsdaleite, C60-fullerene, graphene, amorphous carbon, C540-fullerite, and single-walled carbon nanotube (Figure adapted from [54]).

In the sp^3 configuration, each of the four valence electrons of the C atoms is involved in a tetrahedrally directed sp^3 orbital that creates a strong σ bond with a neighboring atom. However, in the three-fold coordinated sp^2 configuration, three out of four valence electrons involved in the trigonally directed sp^2 orbitals form the planar σ bonds, and the fourth electron lies in the pπ orbital in the normal direction to the σ bonding plane [22,23,53]. The orbital hybridization model is shown in Figure 3-3.

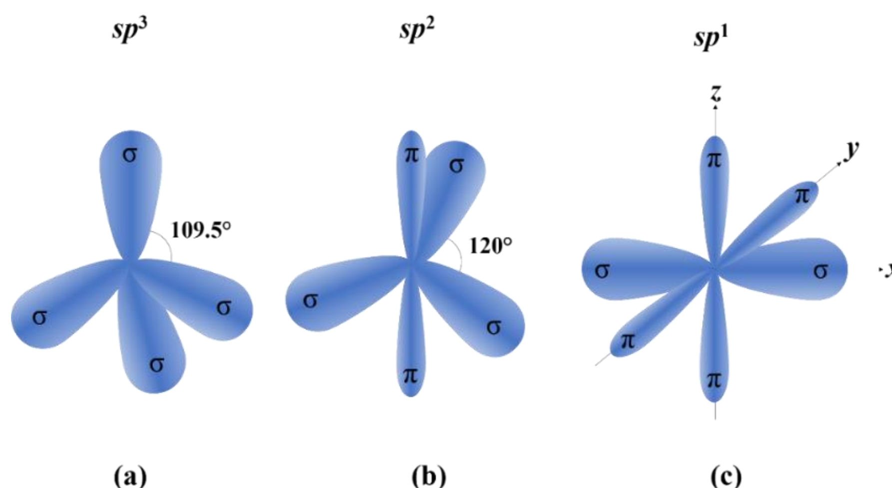

Figure 3-3. Hybridizations of carbon a) sp^3,b) sp^2, and c) sp^1 configuration (Figure adapted from [53]).

Amorphous carbon (a-C) is the result of incomplete carbonization. It is characterized by a broad range of C-C bond length and angle and lacks long-range structural ordering. sp^2 and sp^3 hybridizations with a minor sp contribution are the product of a-C orbital structure, which is influenced by the synthesis conditions, precursor molecules, and substrate material. As a result, the carbon atoms in a–C may undergo distinct hybridizations; some may undergo sp^2 hybridization, which involves three equivalent sp^2 orbitals and one p orbital remaining, while others may undergo sp3 hybridization (involving four equivalent sp^3 orbitals). A small amount of sp hybridization is present, indicating that sp^2 and sp^3 are mostly responsible for the carbon atom hybridization in a-C and sp hybridization plays a minor role in this process [24,55].

A kind of a-C known as hydrogenated amorphous carbon (a-C:H) contains hydrogen in addition to various amounts of tetrahedral (sp^3) and graphite-like (sp^2) carbon bonds. Because of its distinct qualities, a-C:H is often used as a protective coating in the industry. They have low dry-wear resistance, and the surface hydrogen improves lubricant adhesion [56].

a-C:H are classified into four types [22,57–60]:

1) a-C:H films with the highest H content (40-60 at.%): These films may contain up to 70% sp^3. Although the material is soft and has low density, most of the sp^3 bonds are H-terminated. These films are what we refer to as polymer-like a-C:H. (PLCH). The bandgap is about 2-4 eV. Usually, low bias voltage plasma-enhanced chemical vapor deposition (PECVD) is used to deposit these films.

2) a-C:H films with intermediate H content (20-40 at.%): These films have more C-C sp^3 bonds than PLCH, although having a lower total sp^3 concentration. They, therefore, possess greater mechanical characteristics. Their optical gap ranges from 1 to 2 eV. These films are called diamond-

like a-C:H (DLCH). Typically, they are deposited by reactive sputtering or PECVD with a modest bias voltage.

3) Hydrogenated tetrahedral amorphous carbon films (ta-C:H) belong to a class of Hydrogenated diamond-like carbons (DLCHs) where a constant H content can coexist with an increase in C-C sp^3 content. Most films listed as ta-C:H in the literature are merely DLCH. As evidenced by their Raman spectra, greater density (up to 2.4 $g.cm^{-3}$), and higher Young's modulus (up to 300 GPa), ta-C:H films are really in a separate group due to their higher sp3 content (70 percent) and 25-30 at% H. Their optical gap is 2.4 eV or more. High-density plasma sources like plasma beam sources (PBS) and the electron cyclotron wave resonance (ECWR) deposit these layers.

4) a-C:H with low H content (less than 20 at.%): They exhibit sp^2 clustering and high sp^2 concentration. The gap is less than 1 eV. We refer to these films as graphite-like a-C:H (GLCH). They are typically deposited using magnetron sputtering or PECVD at high bias.

The ternary phase diagram shows the various forms of amorphous carbon in Figure 3-4.

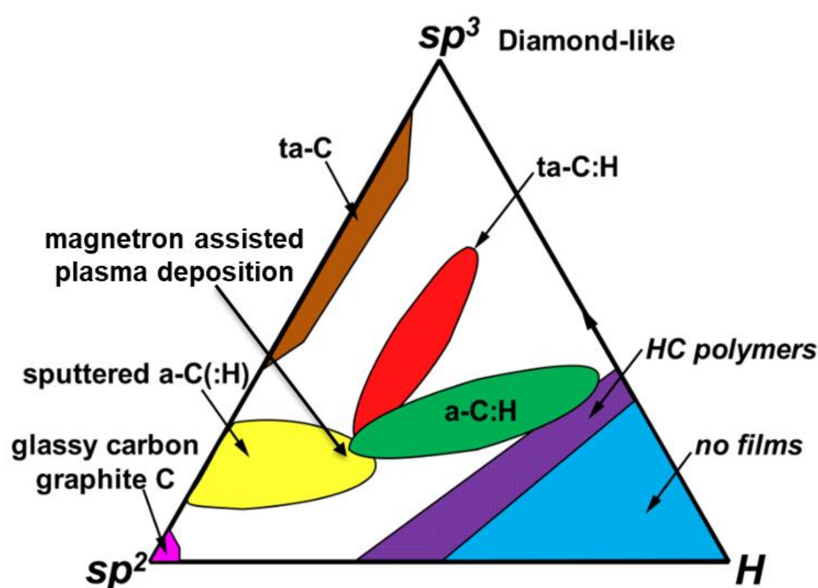

Figure 3-4. Ternary phase diagram of various amorphous carbon forms (Figure adapted from [57]).

The area without C-C bonds is indicated on the phase diagram's lower right side; as a result, no films may be synthesized there. The phase diagram's lower left side displays amorphous carbon with no hydrogen, such as chars and soot (about 100 percent sp^2 bonds). Tetrahedral amorphous carbon (ta-C), which is represented by the upper-left of the phase diagram, is a name for amorphous carbon films with a high degree of sp^3 bonding (>80%). The area of a-C:H films with varying hydrogen contents and sp^3/sp^2 bonding ratios is depicted in the middle of the phase diagram. The characteristics of several amorphous carbon film types are compiled in Table 3-1.

Table 3-1. Comparison of major properties of amorphous carbons with those of reference materials: diamond, graphite [57].

	Sp^3 (%)	H (%)	Density ($g.cm^{-3}$)	Hardness (GPa)	Gap (eV)
Diamond	100	0	3.515	100	5.5
Graphite	0	0	2.267	0.3	0
ta-C	80-88	0	3.1	80	2.5
a-C: H hard	50-70	28-15	1.6-2.2	10-20	1.1-1.7
a-C:H soft	0-70	15-35	1.2-1.6	<10	1.7-4
ta-C:H	70	30	2.4	50	2-2.5

The hardest known material is diamond, which has a hardness of 100 GPa and comprises carbon atoms arranged in a tetrahedral configuration. Additionally, it possesses the highest packing density of carbon atoms and the biggest bandgap (4.5–6.0 eV) (3.515 $g.cm^{-3}$). In contrast, graphite, which has a layered hexagonal carbon structure, has a low hardness (11.5 GPa), a high density (2.267 $g.cm^{-3}$), and no bandgap. Based on the sp^3 ratio (0-90%) and hydrogen concentration (0-65%) of the material, the characteristics of the substance exhibit a wide range, including densities (0.6-3.5 $g.cm^{-3}$), hardness (3-65 GPa), and optical bandgap (0.8-5.0 eV) [57,61,62].

3.1.2. Cu-Zr metallic glass

One particular metallic glass (MG) system that falls under the category of binary MGs is the Cu-Zr system. Due to their exceptional mechanical properties, Cu-Zr-based MGs have garnered increasing attention in recent years. These alloys exhibit high tensile strength (up to 3.5 GPa) [63], four-point bending fatigue strength (around 500 MPa for 37766 cycles) [64], hardness (up to 10 GPa) [65], fracture energy release rate (3-150 kJ/m^2) [66], excellent glass forming range (20 at% - 70 at% of Zr) [67], variable Young's modulus ranges from approximately 40 to 114.3 GPa [68,69], cutting machinability, and corrosion resistance. Cu-Zr-based MGs are more appealing because they are composed of common and inexpensive elements [70–72].

One of the key factors contributing to the desirable properties of Cu-Zr-based MGs is their rapid manufacturing process, a wide GFA, and the creation of a stable amorphous structure due to variations in atomic sizes between Zr (1.60 Å) and Cu (1.28 Å), as well as their low ΔH_f of max -23 kJ/mol [67,70–72]. They exhibit an ordered structure from a chosen atom (~0.5 nm) at least within the first neighbor coordination shell. The results of diffraction studies, which indicate the existence of an initial, intense diffuse halo followed by a second, broader, less intense one that contains important information about the local order, are closely linked to the evidence of an SRO [44,51,73,74]. Furthermore, according to the studies by Kaban *et al.* [41], Icosahedral-like structures with potential distortion and/or truncation

are present in Cu-Zr basic structural units. The term "icosahedral" refers to a particular geometric arrangement of atoms, which resembles a 20-sided polyhedron and locally maximizes the density of packing and are incompatible with the crystalline structure. It influences the material's properties, including its mechanical and thermal behavior. Distortions or truncations in these structures can affect the material's hardness, ductility, and other mechanical properties [70,75,76].

The binary Cu–Zr system contains 12 phases: HCP-Zr (αZr), BCC-Zr (βZr), FCC-Cu (Cu), intermetallic compounds; Cu_5Zr, $Cu_{51}Zr_{14}$, Cu_8Zr_3, Cu_2Zr, $Cu_{10}Zr_7$, CuZr, Cu_5Zr_8, $CuZr_2$, and liquid [77]. The Cu-Zr binary phase diagram with more possible regions for amorphization is shown in Figure 3-5. The solid-liquid phase boundaries and lines of equilibrium are depicted. However, amorphous films are in the metastable phase since an intrinsically out-of-equilibrium process is being used during the production. In conditions far from equilibrium, thermodynamics alone will not be adequate to understand phase formation, phase selection, and microstructure, nor will it have enough time to bring about an equilibrium state. The intermediate states, or metastable phases, of a thermodynamic system, are those that can persist for a long time before transitioning to a more stable phase. Through the integration of solidification kinetics, scientists may acquire a clearer knowledge of the advancement of metastable phases within the Cu-Zr system. While kinetics provides the data necessary to understand the system's evolution over time, thermodynamics provides a framework for understanding the energetics of the system [78–80].

In the Cu-Zr system, for instance, Liu *et al*.[81] investigated the thermodynamics of rapid solidification and the kinetics of crystal growth. The study took into consideration the solute's relaxation period and looked at growth rates and thermodynamic driving forces in rapid solidification. The findings demonstrated that the crystal's growth rate was inversely proportional to the solute's relaxation time and directly related to the driving force.

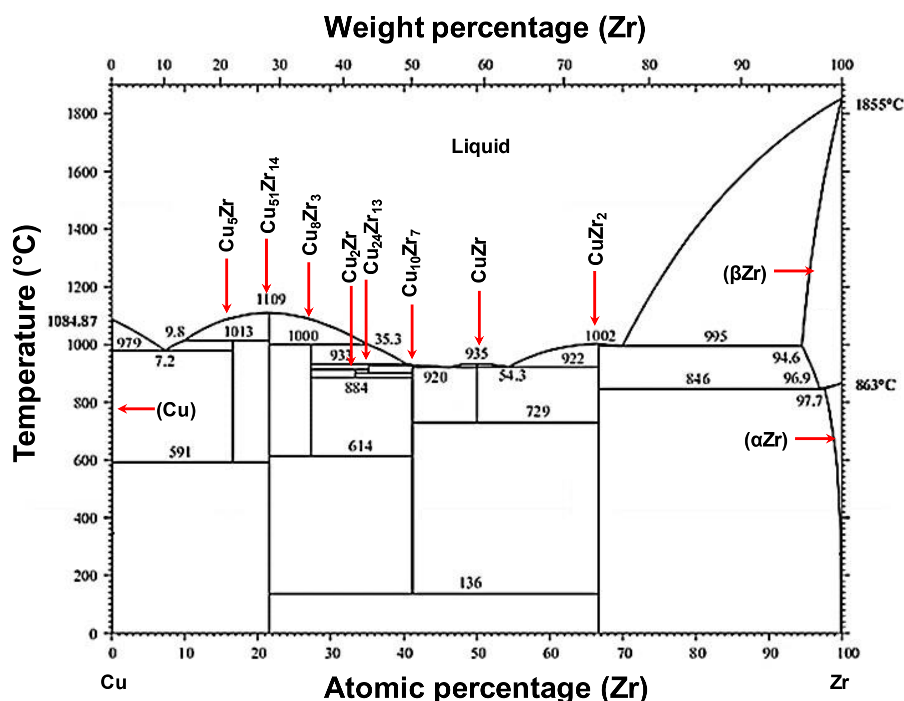

Figure 3-5. Binary Cu–Zr MG phase diagram (Figure adapted from [17]).

In order to analyze the thermodynamic characteristics of these compounds, it is necessary to compute the ground-state total energies of the eight Cu-Zr intermetallic compounds, in addition to pure copper and zirconium. The differences between the total energy of Cu_aZr_b and the linear combination of the stable state energies of pure copper and zirconium are the enthalpy of formation for a certain Cu-Zr intermetallic compound. Therefore, the enthalpy of formation is

$$\Delta H_{formation}^{Cu_aZr_b} = \frac{\Delta H_{Total}^{Cu_aZr_b} - (a\Delta H_{solid}^{Cu} + b\Delta H_{solid}^{Zr})}{(a+b)}, \quad (3\text{-}1)$$

where $\Delta H_{Total}^{Cu_aZr_b}$ is the total energy of the Cu_aZr_b initial cell containing ‘‘a’’Cu atoms and ‘‘b’’Zr atoms with their stable ground state structures, ΔH_{solid}^{Cu} is the total energy of one Cu atom in a face-centered cubic structure with its equilibrium lattice parameters and ΔH_{solid}^{Zr} is the total energy of one Zr atom in a hexagonal close-packed structure with its corresponding equilibrium lattice parameters [77,82–85]. The thermodynamic stability of Cu-Zr intermetallic compounds can be extracted from the enthalpy of formation. The enthalpy of formation and the space group of each phase is illustrated in Table 3-2 and Figure 3-6.

Table 3-2. Crystal structures of phases in the binary Cu–Zr system [77].

Phase	Space group	ΔH_f (kJ/mol)
Cu-A1	$Fm\bar{3}m$	---
Cu_5Zr	$F\bar{4}3m$	-11.77
$Cu_{51}Zr_{14}$	P6/m	-9.5
Cu_8Zr_3	Pnma	-16.3
Cu_2Zr	Amm2	-11.6
$Cu_{10}Zr_7$	Aba2	-16.1
CuZr	$Pm\bar{3}m$	-6.1
Cu_5Zr_8	Pbam	-5.3
$CuZr_2$	I4/mmm	-12.7
αZr	$Im\bar{3}m$	---
βZr	P63/mmc	---

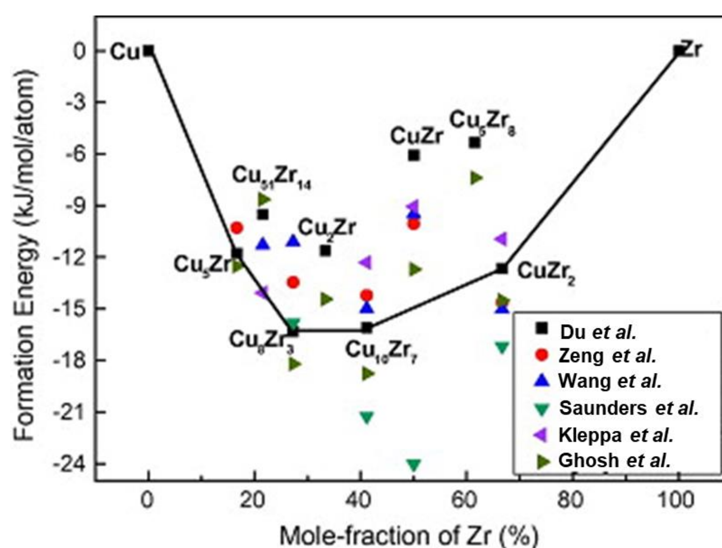

Figure 3-6. Heats of formation values for the Cu–Zr binary system intermetallic compounds [77,84–88].

The thermodynamic stability and reactivity of each phase is determined from the Cu-Zr system enthalpy of formation data. A more negative enthalpy of formations implies more thermodynamically stable intermetallic compounds [77].

The kinetic perspective defines homogeneous nucleation and the development of a spherical crystalline phase from the undercooled liquid, named the nucleation frequency, $J(T)$ as [89]

$$J(T) = \frac{10^{30}}{\eta} \exp\left[\frac{-16\pi\alpha^3\beta}{3}\left(\frac{T_r}{1-T_r}\right)^2\right], \qquad [\text{nucleus.s.m}^{-2}] \qquad (3\text{-}2)$$

where, $T_r = (T/T_m)$ is the reduced temperature, η is a viscosity ($m^2.s^{-1}$), α and β dimensionless parameters related to the energy of the liquid / solid interface (σ), expressed by the following equations

$$\alpha = (N_0V)^{1/3}\sigma/\Delta H_f, \quad (3\text{-}3)$$

$$\beta = \Delta S_f/\mathrm{R}, \quad (3\text{-}4)$$

where N_0 is Avagadro's number, R is the universal gas constant, $\Delta S_f = {}^{\Delta H_f}/_{T_m}$, and V is the atomic volume of the crystal. The above equations indicate that the increase in β and α values will decrease the ΔH_f value in the thermodynamic term. It is concluded that if the $\alpha\beta^{1/3}$ term in this equation is above 0.9, crystallization will not take place at any cooling rate, and the amorphous film will grow; however, it will not be possible to prevent the crystallization of liquid when $\alpha\beta^{1/3}$ is below 0.3 [90,91].

3.2. Characterization of amorphous coatings

Coatings, with their diverse applications across various industries, have become integral in tailoring and enhancing materials' mechanical and tribological properties. A comprehensive understanding of coating characteristics is pivotal for predicting and optimizing performance in engineering applications [92]. This section delves into the nuanced characterization of two distinct coatings (amorphous carbon (a-C:H) and Cu-Zr TFMGs) and aims to decipher the intricate relationship between deposition parameters' effect on the film characteristics and resultant mechanical properties.

3.2.1. Characterization of a-C coatings

The characterization of a-C:H coatings allows us to understand their microstructure, chemical composition, and binding configuration, which are closely linked to their mechanical and tribological performance. The hump peaks indicating (002) and (100) planes of graphite with rapidly decreasing intensity (characteristic of short-range ordered amorphous materials) in a-C films X-ray diffraction (XRD) analysis is evidence for their amorphous state. Here, the XRD pattern of the deposited a-C:H film with graphite target is seen in Figure 3-7. However, it is essential to note that XRD analysis alone may not fully characterize a-C due to its disordered nature. Complementary techniques, such as spectroscopy and microscopy, are often employed to comprehensively understand a-C's properties and behavior.

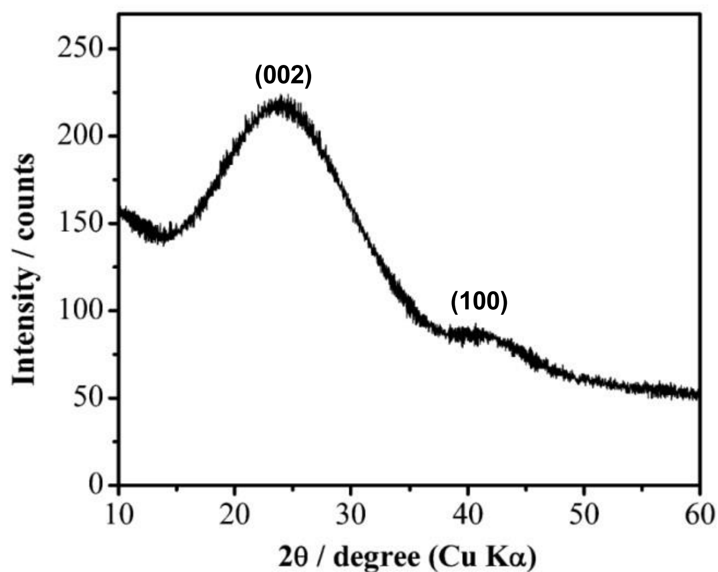

Figure 3-7. XRD pattern of amorphous carbon (Figure adapted from [93]).

This group of coatings shows low surface roughness even though they have columnar growth structures. Low roughness results from their amorphous nature and deposition parameters also influence the final surface roughness. Figure 3-8 illustrates the cross-section, top view, and surface roughness of magnetron sputtered a-C film characterized by Zhang *et al.* [94].

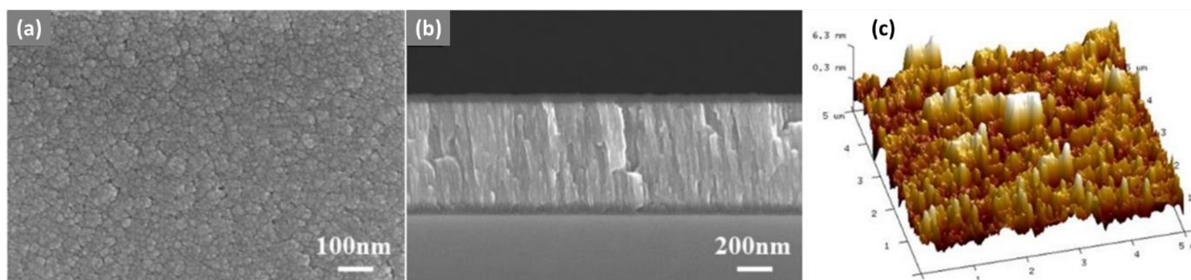

Figure 3-8. SEM image of (a) top view and (b) cross-section besides (c) AFM image of the a-C film (Figure adapted from [94]).

Generally, the a-C coatings show the common features of D (at around 1380 cm^{-1}) and G (at around 1580 cm^{-1}) bands in the 800–2000 cm^{-1} region in their Raman spectra. Figure 3-9 shows typical Raman spectra of the a-C films with indicated D and G peaks.

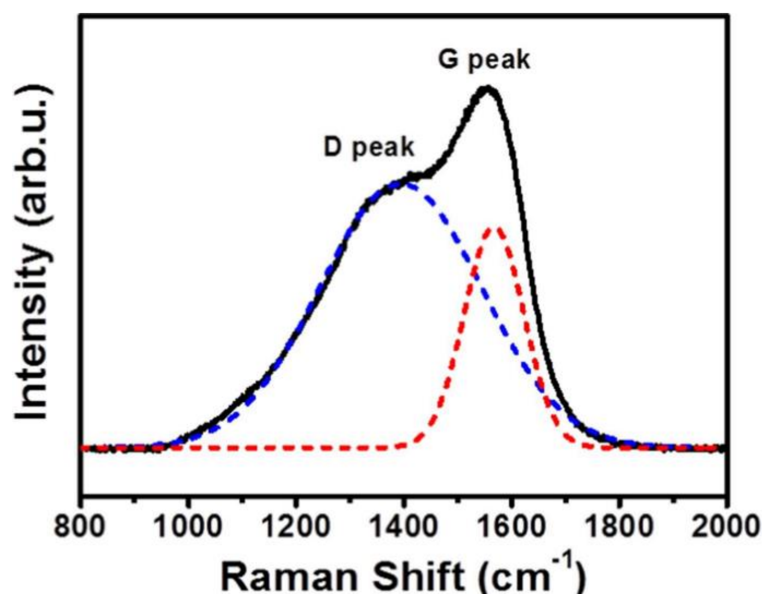

Figure 3-9. Raman spectra of a-C film (Figure adapted from [95]).

The G peak is considered to arise from the bond stretching of all sp^2 atom pairs in both rings and chains and the D peak is due to the presence of non sp^2 sites but activated by the presence of the sp^2 sites and arises from various types of non sp^2 sites including sp^3 sites and is due to the breathing mode of sp^2 atoms in rings [96]. Thus, by studying the Raman spectra of films, the ratio of $\frac{sp^2}{sp^3}$ can be extracted which is a qualitative way to study the graphite structure and hydrogen content in the film. The sp^2 hybridization results in the formation of double bonds and is characteristic of graphite-like structures, while sp^3 hybridization forms single bonds and is associated with hydrogenated or amorphous carbon structures (disordered structure). Thus, the higher $\frac{sp^2}{sp^3}$ ratio shows higher amount of graphite-like (sp^2) and potentially hydrogenated (sp^3) carbon bonds in the film.

3.2.2. Characterization of Cu-Zr thin film metallic glasses

Cu-Zr films with an amorphous state can be obtained on a wide composition, ranging from 20 to 70.0 at.% Zr. As the Cu content increases, the hump peak shifts to the higher 2θ˚ due to the reduction in the mean distance between the initial neighbor atoms. It is caused by the Cu atoms' smaller atomic size and/or by stronger atomic bonds by increasing the Cu content [70,72,97]. Figure 3-10.a shows a typical XRD pattern for Cu-Zr TFMGs studied by Brognara *et al.* [63]. Figure 3-10.b shows the decrease in lattice spacing and hump peak shifting by increasing the Cu content. Using the Ehrenfest formula ($r = 0.615 \times \lambda / sin\,\theta$ [77]) to compare the mean distance between the initial neighbor atoms and calculations according to the rule of mixture shows a very high density of films with Cu contents above 50 at.% [71].

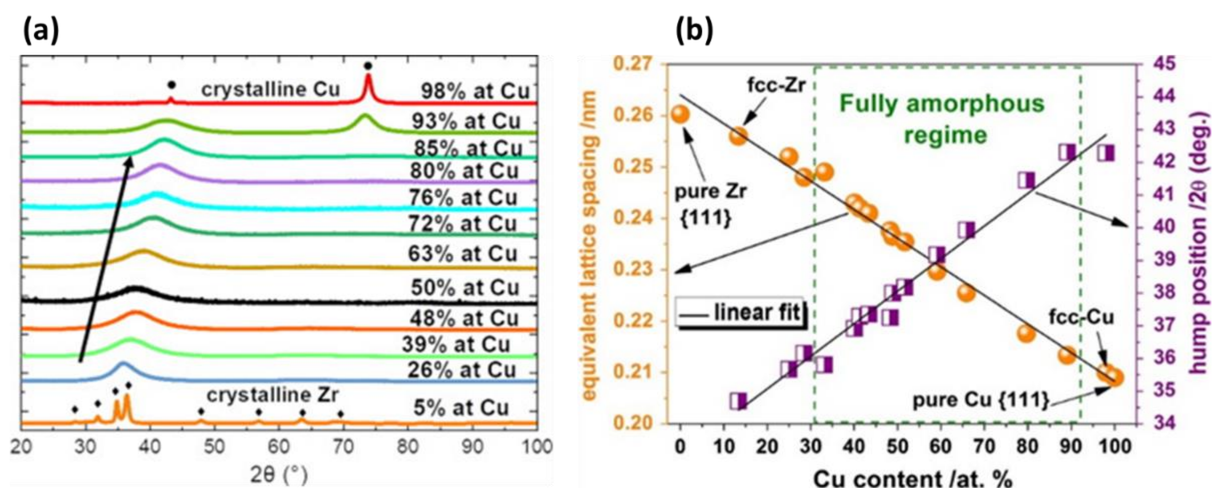

Figure 3-10. (a) XRD patterns of the as-deposited Zr–Cu thin films deposited on the glass substrate (b) The equivalent lattice spacing and hump peak position change with the Cu content in Cu-Zr monolithic TFMG (Figure adapted from [63,72]).

Cu-Zr based TFMGs are characterized by extremely low roughness as well, due to their dense and amorphous structure, with the absence of grain boundaries. Controlling the thin film growth through the discharge parameters allows direct control of the final structure. Thin film growth depends on deposition parameters during the growth process, namely: substrate temperature, deposition power, pressure, and alignment of arriving atoms with the substrate. The deposition parameters determine plasma conditions and affect film growth, which in turn influences the microstructure and properties of the thin film as discussed rest of this section [63,98–100].

Zeman *et al*. [101] deposited Cu-Zr films using DC magnetron sputtering within two different deposition power densities of 40 W/cm^2 and 1000 W/cm^2. According to them, introducing the amorphous film decreases the surface roughness even more by increasing the Cu at.%. Moreover, increasing the power density decreases the surface roughness from around 1.5 nm to below 1 nm. Figure 3-11 illustrates the AFM topographic scans and cross-sectional scanning electron microscopy (SEM) images of pure Zr, Cu, and monolithic Cu-Zr TFMGs.

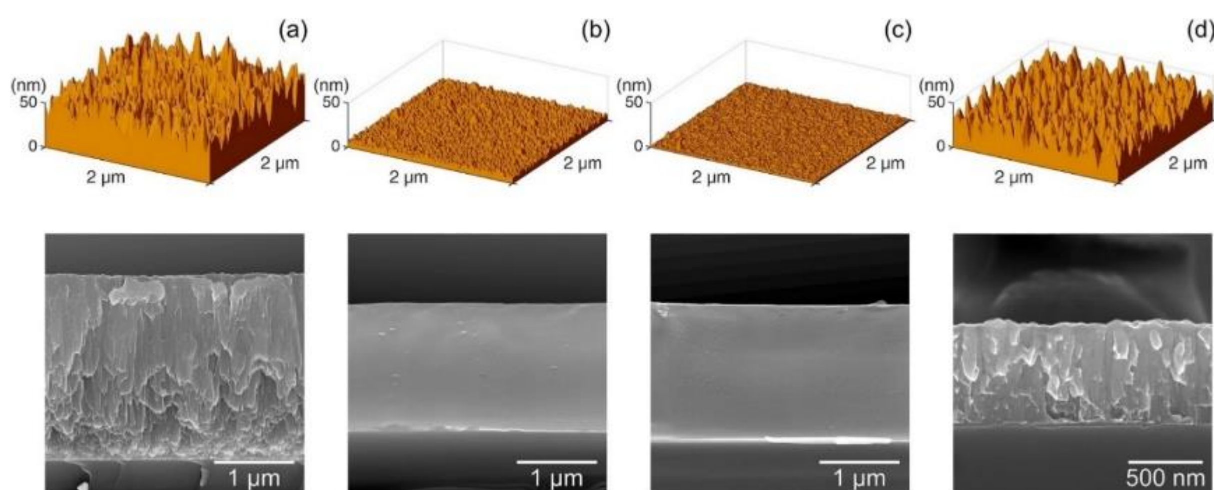

Figure 3-11. The surface morphology (AFM images) and the microstructure in cross-section (SEM images) of (a) the pure Zr film, the Cu-Zr films with (b) 49 at.% and (c) 69 at.% Cu and (d) the pure Cu film deposited at the high power density conditions (Figure adapted from [101]).

Although several studies have shown different fracture shapes in cross-sections of Cu-Zr based TFMGs, the reason behind these differences is still not well understood. For instance, columnar growth and cross-section are reported by Rauf *et al.*[69] or vein patterns illustrated by Brognara *et al.* [63], as can be seen in Figure 3-12. Besides, featureless shape, as shown in Figure 3-11. It has been proposed that the large substrate-to-target distance and low deposition power during film formation generate a less homogenous flow of sputtered atoms, which reach the substrate with reduced energy and lead to cluster growth and, ultimately, a columnar structure [63]. However, there is no rational explanation for the different fracture behaviors, even if the initial growth shape is similar in different Cu-Zr TFMGs. Similar amorphous film composition with a different fracture behavior must be addressed well since it can later explain the material's mechanical characteristics or end-user application.

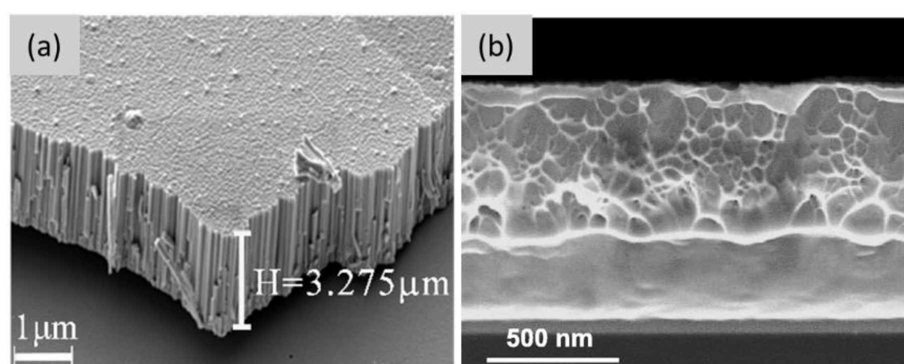

Figure 3-12. (a) columnar and (b) vein-like cross-section morphologies of Cu-Zr based TFMGs.

3.3.Mechanical properties of coatings

Examining coatings' mechanical characteristics has significant effects on real-world uses. To ensure that these coatings work well in a variety of situations, it is essential to comprehend their mechanical behavior.

Challenges with a-C:H films stem from their poor adherence to metals, which is caused by bonding mismatches at the substrate/film interface and compressive stresses. Techniques like interlayer coatings and doping with materials like titanium and chromium are investigated to customize their mechanical characteristics. Optimizing a-C:H films is essential to guarantee their performance in applications such as wear-resistant coatings by overcoming adhesion and hardness issues [102,103].

The problems for Cu-Zr TFMGs are related to recrystallization, oxidation, and the delicate balance required to preserve their amorphous structure. These coatings' wear resistance and general durability largely depend on their mechanical attributes, such as hardness and fracture toughness. Some of the tailoring tactics are adjusting the Cu/Zr ratio, investigating multilayer structures, and comprehending the influence of secondary phases on mechanical softening. The development of Cu-Zr TFMGs with enhanced hardness, wear resistance, and thermal stability due to successfully overcoming these obstacles makes them attractive options for applications seeking durability at high temperatures [104,105].

In addition to providing a general comparison of the two groups, this section will go into detail regarding the various factors that influence the mechanical properties of the coatings group mentioned and provide a general overview of their impact on adhesion, wear resistance, and fracture toughness of the coating.

3.3.1. Mechanical properties of a-C coatings

Because of their high compressive stresses and mismatched bonding types at the substrate/film interface, hydrogenated amorphous carbon (a-C:H) films exhibit poor adhesion to metals in general. The functional qualities of a-C:H under various situations must be ensured by a strong adhesive strength on the substrate in order to prevent failure. Applications of interlayer films based on carbide-forming elements such as Si, Cr, or Ti are popular to increase the adhesion strength on metallic substrates [102]. Adding a dopant is another technique to increase the a-C:H coatings' adherence to the substrate. It has been shown that doping a-C:H coatings' with titanium and chromium reduces internal stress, fracture risk, and material surface peeling [103].

a-C:H films show lower hardness compared to another group of a-C films due to the higher amount of sp^2 and H% in their structure. Thus, it can be noted that the average hardness for this set of films can

vary between 3-10 GPa depending on the doping material and deposition process. It is well noted that adding a metallic underlayer may sacrifice the hardness while increasing the adhesion to the substrate material. Besides that, the doping material affects the films' wear behavior. A recent study by Lie *et al*.[104] illustrated in Figure 3-13 shows improved wear behavior of a-C:H:Cr thin films, with a slight decrease in hardness value. The reason for the decline in hardness is related to the production of Cr-C or metal nano-cluster phase, which disrupts the continuity of the carbon network.

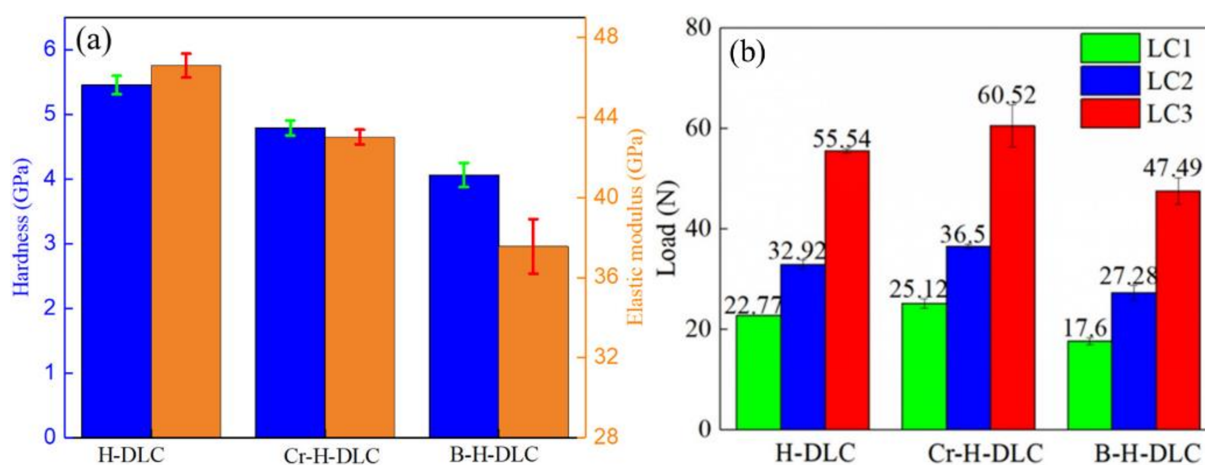

Figure 3-13. (a) the hardness of the a-C:H:Cr layers and (b) critical load during scratching (LC1, LC2, and LC3 represent the occurrence of the first microcrack, a significant portion of peeling flake and full coating removal, respectively) as a function of the doping agent (Figure adapted from [43]).

Furthermore, applying a bias voltage during film deposition can lead to improved ion bombardment of the growing film's surface. This ion bombardment removes less densely packed atoms, leading to an increase in film density and hardness. The degree of enhancement can be controlled by adjusting the bias voltage, making this technique valuable for tailoring the properties of thin films in various applications [105–107]. Moreover, the effect of C_2H_2 gas rate on tuning the mechanical properties of a-C:H films has attracted large attention. The research shows that a higher C_2H_2 proportion results in a lower hardness and elastic modulus. The reason for this negative effect of the C_2H_2 flow rate is that an increasing amount of C_2H_2 in the deposition chamber results in a higher H content within the a-C:H films. This leads to more terminating C-H bonds in the a-C:H structure, resulting in lower density, hardness, and elastic modulus [108]. Figure 3-14 illustrates the counterplot of the a-C:H films hardness and Young’s modulus plotted against the C_2H_2 flow rate and applied bias voltage. a-C:H films have been deposited by the industrial magnetron sputtering device using the C_2H_2 as the precursor gas.

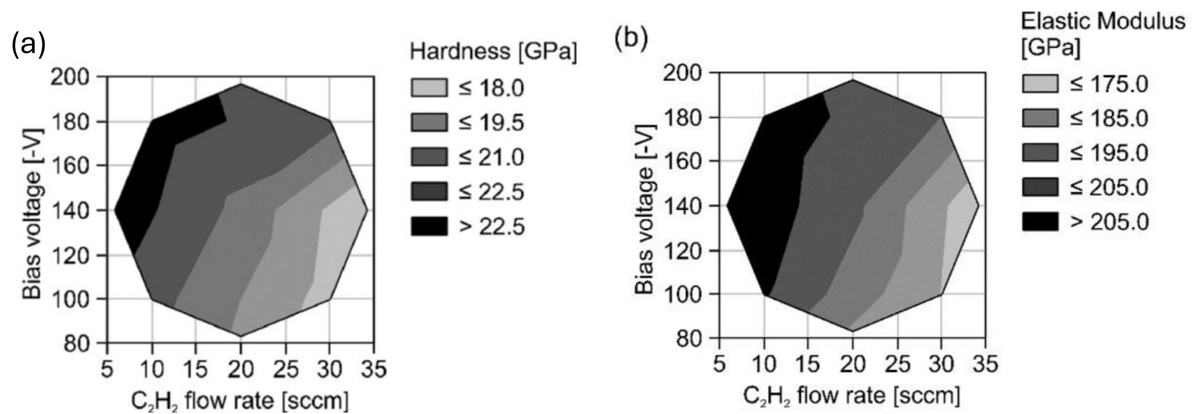

Figure 3-14. contour plot of the (a) hardness and (b) Young's modulus plotted against the C_2H_2 flow rate and applied bias voltage (Figure adapted from [108]).

The hardness and the elastic modulus of a-C:H coatings exhibit a tendency to increase with a decrease in the deposition pressure. It can be inferred that the amount of dissociation and ionization of the precursor gases is decreased by reduced deposition pressure because it results in a possibility of electrons and molecules colliding. Thus, in this near collisionless scenario, the lowest deposition pressures at which plasma stability can be achieved allow for an increase in the ion average energy while a reduction in the ion energy distribution. Another possibility is that the films' mass growth is significantly influenced by the neutral species in the plasma phase (radicals and intact molecules) at higher pressures. Although a-C:H group has lower mechanical properties than DLC or ta-C, these coatings are in use to protect magnetic storage media from wear and corrosion due to their superior scratch resistance, bearings, gears, seals, engine components, oil media, and operation under ultra-high vacuum conditions [109–111].

In their study, Xia *et al*. [112,113] suggest different approaches to compare the fracture toughness of a-C:H coatings. According to their results, in this coating class, they were able to tailor the fracture toughness by multilayering and manipulating the bias voltage. Fracture toughness values extracted from nanoindentation by employing the $K_{Ic} = \sqrt{\frac{UE}{1-\text{Ʋ}^2}}$ equation. Here U is the energy dissipation, E is the film's young's modulus, and Ʋ is the films' Poisson ratio (0.22 – 0.33). The fracture toughness varied between 1.24 and 2.09 $MPa.\sqrt{m}$ depending on increasing the number of sub-layers and/or bias voltage. A comprehensive study on a-C films has been conducted by Jonnalagadda *et al.* [114], indicating that fracture toughness in this group of the coating varies between 3.06 ± 0.17$MPa.\sqrt{m}$ and 4.4 ± 0.4 $MPa.\sqrt{m}$ where the average is 4.03 ± 0.74 $MPa.\sqrt{m}$ for the coatings with 70–80% sp^3 carbon bonding.

3.3.2. Mechanical properties of Cu-Zr based coatings

According to the previously done works, Cu-Zr based coatings have been customized majorly by tailoring the $\frac{Cu}{Zr}$ ratio during the deposition process. The effect of composition change in Cu-Zr TFMGs has been studied by Apreutesei *et al*. [72], Wang *et al*. [115], Rauf *et al*. [69], and Coddet *et al*. [71]. They all connected the reason for the increase in hardness and Young's modulus to the packing density of the final composition. Copper has smaller radii than Zirconium and can be packed more closely within a crystal lattice. Thus, increasing the Cu content in the composition will result in a more compact structure and, consequently, a larger packing density. Furthermore, arranging atoms in a full-icosahedral structure makes the composition more resistant to deformation and enhances its hardness [63].

Abboud *et al*. [116,117] studied the hardness behavior of $Cu_{45}Zr_{55}$/Zr film deposited on stainless steels. Their study shows that monolithic metallic glass/crystalline samples have higher hardness than pure nanocrystalline Cu. Also, they showed that adding the crystalline Cu layer will decrease hardness by increasing the layer thickness; however, the addition of Zr assists in keeping the hardness high even by increasing the thickness (Figure 3-15). A decrease in hardness by increasing the Cu layer can be explained by Hall & Petch's law, which states that by increasing the crystalline phase thickness, more dislocation nucleation and motion will influence the materials' hardness [116,118,119].

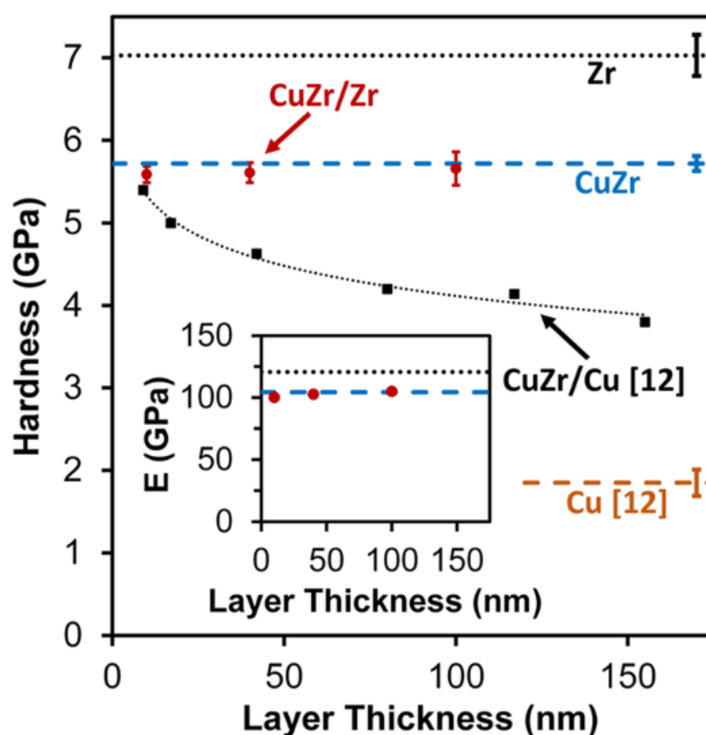

Figure 3-15. The hardness of $Cu_{45}Zr_{55}$/Zr nanolayers (red points). $Cu_{45}Zr_{55}$/Cu (black dot-lines with points) as a function of the thickness of the Cu or Zr layer. The hardness of nanocrystalline Zr (black

dot-lines), $Cu_{45}Zr_{55}$ thin film metallic glass (blue dash-lines), and Cu (orange dash-lines) is shown for comparison. The inset shows elastic modulus (*E*) values of Zr (black dot-lines), $Cu_{45}Zr_{55}$ (blue dash-lines), and $Cu_{45}Zr_{55}$/Zr (red points) using the same marker and line style convention as that of the main plot (Figure adapted from [116]).

Wang *et al.* [115], Jeong *et al.* [120], and Sun *et al.* [121] conducted studies on increasing the total film thickness from 100 nm to 300 nm (Figure 3-16). Regardless of composition, they found that the Cu-Zr TFMG hardness value decreased with increasing film thickness. The shear transformation zone (STZ) volume, which refers to the volume of a limited area inside a material where a shear transformation can take place, was identified as the cause of this phenomenon. The following are some of the main conclusions drawn from these investigations: Structure heterogeneity results from a decrease in STZ number but an increase in size as film thickness increases. The mechanical and plastic characteristics of the thin film are significantly influenced by the activation volume, which also controls a large amount of the mechanical properties. It was discovered that the STZ activation volume ranged from 2.5 to 6.6 nm.

These results imply that the mechanical properties of thin films are significantly influenced by the STZ activation volume and that comprehending this connection is essential to maximize the performance of various materials and devices.

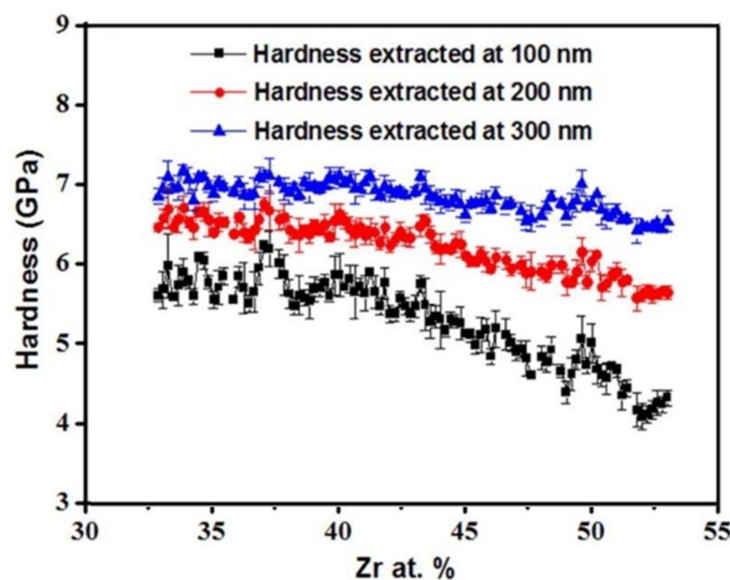

Figure 3-16. Hardness plot for different compositions in the binary Cu–Zr system, extracting at depths of 100, 200, and 300 nm using the Oliver–Pharr method (Figure adapted from [115]).

Despite the initial expectation that CuZr base TFMGs would exhibit exceptional wear resistance due to their high hardness, conflicting reports have emerged from research groups. This is because mechanical

softening caused by the rapid spread of secondary phases (SPs) often overshadows the potential benefits of high hardness. To address this issue, scientists have explored the use of multi-layers, such as MG/MG and/or MG/Crystalline architectures, to tune the friction coefficient. However, selecting the optimal composition is crucial. If the composition is not carefully chosen, multilayering can actually display the opposite trend. For instance, Abboud *et al.*[116] investigated the wear behavior relationships in CuZr monolithic TFMG and CuZr/Zr nano-layered coatings with layer thicknesses ranging from 10 to 100 nm.

Their results showed the scratch resistance was highest for the monolithic CuZr and decreased with decreasing layer thickness for nanolayered coatings, although hardness and modulus remained constant. Also, the interfacial delamination, in the form of buckling was observed in the nanolayered coatings. Since the interface between the CuZr and Zr layers is weak, having more interfaces facilitates plastic deformation and lowers the resistance to scratch penetration. The strain mismatch between the crystalline and amorphous layers, followed by the plastic deformation of the Zr layer, is likely to be the first cause of shear fracture at the interface and a decrease in the resistance to scratch penetration [122]. This interface-dominated wear pattern explains the maximum scratch resistance in CuZr without any interfaces and the scratch resistance monotonically declining with increasing interface density, as seen in Figure 3-17.

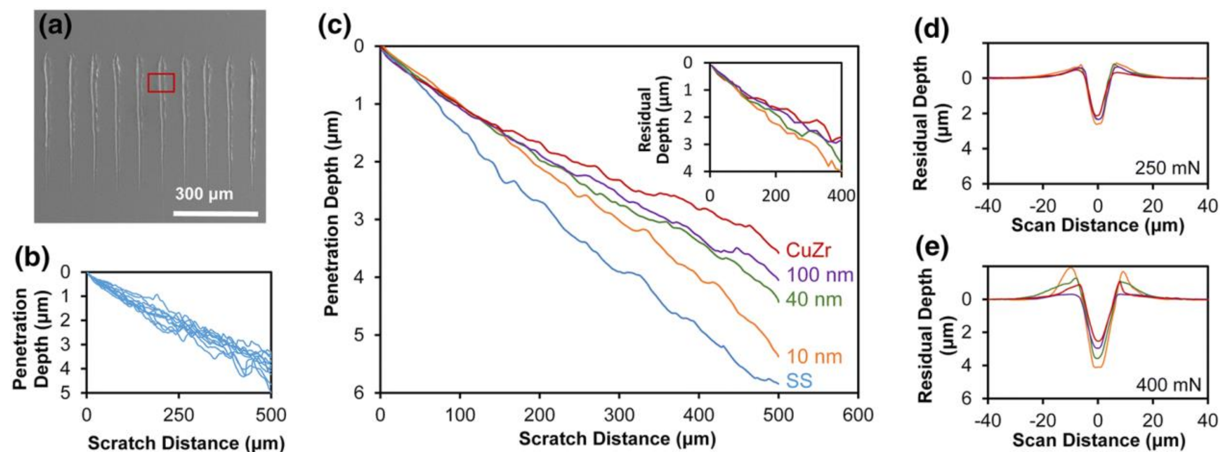

Figure 3-17. (a) SEM image of 10 scratches on CuZr/Zr-40. The red rectangle represents the region of FIB cross-sectioning. (b) 10 penetration depth profiles for CuZr/Zr-40 measured during scratch loading, demonstrating the repeatability of the measurements. (c) Penetration depth profiles for each sample were measured during scratch loading. The inset at the top right shows the residual scratch depths, as measured by AFM at ~ 20-μm intervals along selected scratches. (d, e) Scratch track profiles were measured by AFM on selected scratches at locations of 250 mN and 400 mN loading, respectively. (c–e) have the same color coding (Figure adapted from [116]).

The fracture toughness of $Zr_{51}Cu_{31}Al_{13}Ni_5$ TFMG has been studied by Li *et al.*[123]. For comparison, the same test was also carried out on bulk metallic glasses (BMGs), crystalline Ti thin films, and TiN thin films. Figure 3-18 reveals the load vs. deflection curves that were produced. Zr-based TFMGs, BMGs, and Ti films displayed nonlinear yielding behavior beyond the linear region of elasticity, which is indicative of ductile deformation. The following are the observed values for fracture toughness: Zr-based TFMG (3.84 $MPa.\sqrt{m}$), TiN (2.15 $MPa.\sqrt{m}$), and Ti (0.74 $MPa.\sqrt{m}$). The notch toughness method by including the geometric factor of $f(\frac{a}{W})$ has been employed for the fracture toughness calculation. The fracture toughness has been calculated using $K_{Ic} = \frac{F_{max}L}{BW^{3/2}} f(\frac{a}{W})$ equation where F_{max}, B, and L are the fracture loading, the width of the microcantilever, and the distance between the notch and loading point, respectively [124]. Regarding this study, Z-TFMG was shown to require more energy for the creation of fractures than were the other materials. Also, Z-TFMG and BMG microcantilevers presented ductile fracture behavior where TiN film has a brittle nature [125].

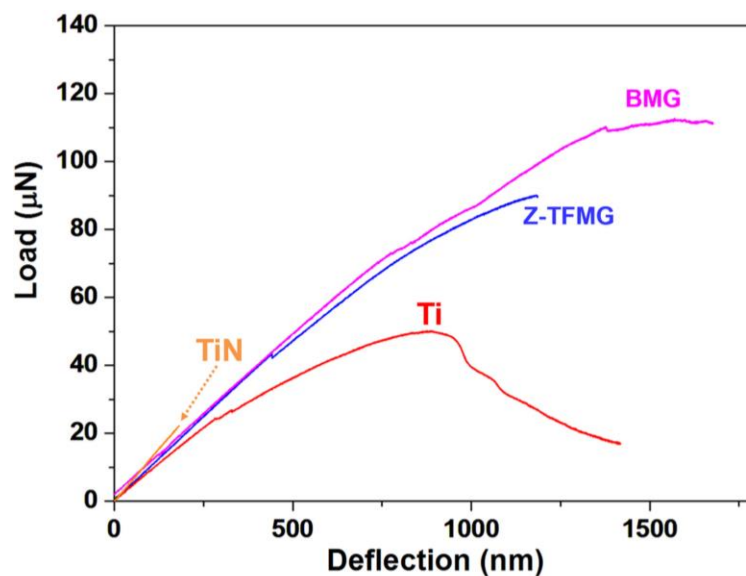

Figure 3-18. Typical load versus deflection curves of each microcantilever (Figure adapted from [123]).

The fracture toughness and energy release rate of $Cu_{67.8}Zr_{32.2}$ TFMG examined by micro-fracture experiments by Schnabel *et al.* [126] showed fracture toughness of 2.7±0.5 $MPa.\sqrt{m}$ and energy release rate of 60 J/m^2.

One approved and facilitated method to extract the fracture toughness of TFMGs is to relate it to the corrugation or vein width. In this method σ_y is the yield stress, and ω is the average size of corrugated patterns. Thus, the fracture toughness can be calculated from $K_{Ic} = \sigma_y\sqrt{40\omega}$ [127]. Liu *et al.* [128] have extracted the fracture toughness of Zr–Cu doped with Ni-Al–Hf–Ti thin film with this method,

where the value is 3.7 ± 0.4 $MPa.\sqrt{m}$.One crucial aspect we emphasize in this thesis is the omission of reporting the oxygen content in previous studies that examined the cross-sectional structure of Cu-Zr base TFMGs and described it as columnar. We believe it is essential to consider the oxygen content in the deposition process as it can significantly influence the coatings' microstructure, fracture behavior, and mechanical properties. Therefore, we critique the previous studies for not accounting for this crucial parameter, and experimentally, this study will show the driving force behind this phenomenon in Chapter 6.

3.4. General comparison of a-C:H and Cu-Zr based thin films

After a detailed discussion of each group, this section will discuss all characteristics of these two groups. This section generally compares these coatings' different aspects, from the production methods to the mechanical properties.

The first step to being able to name a coating as a desirable coating is the versatility of its production methods. Regarding the deposition method, a-C:H coatings are generally produced by the PECVD technique. However, Cu-Zr based TFMGs can be produced using a variety of methods, such as thermal evaporation, magnetron sputtering, and plasma laser deposition [129].

It is necessary to correctly choose the precursor gas (Methane, Acetylene, Butadiene, Cyclopentane, or Benzene) and control the gas flow during PECVD deposition to be able to get the desired properties [130]. Coating uniformity is another thing to be considered since it can be challenging and should be improved by tuning the deposition parameters such as deposition pressure, distance from the target, and gas flow, as discussed in [131–133]. Lastly, initial gas contamination or poor purity affects the final product of a-C:H coating [134,135]. However, besides these difficulties, low deposition temperature, high deposition rate, and ability to manipulate the coating chemistry are just a few advantages of this group [27]. Also, a-C:H coatings show better oxidation behavior than other metallic coatings during and after deposition [136,137].

Regarding the Cu-Zr TFMGs, keeping the amorphous nature of the coating was always challenging. They are prone to recrystallization and oxidation, and their composition should be controlled to be within the limit of the GFA region; otherwise, the crystalline coating will result instead of amorphous. Also, annealing, which is a well-known method to improve the mechanical properties of materials and decrease the residual stress, can cause the devitrification of these coatings [100,138–140].

Although producing these coatings requires high control and attention, raw materials availability and average price compared to other coatings materials (Pd, Ag, Ti, etc.) with very close properties being

used in applications like anticorrosion and flexible coating makes them a promising option in the industry [141–144].

In order to select the suitable coating for the desired application, a comparison of mechanical properties is necessary since each coating will not present the same behavior in different test conditions. Thus, in this section, the comparison of different conventional coatings have been showed by plotting ${}^{\sigma_y}/_{E'}$ against the fracture energy release rate (G_{Ic}) as an indicator of resistance to cracking and plastic deformation.

The comparison of fracture behavior of different coatings in the thin film industry is inserted in Figure 3-19. It has been proved that coatings with higher G_{Ic} are resistance to cracking initiation and propagation, which can benefit barrier coatings on polymer substrates, thermal barrier coatings, and any coatings exposed to high tensile stress to prevent crack opening [145,146]. Conversely, coatings with higher ${}^{\sigma_y}/_{E'}$ ratio can undergo huge elastic deformation before permanent plastic deformation, allowing expansion and contraction in different applications [147].

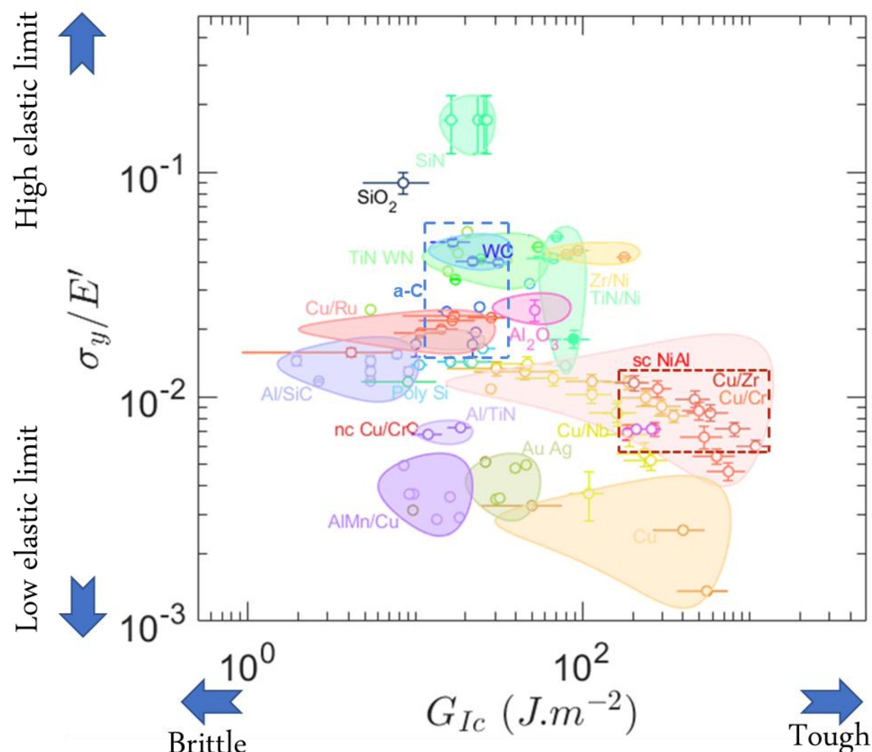

Figure 3-19. The materials property map presents the elastic limit against the critical energy release rate. The results are obtained from the literature where a-C are shown with blue dot lines and Cu-Zr based metallic glasses with red dot lines [114,127,148–162].

According to the literature review, it is notable that a-C coatings will provide higher elastic limits than Cu-Zr thin films, indicating their ability to withstand higher stress levels and deformation without undergoing permanent plastic deformation, as was expected due to their polymeric nature. On the other hand, Cu-Zr based TFMGs provide a larger fracture energy release rate (>100 J/m^2) than a-C coatings (10-40 J/m^2), indicating their ability to resist crack propagation and absorb larger energy before failure and durability [114,127,148–162].

Although a-C:H thin films show extraordinary properties in ambient conditions, however, they are unsuitable coatings for high-temperature applications, and their hardness will decrease by increasing the temperature. The reason is increased graphitization degree and loosest sp^2 bonds in the coating. This will result in a decrease in the wear resistivity of a-C:H coatings [108,163]. However, Cu-Zr based thin films improve hardness, wear resistance, and thermal stability over time. It is believed that oxidation in this coating group causes the nucleation and dispersion of ZrO_2 oxides and crystals, increasing the materials' hardness. It illustrates the benefits of using this group in industries requiring longer durability under high working temperatures [70,164,165].

3.5. Summary

This chapter explored the fascinating field of amorphous materials and emphasized the key distinctions between amorphous and crystalline solids. Additionally, it focused on the a-C and Cu-Zr TFMG subgroups of amorphous thin films.

This chapter analyzed the mechanical and tribological performance of the abovementioned coatings groups, illuminating their distinctive characteristics, microstructures, and the variables affecting their performance.

It provided a comprehensive comparison of two groups based on the literature review and showed Cu-Zr-based thin films may be used in applications that need more durability before cracking due to their higher fracture energy release rate and elevated working temperature. On the other hand, a-C films can be used in applications asking for more significant elastic deformation before permanent plastic deformation but below hundreds of degrees centigrade

Chapter 4.

4. Methodology

This chapter provides background knowledge and insights into the production methods and necessary analysis methodologies needed to achieve our goal in this thesis.

The research leading to this thesis has focused on the deposition and analysis of a-C:H:Cr and Cu-Zr thin films. Thus, structure, chemical bonding, mechanical properties, and other material properties have been characterized for the deposited films. This has been done by several techniques, where the author has deposited all of the samples and performed most of the analysis, e.g., X-ray diffraction (XRD), X-ray photoelectron spectroscopy (XPS), scanning electron microscopy (SEM), atomic force microscopy (AFM), Raman spectroscopy, and the majority of mechanical properties while transmission electron microscopy (TEM) and some of the mechanical properties including micro-scratch test and tensile testing have been performed in collaboration with other researchers from UCLouvain and UAntwerpen.

4.1. Thin film deposition

4.1.1. a-C:H:Cr thin film deposition

In this work, a-C:H:Cr films with 10 at% of Cr (added intentionally in order to decrease the film residual stress and improve the wear resistance, adhesion, thermal stability, and fracture toughness), and around 30 at% of hydrogen content (presence due to using the C_2H_2 as a precursor gas) were deposited on Si (100) wafers and on 13 µm and 25 µm thick HN type Kapton substrates using PECVD magnetron sputtering in DC pulsed mode. This process uses a glow discharge to break down the gas precursor (such as methane or acetylene) into various (metastable) neutral species, including CH_3, CH, and H, as well as ions like CH^{3+}, CH^+, C^+, and H^+. Silicon substrates were ultrasonically cleaned in soap and de-ionized water and dried with hot air prior to deposition. The polymer substrates were used as received by the supplier. A base pressure of 10^{-6} Torr was created prior to deposition. Then, a 10 min Cr target cleaning with 1.2 kW power was performed under a pure Ar atmosphere. Cr targets (7.5x35cm, purity 99.8 %, Nova fabrica) have been sputtered in argon and acetylene (C_2H_2) mixed atmosphere (150 sccm Ar/160 sccm C_2H_2) under different deposition conditions (5 mTorr, 20 mTorr sputtering pressure, floating or -100V bias voltage). Mentioned parameters have been selected as optimum in this study after examining several deposition parameters, including 2, 5, 10, 20 mTorr and 0V, -50V, -100V, -150V, -200V bias voltage. The gas flow rate was controlled by FloTron multi-channel reactive gas monitoring system. A bipolar pulsed power supply with a frequency of 1250Hz and a pulse duration of 300 µs on /100 µs off was used (duty cycle of 75%). 3-fold sample rotation around the Z axis and 2 rpm table rotation speed have been applied to generate homogeneous coating. The deposition was done at room temperature. The film thickness was kept around 1 µm, i.e. sufficiently thick to perform relevant mechanical tests. Figure 4-1 shows the schematic designs for the PECVD technique used in this project.

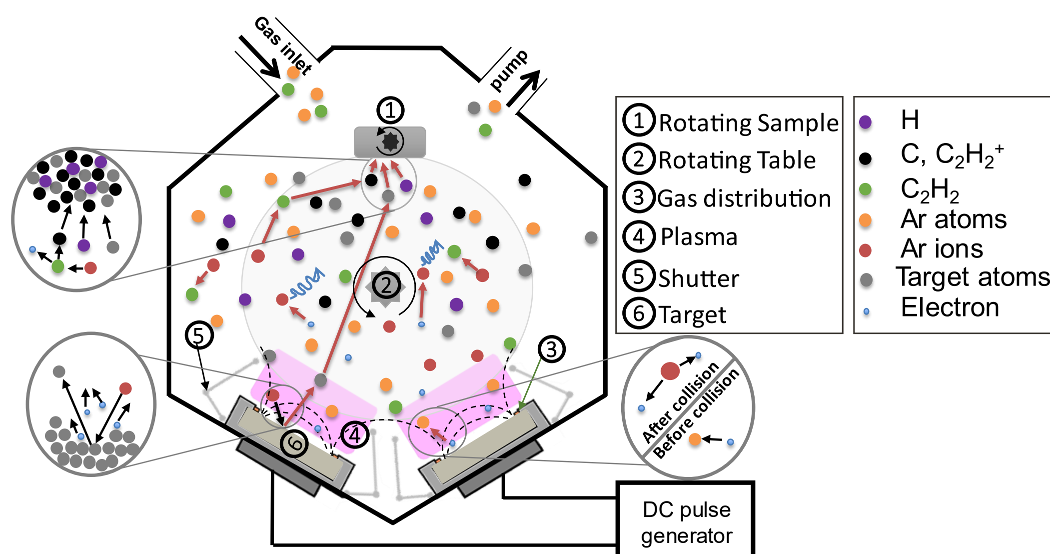

Figure 4-1. Schematic of the deposition process for a-C:H:Cr film deposition with magnetron coater.

As shown in this figure, Ar (argon) and C_2H_2 (acetylene) gases are introduced into the chamber through the gas inlet valve controlled by the FloTron. The inset to the figure (bottom right) illustrates the ionization of Ar atoms after colliding with the electrons, resulting in the creation of Ar^+ and secondary electrons. Later, Ar^+ collides with the target material's surface (chromium in this study) due to the potential difference between the target and Ar^+, ejecting Cr atoms (inset to figure in the bottom left-hand side). These ejected Cr atoms then travel towards the substrate and deposit onto the substrate surface, as shown inset to figure in the top left-hand side. Furthermore, the Ar^+ also plays a major role in decomposing the C_2H_2 precursor gas and giving rise to the a-C:H film growth. A detailed explanation of the sputtering process is discussed in section 2.1.2.

4.1.2. Cu-Zr thin film deposition

The Cu-Zr films were deposited on Si (100) wafers using magnetron sputtering with pure metallic Zr (99.999%) and pure Cu (99.95%) targets in DC mode. Silicon substrates were ultrasonically cleaned in soap and de-ionized water and dried with hot air prior to deposition. A base pressure of 10^{-6} Torr was created prior to deposition. Then, a 10 min target cleaning with 400-800 W power was performed under a pure Ar atmosphere. Cu target (7.5x35cm, purity 99.95 %, Neyco) and Zr target (7.5x35cm, purity 99.4 %, Nova fabrica) have been sputtered in argon atmosphere (150 sccm Ar) under different deposition conditions (5 mTorr, 20 mTorr sputtering pressure, floating or -100V bias voltage). Another set of samples has been sputtered in Argon and Oxygen atmosphere (150 sccm Ar/3, 5, 7 sccm O_2) under 5 mTorr / -100 V bias condition. Mentioned parameters have been selected as optimum in this study after examining several deposition parameters, including 2, 5, 10, 20 mTorr, 0V, -50V, -75V, -

100V, -150V, -200V bias voltage, and 0, 3, 5, 7, 10 sccm O_2 injection. Due to poor amorphization and adhesion of other samples, only the above-mentioned samples have been selected. The gas flow rate was controlled by FloTron multi-channel reactive gas monitoring system. 2-fold sample rotation around the Z axis and 2 rpm table rotation speed have been applied to generate homogeneous coating. The deposition was done at room temperature (Figure 4-2).

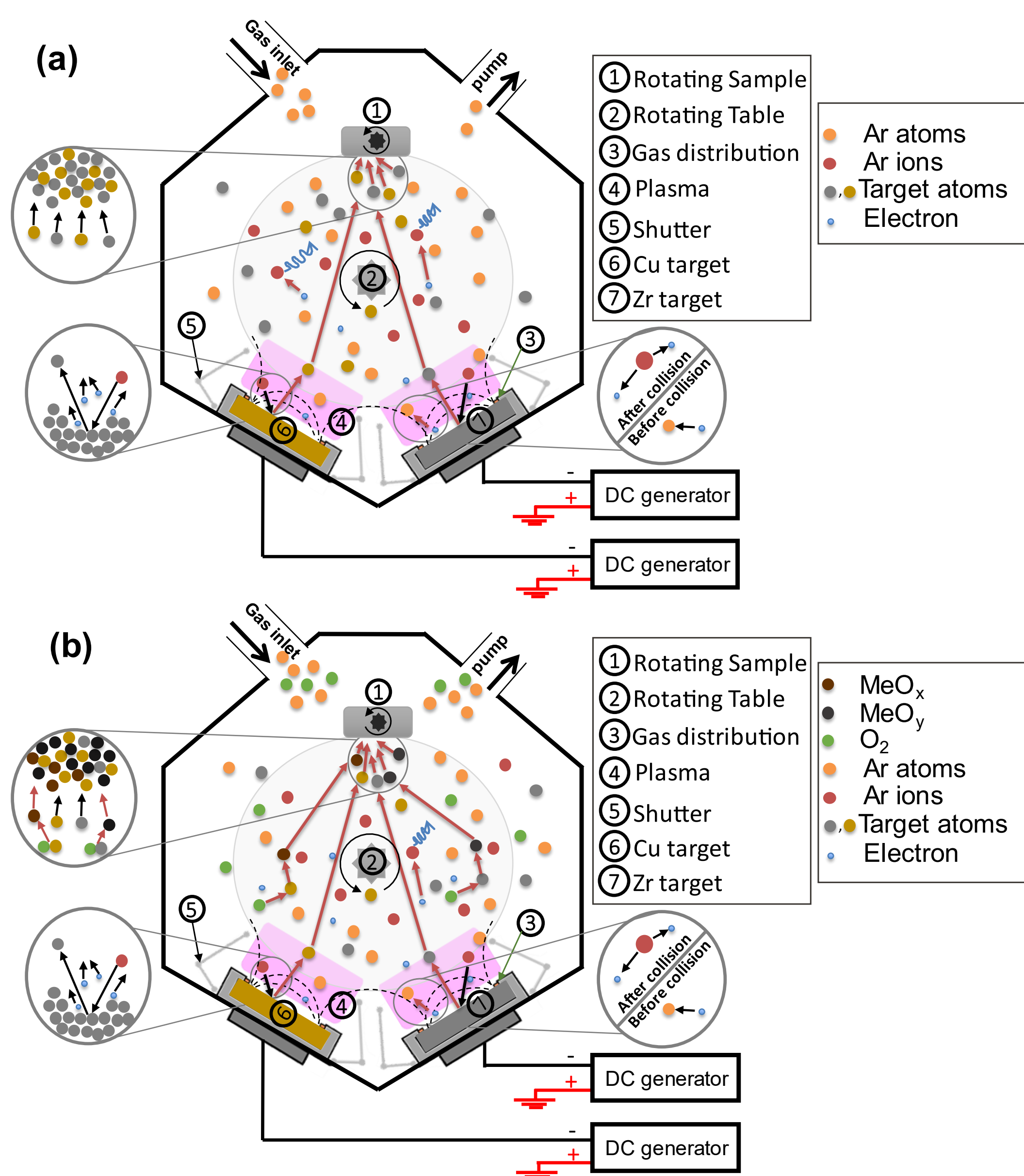

Figure 4-2. Schematic of the (a) magnetron sputtering and (b) reactive magnetron sputtering process for Cu-Zr film deposition.

As shown in this figure (Figure 4-2 a) Ar (argon) gas and (Figure 4-2 b) Ar (argon) along with O_2 gas, are introduced into the chamber through the gas inlet valve. The inset to the figure (bottom right)

illustrates the ionization of Ar atoms after colliding with the electrons, resulting in the creation of Ar^+ and secondary electrons. These Ar^+ collide with the target materials' surface (Copper and Zirconium in this study) due to the potential difference between the target and Ar^+, ejecting Cu an Zr atoms (different ratios regarding their sputtering yield). These ejected atoms then travel towards the substrate and deposit onto the substrate surface, as shown inset to figure in the left hand side. Furthermore, the Ar^+ also plays a role in decomposing the O_2 gas, leading to the growth of the metal oxide film. A detailed explanation of the sputtering process is discussed in section 2.1.2.

4.2. Thin film microstructure investigation

4.2.1. X-Ray Diffraction (XRD)

In this study, PANalytical X'Pert PRO diffractometer is used in the 2θ-ω configuration to remove the background caused by the silicon substrate. The angle between the incident X-ray beam and the detector forms an angle of 2θ and the ω angle represents the angle at which the X-ray beam hits the sample. Monochromatic $\mathrm{Cu} - k_\alpha$ Wavelength $\lambda = 0.15406$ nm has been used as the X-ray source. The device has been operated at 45 kV and 30 mA. Because of this configuration, the thickness probed is several µm of thickness, and the area measured is several mm^2.

4.2.2. X-Ray Photoelectron Spectroscopy (XPS)

In this work, depth profiling mode using a monochromatic X-ray source (Al Kα radiation 1486.6 eV, spot size of 250x250 µm), and an Ar^+ erosion gun, working at 2 keV (raster size of 1.25x1.25 mm, incident angle of 30°), on ThermoFisher K-alpha spectrometer has been used. The chamber pressure before the acquisition was below 1.5×10^{-9} Torr. A flood gun has been used during analysis, preventing eventual charging effects. Accumulated charge on the sample surface can cause binding energy shifts and peak distortions, impacting data accuracy. Thus, data resolution will be improved by neutralizing the accumulated positive charges by using a flood gun during the analysis. No further energy shift is applied to the signal. Each level of elements is collected using snapshot mode (pass energy 147eV, 10 snaps), where the detector measures a set of energy channels determined by the pass energy of the analyzer in parallel. The reason for utilizing this mode in our study is the advantages of this method over serial acquisition (scan mode). The main advantages that can be mentioned are the enhanced resolution and significantly faster data collection without sacrificing sensitivity (a 256×256 pixel image may be acquired in seconds) [166–168]. To obtain the composition depth profile, the peak area of each level is measured after subtracting the Shirley background (the background produced by electrons that are inelastically dispersed), which enables precise peak intensity measurement and quantitative analysis [169]. All XPS data are computed using Avantage v.5.9916 Build 06625 software.

4.2.3. Scanning Electron Microscopy (SEM)

The coating thickness, surface morphology, and cross-sectional growth observation of deposited samples on silicon and kapton substrates were determined based on ZEISS Ultra 55 Field Emission Gun–Scanning Electron Microscope (FEG-SEM) with high efficiency in-lens detector. An electron high tension (EHT) of 5 kV in in-lens and SE modes has been generated to capture clear and less electrostatically distorted images of nanostructures.

4.2.4. Transmission Electron Microscopy (TEM)

The crystalline microstructure of the samples has been determined by TEM, including selected area electron diffraction (SAED), high-resolution transmission electron microscopy (HRTEM), and energy dispersive X-ray spectroscopy (EDXS), on Thermo Fisher Tecnai Osiris microscope operated at 200 kV. The microscope is equipped with an Extreme Field Emission Gun (XFEG) electron source and a highly efficient Super-X system[1] to acquire high-resolution energy dispersive X-ray (EDX) maps at low doses with a short exposure time. Prior to TEM imaging, a Thermo Fisher Helios Nanolab 650 dual-beam SEM/FIB (focused ion beam) instrument was used to produce electron-transparent thin foils out of the samples. The Platinum protection layer was locally deposited on the cut area in two electron beam steps, followed by an ion beam, followed by an ion beam. This is being applied to protect the sample contamination. The FIB foils were then thinned to a thickness lower than 50 nm with a 2 kV/0.2 nA ion beam.

4.2.5. Raman Spectroscopy

Raman spectroscopy was performed in the backscattering configuration using a LabRam HR 800 confocal laser system with a laser wavelength λ = 514 nm and a 2400 gr/mm grating. The spectral resolution for this configuration is ≈ 0.5 cm^{-1}. In order to avoid local heating and allow accurate measurement, the laser power was set to 10% of the maximum (20 mW) working power.

4.2.6. Atomic Force Microscopy (AFM)

AFM measurements were performed in air, using the soft tapping mode of a Nanoscope III from Veeco Instruments (Santa Barbara, CA, USA). Images were recorded in 4×4 μm^2, and 2×2 μm^2 sizes with 512×512 lines per image and a scan rate of 1Hz. The average of 3 measurements for each sample has

[1] It is intended to deliver superior performance in terms of spectrum purity, quantification, and compositional mapping.

systematically been used. The silicon cantilever (Nanosensors PPP-NCHR) with a resonance frequency of 290 kHz and a typical spring constant of around 42 N/m has been used for analysis. The tip has a nominal radius lower than 10 nm. The ratio between the set-point amplitude and the free amplitude of the cantilever vibration was always kept above 0.8 to guarantee sufficient contact between sample surface during scanning. The topographic analysis of AFM images regarding surface roughness was carried out using the Gwyddion software version 2.59.

4.3. Thin film mechanical properties

4.3.1. Nanoindentation and micro-scratch test

In this thesis, the hardness, Young's modulus, and apparent activation volume have been determined by nanoindentation using a G200 nanoindenter (KLA Tencor) equipped with a Dynamic contact module (DCM) II head with 50 nN and 0.01 nm of force and vertical displacement resolution, respectively. A diamond Berkovich tip has been used, and the tip area function has been calibrated using a fused silica reference. The nanoindentation measurements were performed at room temperature, under the load-control mode, with an exponential loading in order to produce a constant strain rate of $\dot{P}/P$ =0.05 s^{-1}. The thermal drift rate has been limited to 0.05 nm s^{-1} before each experiment to ensure a negligible effect on the measured displacement. Sixteen indents were made within each sample for statistical analysis and consistency inspection. The measurements were carried out using the continuous stiffness measurement (CSM) technique providing continuous hardness and Young's modulus with increasing indentation depth. The hardness and modulus were calculated using the Oliver and Pharr model [170]. Also, Young's modulus of the film was corrected from the substrate effect using the model proposed by Hay and Crawford [171].

In order to extract the apparent activation volume, constant contact stiffness relaxation tests have been performed with a holding duration of 30 min and a maximum penetration depth of 90 nm. As a result, the activation volume V^* extracted from nano-indentation can be stated as follows, according to Gu *et al.* research [172]

$$V^* = 3\sqrt{3}kT\frac{\partial ln\varepsilon_i}{\partial H}, \quad (4\text{-}1)$$

where ε_i stands for the indentation strain rate, k represents Boltzmann's constant, and T is the testing temperature. The corresponding experimental procedure and data processing are explained in more detail in [173,174].

Micro-scratch experiments were performed using a G200 nanoindenter (KLA Tencor) with a XP head equipped with a lateral force measurement. This setup allows the measurement of the coefficient of

friction during scratch. The XP head has a maximum normal force of 500 mN. A sphero-conical diamond tip with a radius of 5 µm and 90 degrees cone equivalent angle was used to perform the tests. Experiments involve applying a linear axial loading from 0 to 100 mN while sliding the indenter tip on 600 µm distance with a velocity of 30 $\mu m.s^{-1}$. The sample surface along the scratch path was scanned at low load (20 µN) with the indenter tip before and after the experiment to assess the surface roughness and topology before and measure the residual profile afterward. For each sample, a set of 8 scratches has been performed. SEM observed scratch grooves to characterize the failure mechanisms along the wear track.

4.3.2. Fracture toughness and crack density

The fracture toughness of films has been characterized by deforming the films deposited on polymer substrates under traction. Before film deposition, the polymer sheet was cut into tensile specimens using a punch. The geometry of the specimens is shown in Figure 4-3. In-situ optical microscope and SEM tensile tests were performed with a Gatan micro testing machine with a maximum force of 2 kN and displacement rate of 0.1 mm/min. All experiments were performed at room temperature.

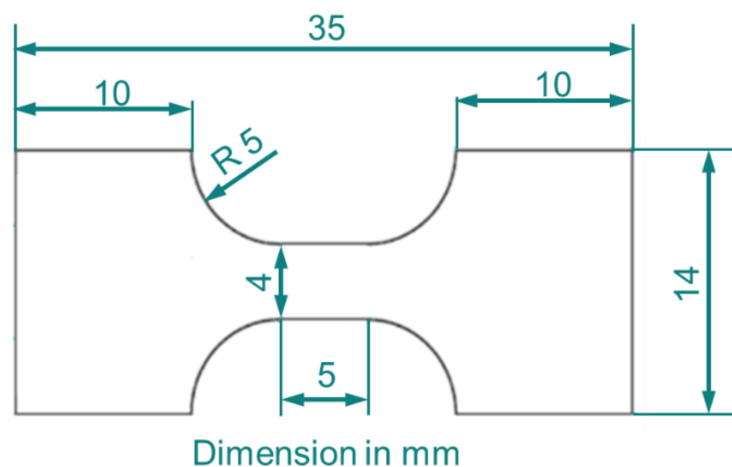

Figure 4-3. Specimen geometry for tensile testing of a-C:H:Cr films on kapton.

The cracking behavior was characterized with two different techniques. An in-situ SEM imaging during the traction was used to characterize the crack propagation and crack saturation density. An ex-situ optical microscopy technique also has been employed to characterize the fracture toughness of the films. In-situ SEM tests require interrupting the test for imaging, which leads to some spurious creep in the polymer substrate. It has been shown in the literature that test interruption can lead to crack propagation even when the mode I stress intensity factor (K_I) remains below the critical value (K_{Ic}) of the film [175]. Meanwhile, in-situ SEM tensile tests have been used to accurately determine the saturation crack

density (ρ_{sc}), i.e. the maximum crack density reached when pulling on the specimen. In-situ SEM tests were initially stopped every 50 µm of crosshead displacement until 400 µm in order to take images at various magnifications. After the first 400 µm of displacement, the experiment was stopped every 100 µm of displacement until a total crosshead displacement of 1 mm. Two images per second were acquired during in-situ optical microscope tensile test at a magnification of 200x with a resolution of 1272x952 pixels which ensures looking at the whole specimen gage length while seeing the cracks. These parameters are well suited to observe crack propagation and calculate the critical fracture energy release rate G_{Ic} from

$$\boldsymbol{G_{Ic}} = \frac{\boldsymbol{Z\sigma_f^2 h_f}}{\boldsymbol{E'_f}}, \qquad (\mathbf{2})$$

where Z is a dimensionless parameter that depends on the elastic mismatch between the film and substrate, σ_f is the fracture stress in the film, h_f is the film thickness and $E'_f = E_f/(1-\nu^2)$ is the plane strain Young's modulus. The Z factor depends on the Dundurs parameter α as defined in [176] and on the substrate/film thickness ratio [177]. The stress inside the film is obtained from Young's modulus and from the strain at which the first crack is propagating, assuming the film behaves as a linear elastic material and using Young's modulus extracted by nanoindentation. This will turn out to be a reasonable hypothesis with respect to the level of strain that is reached when looking at the literature [178,179]. The fracture strain (ε_f) is measured by following the displacement of small asperities on the images located close to the end of the gage region of the specimen. Note that the residual stress of a-C:H:Cr is considered as equal to zero because the soft polymer substrate rapidly relaxes this stress, on the contrary to the condition impressed by a Si substrate. Finally, equation (2) can be rewritten as

$$G_{Ic} = Z h_f E'_f \varepsilon_f^2, \qquad (3)$$

and the related stress intensity factor K_{Ic} as

$$K_{Ic} = \sqrt{G_{Ic} E'_f}, \qquad (4)$$

Despite the possibility of extremely high fracture toughness, the relatively high yield strength causes a reduction of the size of the fracture process zone, d, ahead of the crack tip [180]. The fracture process zone size, d, is defined as

$$d = \frac{{K_{Ic}}^2}{\pi {\sigma_y}^2}, \qquad (5)$$

where σ_y is the yield strength of the film.

In this chapter, the basics and comprehensive explanation of each technique, from materials characterization that unveils the essence of our materials' composition and structure to the mechanical properties that resonate with the soul of our research, have been discussed. An in-depth exploration of our methodology can also be found in Chapter 9 (annex).

Chapter 5.

5. Tailoring mechanical properties of a-C:H:Cr coatings

This chapter contributes a novel approach to crafting tunable coatings based on the fracture toughness and elastic limit that is vital for diverse technological applications with varying needs. This novel approach replaces traditional trial-and-error methods with a rational material selection technique.

Abstract

The development of coatings with tunable performances is critical to meet a wide range of technological applications each one with different requirements. Using the plasma-enhanced chemical vapor deposition (PECVD) process, scientists can create hydrogenated amorphous carbon coatings doped with metal (a-C:H:Me) with a broad range of mechanical properties, varying from those resembling polymers to ones resembling diamond. These diverse properties, without clear relations between the different families, make the material selection and optimization difficult but also very rich. An innovative approach is proposed here based on projected performance indices related to fracture energy, strength, and stiffness in order to classify and optimize a-C:H:Me coatings. Four different a-C:H:Cr coatings deposited by PECVD with Ar/C_2H_2 discharge under different bias voltage and pressure were investigated. A path is found to produce coatings with a selective critical energy release rate between 5 – 125 J/m2 without compromising yield strength (1.6-2.7 GPa) and elastic limit (≈0.05). Finally, fine-tuned coatings are categorized to meet desired applications under different testing conditions.

Keywords: Chromium-doped hydrogenated amorphous carbon, Magnetron sputtering, Tensile testing, Fracture toughness, Hardness, Materials selection.

This chapter has been published as a scientific paper in the journal of Coatings:

***Bagherpour A**, Baral P, Colla MS, Orekhov A, Idrissi H, Haye E, Pardoen T, Lucas S. Tailoring Mechanical Properties of a-C:H:Cr Coatings. Coatings. 2023 Dec 14;13(12):2084.*

5.1. Introduction

Amorphous carbon (a-C) films have been intensively studied over the last decades. In particular, the family of a-C:H coatings deposited by vacuum technology has shown outstanding and tunable mechanical [181,182], chemical [22,25], and biological protective properties such as high hardness, low friction, and high wear resistance [96,183]. The ability to modify properties by varying the deposition conditions makes them attractive candidates for tuning performances as a function of the applications e.g. flexible a-C films for protection of flexible substrates, wear resistant a-C films for hard discs, read–write heads, cutting tools, and ball bearings for space applications [96,184,185].

Among the other deposition methods, PECVD allows tuning the physical and chemical properties of films by varying the deposition parameters, including the pressure and gas composition in the chamber. Besides, the chemical structure is affected by the magnitude of the impinging energy of the ions. Hence, PECVD is a good candidate for a-C:H film deposition with tunable properties, from polymer-like to diamond-like behavior [186–188]. Among the different sources for a-C:H deposition by PECVD, acetylene (C_2H_2) has received more attention. C_2H_2 is often used for deposition thanks to the overall high electron-molecule cross-section leading to high deposition rates [189–192].

When internal stress is an issue, several studies have shown that adding metal elements in the films decreases the magnitude of the (tensile) internal stress and improves the wear resistance, adhesion, thermal stability, and fracture toughness. The rise in sp^2 graphitization by doping metal elements, along with partly hard carbide phase dispersion in amorphous carbon explains this phenomenon [193,194]. Among many metallic elements, chromium (Cr), in combination with carbon, presents attractive mechanical properties (especially stable friction performance and toughness) in a-C coatings [194–196].

Nanoindentation provides high resolutions on both forces and displacements, being an effective method for determining the mechanical response of materials [197] and extracting among others, the elastic modulus, hardness, and activation volume of a coating lying on a substrate. The apparent activation volume (V^*), which quantifies the rate deformation process is used to determine the elementary volume of material that experiences plastic deformation revealing the nature of the underlying deformation mechanism [173,174].

Although a large fraction of the research is concentrated on hard materials, some polymeric materials may offer outstanding wear resistance even with low hardness and Young's modulus. The elastic strain limit (σ_y/E') must be considered in addition to the resistance to plastic deformation. The ratio of (σ_y^3/E'^2) is a good indicator of wear resistance associated with plastic mechanisms [198]. Both high

$\sigma_y/_{E'}$ and $\sigma_y^3/_{E'^2}$ are needed to ensure high wear resistance, which fracture must be associated to G_{Ic} under low to medium contact pressure [194].

This research aims at understanding further how the deposition parameters affect the mechanical characteristics (both effective and intrinsic) of thin a-C:H:Cr films with thickness in the 1 μm range in order to build a rational coating selection strategy to further optimize the systems. To this end, we capitalized on the previous work by our group [183,199–201] to demonstrate how a-C:H:Cr films can be produced with tailored mechanical properties, specifically strength and fracture toughness by varying only the deposition conditions in C_2H_2 magnetron-assisted discharge. Because of the ionic nature of the condensing species in such a setup, one can easily understand that substrate biasing is one of the methods to produce films with different properties, as well as traditional pressure variation. Four films have been selected as representative candidates for this study and characterized by a panoply of techniques including X-ray Photoelectron Spectroscopy (XPS) to extract the coating's chemical composition; Atomic Force Microscopy (AFM) and Scanning Electron Microscopy (SEM) to observe the structural and morphological properties of the films; Transmission Electron Microscopy (TEM) and X-ray diffractometer (XRD) to investigate the amorphous microstructure of the coating; Raman Spectroscopy to track structural variation; nanoindentation to determine the hardness, Young's modulus, and activation volume; micro-scratch test to extract wear resistance, critical load, as well as tensile tests on a supporting polymer membrane to determine the fracture toughness of the coating. Comparison and deeper discussion are made through analyzing materials property map presenting the ratio of yield strength over Young's modulus against critical fracture energy release rate for several materials. The performances are shown to position extremely well compared to other available coatings for various applications asking for high yielding strength, high critical load under scratching conditions, and elastic limit, with a wide range of critical energy release rate.

5.2. Results

5.2.1. Structure, composition and surface morphology

The microstructure of the a-C:H:Cr films under different deposition conditions (5 mTorr, 20 mTorr sputtering pressure, floating or -100V bias voltage) have been studied by XRD and TEM analysis. X-ray diffractograms of the films detected no crystallinity in the coatings showing a fully amorphous nature of the films. The high-resolution micrograph and SAED pattern from TEM also confirm the amorphous character of the deposited films (see Figure 5-1).

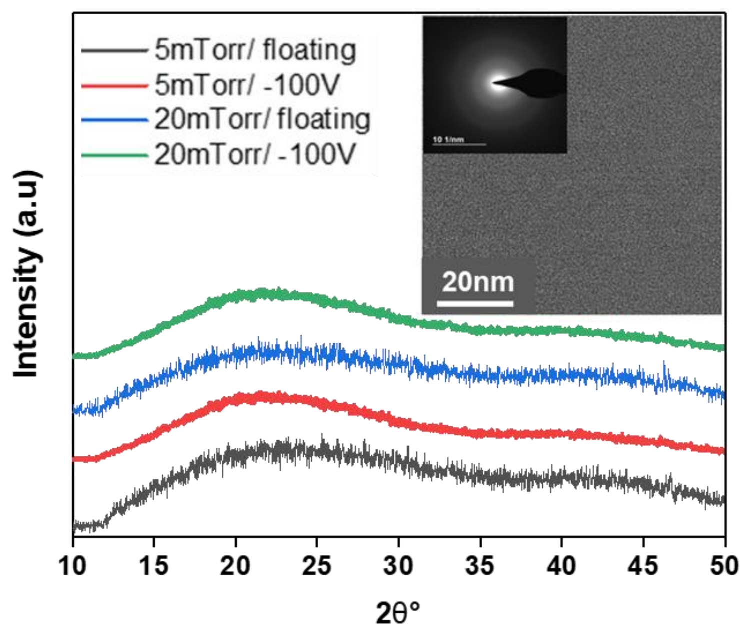

Figure 5-1. XRD pattern of the as-deposited amorphous films with different deposition conditions. The inset shows the high resolution TEM micrograph and a diffraction pattern typical of amorphous film.

Figure 5-2 displays the Raman spectra of the films. Each Raman spectrum was fitted into two Gaussian peaks. When applying a bias voltage, a small shift to the lower wave number is observed in the positions of the G peak (≈ 12 cm^{-1} and ≈ 6 cm^{-1} for 5 mTorr and 20 mTorr, respectively). A decrease in the ratio of the D-band intensity to that of the G-band (I_D/I_G) and the G-band position are both indicators of lower hydrogen content and a rising sp^3 content, respectively [202–204].

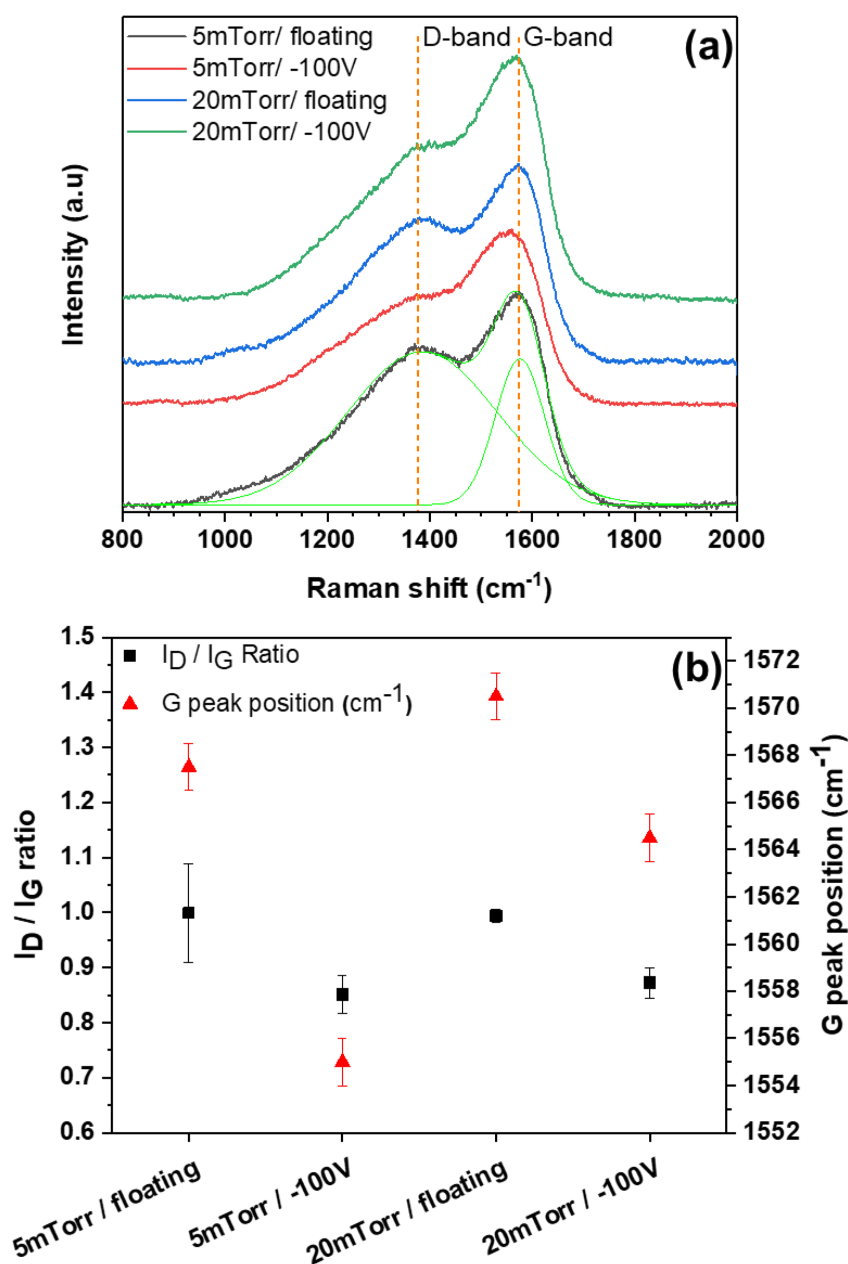

Figure 5-2. (a) Raman spectra of the a-C:H:Cr films. (b) Variation of the I_D/I_G intensity ratio and the G peak positions under different deposition conditions.

The chemical composition of the films as a function of depth has been obtained by XPS analysis and ERD analysis. A comparison of the chemical composition of the films as a function of the applied bias voltage and deposition pressure is illustrated in Figure 5-3. The C content slightly increases, whereas the oxygen (O) content decreases with increasing applied bias voltage at constant amount of Cr for both groups. The presence of higher oxygen content through the film is associated with the low deposition power and bombarding of the substrate with lower energy than usual in order to prevent overheating of

the Kapton substrate as well as the recrystallization of the a-C:H:Cr films. The decrease in O content with increasing bias voltage is known as a preferential sputtering effect, which removes adsorbed oxygen during film growth. When the bias voltage increases, the sputtering and etching energy of ions or atoms increase, and atoms' movement to the growing surface is enhanced. Due to the high deposition energy, C and Cr atoms are strongly bonded to the surface. Thus, weakly bonded O adatoms would be more easily re-sputtered by incident high-energy ions in the growth process of the films. This leads to dismissed O being replaced by C atoms [205].

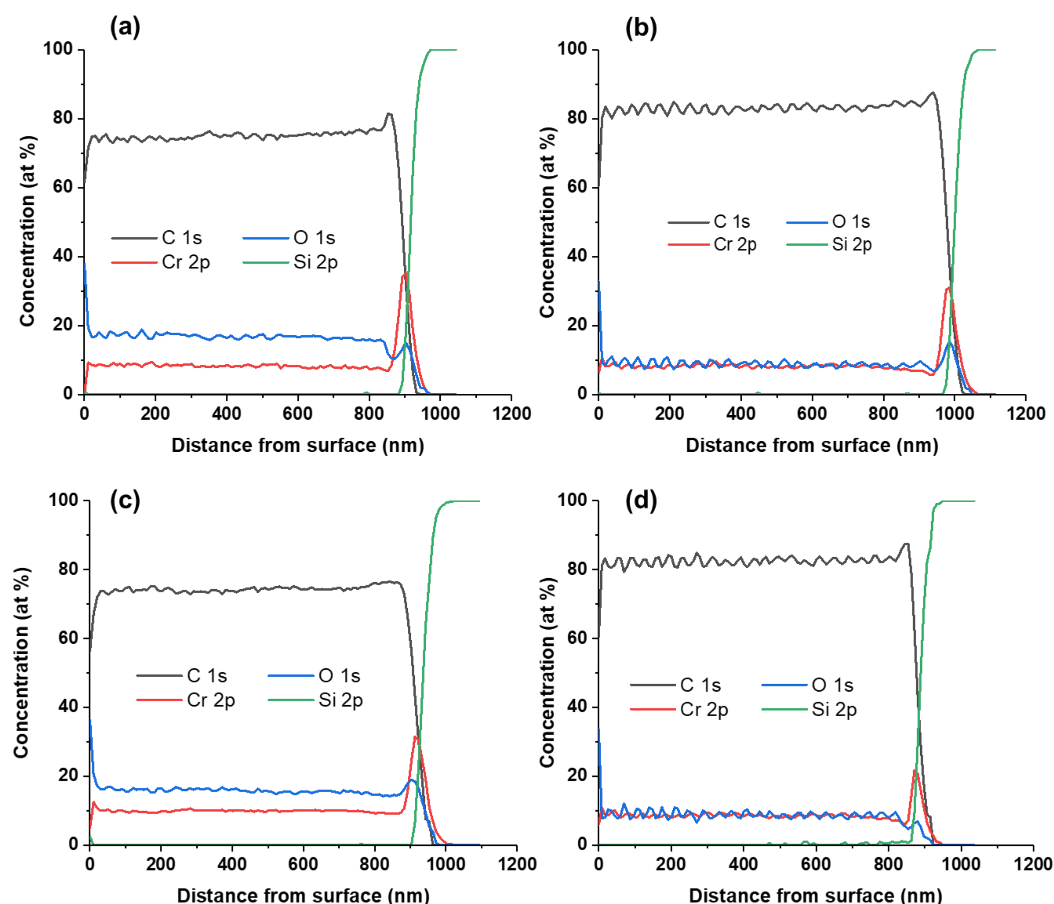

Figure 5-3. Chemical composition obtained by XPS depth profiling as a function of the film thickness for a) 5 mTorr / floating and b) 5 mTorr / -100V, c) 20 mTorr / floating, and d) 20 mTorr / -100V conditions.

The AFM micrographs of the films over the 2x2 μm^2 area of selected regions are given in Figure 5-4. The roughness significantly depends on the applied bias voltage and working pressure [206]. A clear distinction can be made based on the bias voltage: the films obtained without bias exhibit a larger root mean square (RMS) roughness besides exhibiting columns wider than the one produced with -100 V bias. Also, the working pressure seems to affect the roughness when no bias is applied: increasing the working pressure leads to a smoother surface. Hence, the application of a bias during deposition has a

prominent effect on surface morphology. Table 5-1 presents the column diameter and surface roughness measured by AFM.

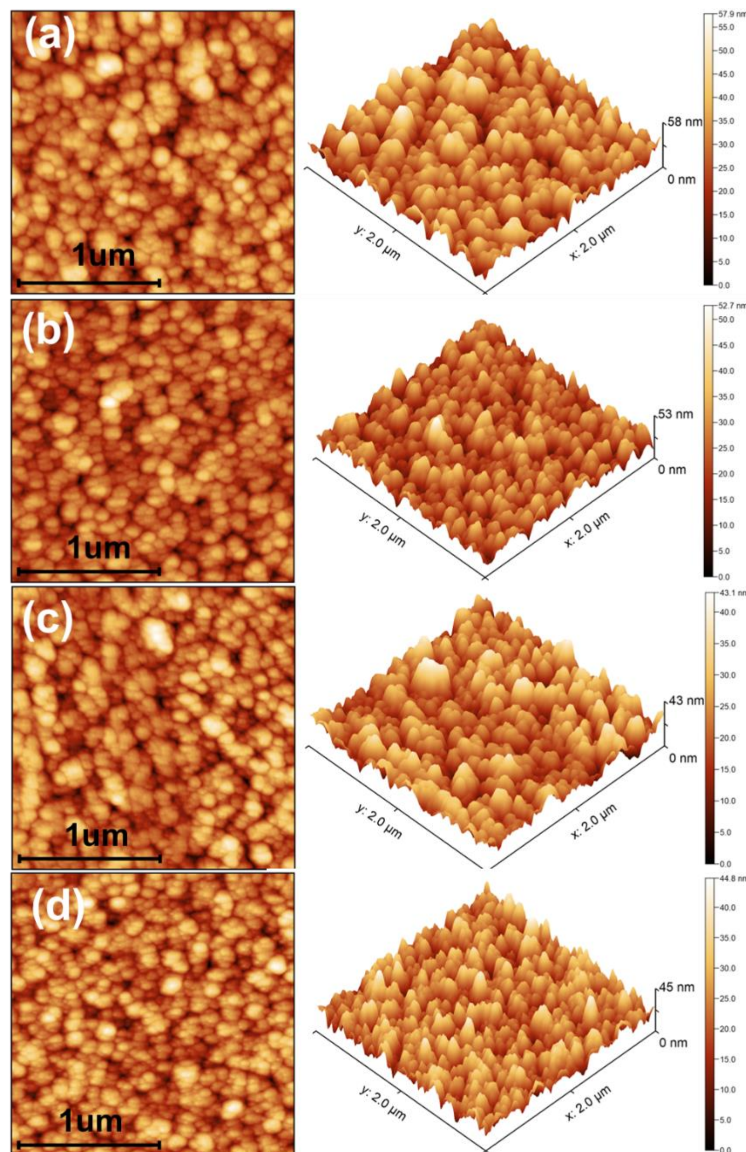

Figure 5-4. AFM images of a-C:H:Cr films a) 5 mTorr / floating, b) 5 mTorr / -100V, c) 20 mTorr / floating, and d) 20 mTorr / -100V.

Table 5-1. a-C:H:Cr films mean column diameter and surface RMS roughness measured by AFM.

sample	Column diameter (nm)	Surface RMS roughness (nm)
5 mTorr / floating	31.5 ± 2.6	7.8 ± 0.16
5 mTorr / -100V	24.7 ± 0.7	6.2 ± 0.01
20 mTorr / floating	31.7 ± 1.6	6.7 ± 0.81
20 mTorr / -100V	29.1 ± 1.6	6.2 ± 0.14

The SEM top view and cross-section micrographs (Figure 5-5) reveal additional microstructure characterization, which varies with pressure and bias voltage. Cross sectional views indicate the presence of a morphological texture with columnar 'growth' parallel to the growth direction as was expected according to the Thornton diagram as we work in Zone 1 with low $\frac{T_s}{T_m} < 0.1\ or\ 0.2$. AFM top view observation and SEM cross sectional view are in qualitative agreement in case of columnar growth of a-C:H:Cr films.

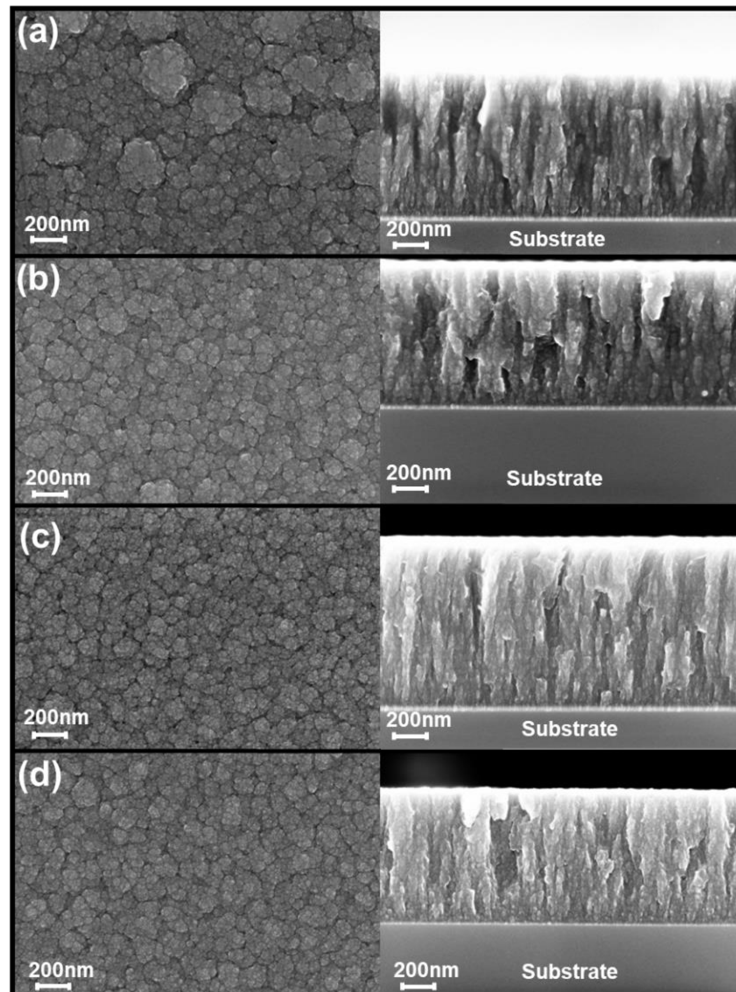

Figure 5-5. SEM micrographs on top views and cross-sections of a-C:H:Cr films: a) 5 mTorr / floating, b) 5 mTorr / -100V, c) 20 mTorr / floating and d) 20 mTorr / -100V.

5.2.2. Mechanical and tribological properties

5.2.2.1. Nano-indentation

The hardness (*H*) and Young's modulus ($E^{'}$) are provided in Table 5-2. Films deposited without applied bias voltage are softer with a hardness of 3.52±0.44 GPa and 3.06±0.37 GPa for 5 mTorr / floating and 20 mTorr / floating, respectively. With an increasing bias voltage, the hardness gradually increases to

reach the highest value (4.95±0.69 GPa) for the 20 mTorr /-100 V sample. Since during deposition, the temperature did not exceed the room temperature (30 °C), no relaxation takes place in the films [207]. For instance, residual compressive stress on the order of 700-800 MPa has been determined using the Stoney method for the 5 mTorr / -100V sample deposited on the Si wafer [10]. The compressive stress experienced in many a-C:H:Cr films tend to close the cracks during indentation preventing crack initiation and propagation while simultaneously showing the smallest indentation imprint. All films illustrate the same trend in Young's modulus.

The performance indices $\sigma_y/_{E'}$ and $\sigma_y^3/_{E'^2}$ extracted from nanoindentation analysis are shown in Figure 5-6 and Table 5-2 as indicating the resistance of wear behavior and plastic deformation of coatings. The yield strength is estimated from the hardness (*H*) as

$$\boldsymbol{\sigma_y = \frac{\xi_3 \, tan(\beta) \, H}{\xi_1 \, tan(\beta) - (1 - \xi_2) \frac{H}{E'}}} \quad , \qquad (6)$$

where ξ_1, ξ_2, ξ_3, and β values for a Berkovich tip are equal to 0.66, 0.216, 0.24, and 19.7, respectively [208].

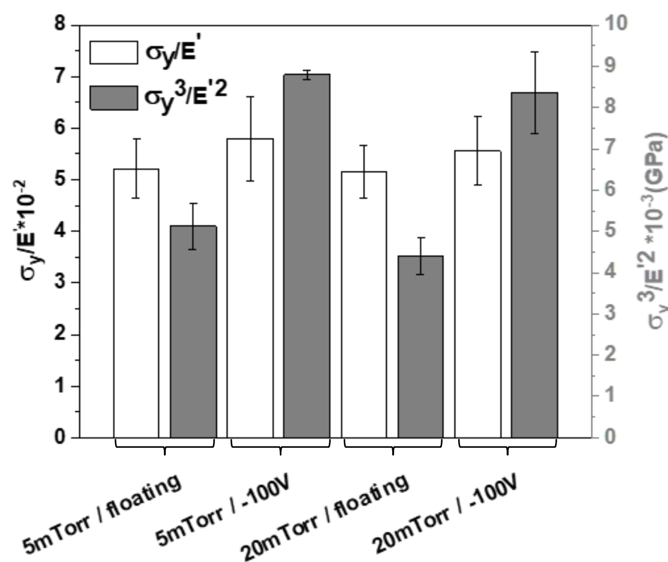

Figure 5-6. Comparison of the performance indices: $\sigma_y/_{E'}$ and $\sigma_y{}^3/_{E'^2}$ for the four conditions investigated in this study. The error bars represent the standard deviation calculated over 16 experiments.

The apparent activation volume V^*can be related to the physical activation volume Ω as $V^* = \Omega\gamma$ where γ is the transformation strain associated with the local atomistic shuffling mechanism [209], which is

the deformation mechanism expected for this class of amorphous solid. The value of γ for amorphous systems ranges from 0.05 to 0.15, see Argon [210]. We assume a transformation strain $\gamma = 0.1$ to obtain a rough estimate of the elementary volume in which the permanent elementary plastic deformation mechanism takes place. Figure 5-7 shows the variation of physical activation volume and the number of atomic sites involved in this volume as a function of the deposition parameters. The physical activation volumes obtained from relaxation tests also illustrate the same trend as for the nanoindentation results. Lower physical activation volume corresponds to films with larger hardness.

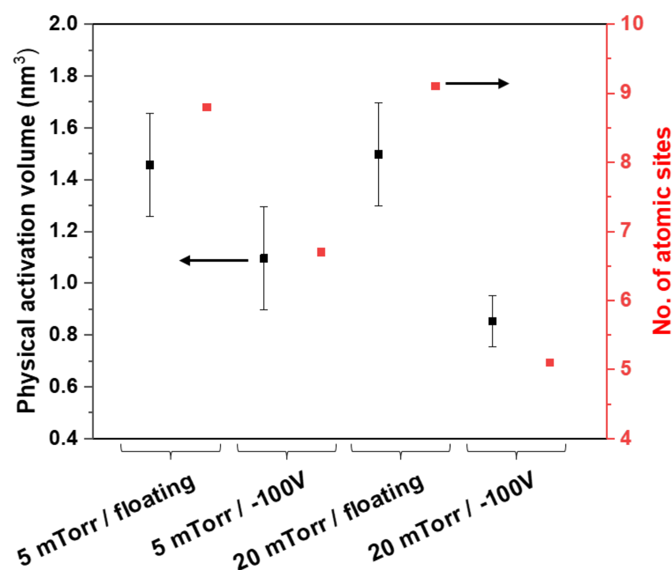

Figure 5-7. Effect of the deposition parameters on the physical activation volume and associated number of atomic sites of a-C:H:Cr thin film.

The lowest physical activation volume is found for the 20 mTorr / -100 V thin film as equal to $\Omega = 0.85 \pm 0.11\ nm^3$. When no bias is applied, the working pressure does not significantly affect the physical activation volume which is around 1.5 ± 0.23 nm^3.

5.2.2.2. Wear behavior

The wear behavior of the films has been directly evaluated by measuring the critical load at the onset of cracking (L_c) as shown in Figure 5-8.a. L_c is defined as the load at which the coating fails under scratching conditions. Elastic recovery is also displayed as a function of sliding distance in Figure 5-8.b. Total elastic recovery corresponds to 1 and fully plastic deformation corresponds to 0. 5 mTorr / -100 V condition remains nearly fully elastic until it fails. The variation of L_c for each material is displayed in Figure 5-8.c. The bias voltage plays a major role in the enhancement of the coating resistance to wear. Also, the deposition working pressure seems to be significant, with the 5 mTorr / -100 V sample being clearly more resistant to the onset of wear compared to the 20 mTorr / -100V one. The coefficient

of friction is also an important index of the performance of an industrial coating (see Figure 5-8.d). It must remain low even under high load.

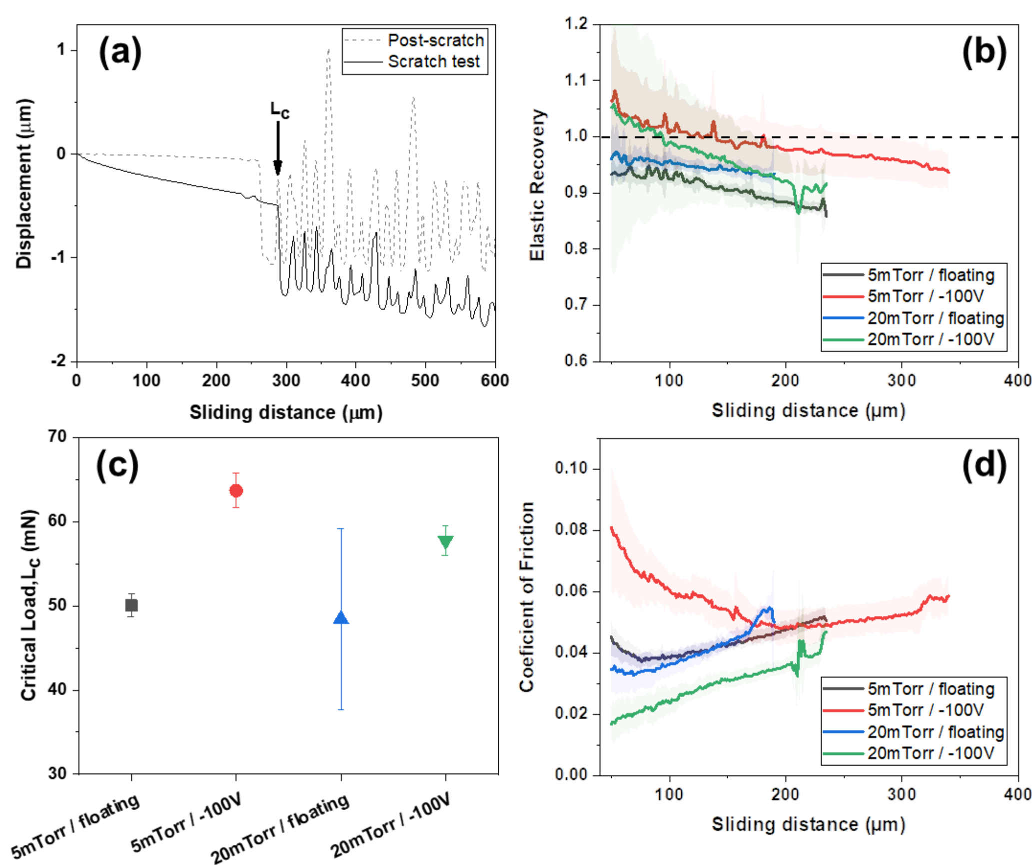

Figure 5-8. Results from the nanoscratch tests: (a) typical scratch profile with the displacement during loading as a black plain line and the profile of the wear track after loading in a dashed black line. The black arrow indicates the location of the critical load; (b) variation of the elastic recovery as a function of the sliding distance; (c) average critical load measured for each coating, error bars indicate the standard deviation; (d) variation of the coefficient of friction as a function of the sliding distance.

The critical load for the onset of chipping increases by applying a bias voltage, see Figure 5-8 and Table 5-2. Whatever the working pressure, applying a bias voltage leads to an increase in the wear resistance of the a-C:H:Cr films. Figure 5-9 displays typical wear tracks produced by micro-scratching. Several features distinguish the materials failure modes: (i) the first chip forms at a critical load noted L_c propagates both forward and backward; (ii) the chip formation mechanism varies from random to reproducible chip sizes and shapes; (iii) a step-like pattern is evidenced along the crack surface. For 20 mTorr films, the first chip propagates at a significantly lower critical load compared to 5 mTorr coatings. This would imply that delamination at the interface between Si wafer and a-C:H:Cr film begins earlier – at a lower load – for the 20 mTorr samples. The shape and the size of the chips depend on the bias voltage applied during deposition. Indeed, without bias, the chips are relatively diverse while

for biased samples (-100 V), the chips are very reproducible. Also, for biased samples, chips are smaller and crack propagation is limited [211]. Finally, the fracture surface of the chip presents a step-like pattern as highlighted in Figure 5-9.f. A qualitative counting of these features gives 20 occurrences. This is in line with the number of rotations performed during deposition (~23) where the samples being either close to the acetylene plasma or away. By getting far from the target, the risk of oxidation increases due to the absence of energetic ions bombarding the surface along the outermost surface of the film, which produces a weaker interface for the next layers.

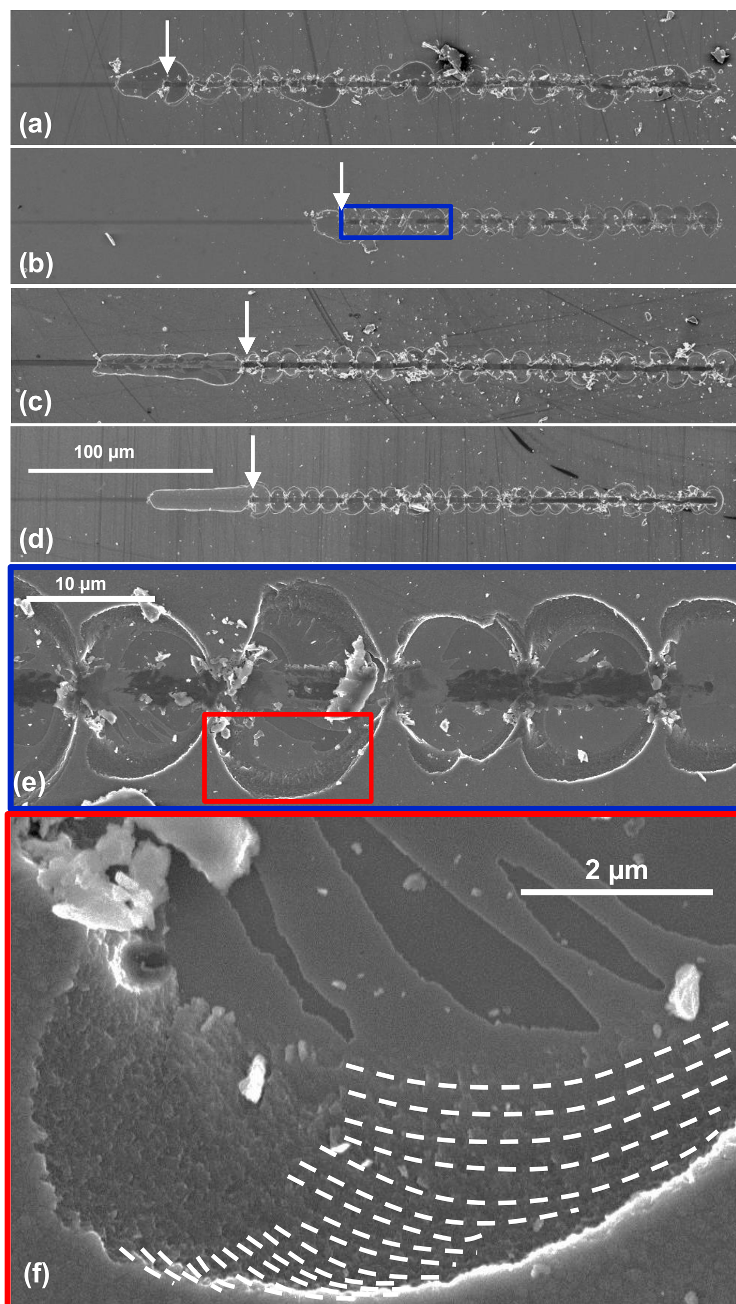

Figure 5-9. Typical wear track after nano-scratch testing of (a) 5 mTorr / floating, (b) 5 mTorr / -100 V, (c) 20 mTorr / floating, (d) 20 mTorr / -100 V. The white arrows indicate the location of the critical

load. The blue box highlights in (e) the formation of a chip just after the critical load on a 5 mTorr / -100 V sample. The red box displays in (f) the crack features of the chip. The dashed white lines highlight the step-like pattern produced during the formation of the chip.

Table 5-2. Nano-indentation and micro-scratch related results: hardness, Young's modulus, resistance to plastic deformation, wear resistance, and critical load values for different deposition conditions.

	$\boldsymbol{H}$ (GPa)	$\boldsymbol{E'}$ (GPa)	$\frac{\boldsymbol{\sigma_y}}{\boldsymbol{E'}} * \mathbf{10^{-2}}$	$\frac{\boldsymbol{\sigma_y}^3}{\boldsymbol{E'^2}} * \mathbf{10^{-3}}$ (GPa)	$\boldsymbol{L_c}$ (mN)
5 mTorr / floating	3.5 ± 0.4	36.2 ± 2.8	5.21 ± 0.57	5.12 ± 0.56	50 ± 1.3
5 mTorr / -100V	4.7 ± 0.8	45.1 ± 4.3	5.80 ± 0.81	8.80 ± 0.12	63.7 ± 2.0
20 mTorr / floating	3.1 ± 0.4	32.3 ± 1.9	5.15 ± 0.51	4.40 ± 0.43	48.4 ± 10.7
20 mTorr / -100V	4.9 ± 0.7	48.7 ± 3.9	5.60 ± 0.65	8.37 ± 0.99	57.7 ± 1.2

5.2.2.3. Uniaxial tensile tests

5.2.2.3.1. In-situ SEM tensile tests

In order to determine the saturation crack density (ρ_{sc}), 200x magnification SEM micrographs have been selected – i.e. with a typical 580 µm linear field of view to ensure statistically relevant measurements. Figure 5-10.(a-d) shows crack patterns at 1mm of crosshead displacement (at 1000x magnification in order to distinguish the cracks clearly) when saturation is reached (in detailed information is available in annex chapter). An elastic deformation is observed up to ~1.5% strain followed by a crack initiation. Increasing the bias voltage and decreasing the pressure leads to lower crack density and earlier saturation of the cracking process, see Table 5-3. Figure 5-10.e shows a typical crack at very high magnification in a 20 mTorr / -100 V thin film. The cracks systematically propagate along the cluster boundary.

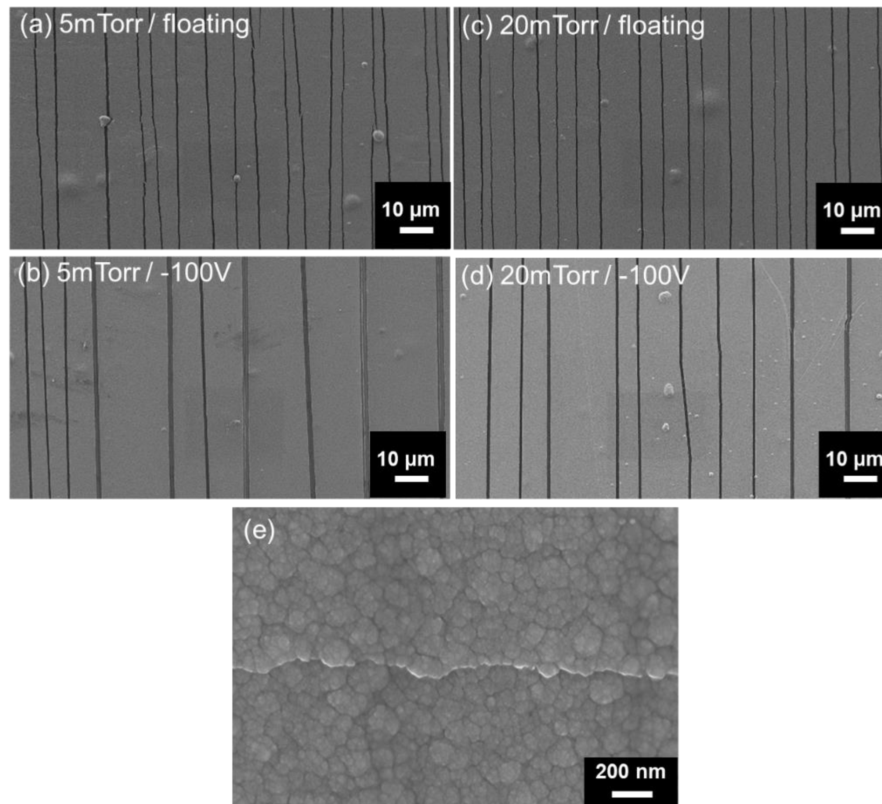

Figure 5-10. (a-d) Evolution of crack density with in-situ strain for different samples (e) typical high magnification SEM top-view observation of a crack.

The fracture toughness of the films has been determined using equation (4) with a Z factor equal to 15.6, as computed by [177] for a ratio $H/_h$ around 30 and a α-Dundurs parameter equal to 0.9. The plane strain Young's modulus is obtained from nanoindentation experiments. The strain has been determined from in-situ optical microscopy tensile tests by taking the strain at which the first cracks start to propagate. K_{Ic} values of the different film conditions are presented in Table 5-3 as well as the corresponding G_{Ic}. Increasing the working pressure leads to higher fracture toughness, as well as applying a bias voltage. Also, the application of a bias voltage decreases the crack density at saturation G_{Ic} values above 100 J/m^2 which is an excellent resistance to cracking for a 1µm thick film [8].

Table 5-3. Traction related results: Fracture strain and stress, Saturation crack density at 1mm of crosshead displacement, critical fracture energy release rate, fracture toughness, and fracture plastic zone size values for different deposition conditions.

	Fracture strain (%)	Fracture stress (MPa)	ρ_{sc} (µm^{-1})	G_{Ic} (J/m^2)	K_{Ic} (MPa.m$^{1/2}$)	d *(nm)*
5 mTorr / floating	0.3	108.6	0.128 ± 0.004	4.94 ± 0.04	0.42 ± 0.08	15.7 ± 0.82
5 mTorr / -100V	0.83	374.33	0.049 ± 0.001	47.4 ± 0.83	1.46 ± 0.05	100.8 ± 1.08
20 mTorr / floating	1.5	484.5	0.173 ± 0.002	125 ± 5.63	2.01 ± 0.18	488.6 ± 2.68
20 mTorr / -100V	1.3	633.1	0.1 ± 0.003	115 ± 2.95	2.37 ± 0.12	242.5 ± 1.55

5.3. Discussion

5.3.1. Effect of process parameters on hardness, Young's modulus, and activation volume

The magnitude of the hardness and Young's modulus are in good agreement with similar a-C:H coatings from the literature. For instance, Wei *et al.* [96] measured hardness between 3 - 6 GPa, Kassavetis *et al.*[212] between 2 - 6 GPa, Vanden Brande *et al.*[213] around 4 GPa, and De vriendt *et al.*[214] around 7 GPa. Also, in these studies, the Young's modulus varies between 22.7-49.2 GPa, 20-45 GPa, 25-30 GPa, and 70 GPa, respectively.

By increasing the deposition pressure, ions are more likely to react with acetylene or to recombine with low energy electrons. This leads to a reduction of the calculated ion mean free path from ≈22 mm to ≈5 mm and a rise in the number of collisions from $1.8e^4$ collision/s at 5 mTorr up to $7.2e^4$ collision/s at 20 mTorr. By knowing the target to substrate distance (≈150 mm) one can assume that number of collisions will increase from $1.2e^5$ to $2.1e^6$ $collision/s$ from 5 mTorr to 20 mTorr, so it will decrease the energy of incident ions much more by increasing the deposition pressure. These reactions and recombination reduce the amount of energetic $C_2H_2^+$ and Ar^+ reaching the substrate. As a result of the sub-plantation process being reduced, energetic ion penetration into the growing film will be prevented, which will lead to less sp^3 bonding, which is a crucial characteristic of hard films [199,200,215]. Consequently, film growth results from the condensation of low energetic species. In this case, growth will mostly cause by the condensation of $C_{2n}H_3$ molecules which leads to a decrease in the hardness value [199,200,215]. Amorphous carbon films deposited from C_aH_b base without applied bias voltage are known to contain a higher density of C-H bonds which involve much smaller displacement energy than C-C bonds as present in a-C:H coatings [186,200], and films will contain a high amount of free volumes

in their structure. When the bias voltage is applied, an increase in the energy of the ions impinging the substrate causes electron and carbon atoms to yield to compensate for free volume deficiency. This has been confirmed by the Raman spectroscopy results presented in Figure 5-2.b and hardness values where the I_D/I_G decreases with increasing sp^3 content at lower pressure and biased films. Although analyzing the I_D/I_G for a-C:H:Cr does not precisely reflect the hardness variation since the specimens are made up of two different elements rather than only carbon, the results may typically be used to identify patterns based on carbon structure. The increase in the film hardness is associated with the decline in I_D/I_G [193].

There is also a link between the applied bias voltage and the physical activation volume. Lower activation volumes are found when a bias voltage is applied during deposition, this would be another evidence of higher packing density [216]. Furthermore, assuming that the interatomic spacing of the surrounding C atoms is similar to the one of graphite, i.e. 3.4 Å [217,218], and that these sites present a spherical shape, we can estimate the volume of each site to be ∼0.16 nm^3. These characteristics relate to crystalline C and do not represent the free volume of the amorphous structure of a-C:H:Cr. Nonetheless, the physical activation volume obtained from the nanoindentation test corresponds to 5 to 9 crystalline C atom sites. This suggests that the elementary volume where plastic deformation events occur is very localized and includes the motion of a few C atoms only. The lower the physical activation volume, the less the atoms will be involved in the viscoplastic deformation mechanisms which is favorable in terms of the mechanical stability of the coatings owing to higher strain rate sensitivity. Since the physical activation volume has the lowest value for biased samples, a stronger atomic arrangement of carbon clusters is expected as can also be seen from the elastic properties. The present results confirm that the effect of the bias voltage is predominant over the effect of deposition pressure.

5.3.2. Effect of process parameters on wear resistance

The critical load L_c at which scratch damages start appearing on the coating is used to qualify the wear resistance with a similar tip. Besides the coating/substrate adhesion, the detachment of the fragments is also related to the cohesive (within the coating) fraction. The critical load has been shown to be proportional to the ratio ${\sigma_y}/{E'}$ quantifying the ability to deform elastically [219], which is in good agreement with what is observed here when applying a bias voltage (see Table 5-2). Again, applying a bias voltage results in enhanced scratch resistance. This is a known result, but this scenario is also in good agreement with the activation volume values. Note that even though the activation volume for 20 mTorr / -100V is lower than 5 mTorr / -100 V, the critical load of the film deposited under 5 mTorr / -100 V is a bit higher. This can be explained by the weak interface adhesion between the Si substrate and the 20 mTorr sample as compared to the adhesion of the 5 mTorr film. The key information

extracted here is that a lower activation volume and higher $\sigma_y/_{E'}$ and $\sigma_y^3/_{E'^2}$ leads to a longer elastic track on the coating, delays the plastic deformation and increases the critical load to the onset of crack.

Table 5-4 compares our results with other studies using the same deposition technique in the literature. Results are in good agreement with coatings made of comparable a-C:H:Me materials found in the literature. The choice of the target has an importance. Additionally, our results based on a metallic target and C_2H_2 precursor gas show a higher critical load than one obtained for films deposited from sputtering a graphite target.

Table 5-4. a-C:H:Cr films deposited by PECVD method with CH_4 and C_2H_2 precursor gases or graphite target and nano-indentation results in comparison with recent work.

Sample	Precursor gas/source	$\boldsymbol{H}/_{\boldsymbol{E'}}$	L_c (mN)
Ref [23]	CH_4	0.124-0.134	33-64
Ref [220]	CH_4	0.11-0.16	43-120
Ref [221]	CH_4	-	18.2-23.5
Ref [222]	C_2H_2	0.041-0.086	36-75
Ref [223]	C_2H_2	0.081	68
Ref [224]	C_2H_2	0.067	2.13
Ref [225]	Graphite	0.14	6
Ref [226]	Graphite	≈0.083	1.9-5
Ref [227]	Graphite	≈0.081	40
Our study	C_2H_2	0.09-0.1	48-64

5.3.3. Effect of process parameters on fracture behavior

The SEM micrograph of Figure 5-10.e, shows that the preferential crack path follows the boundary of columns. This highlights weaker inter-column boundaries. This is comparable to nano-glasses with weaker grain boundaries in comparison with the glassy matrix because of the higher free volume density contained in the boundaries [65,228,229]. However, the cluster interface strength also depends on the applied biased voltage. A decrease in columns' size is found in samples with bias voltage, thus for the smaller clusters – i.e. higher ratio of the interface to cluster – the crack resistance is the highest. If the interface strength is constant, a lower number of interfaces will lead to an enhanced crack resistance, whatever the applied bias. Indeed, increasing the bias voltage leads to an increase in the adatom energy. Thus, atoms will attach more firmly to the substrate and already present clusters. It is therefore confirmed that the cluster interface is stronger when a bias is applied, providing enhanced crack resistance [230].

Finally, the $\sigma_y/_{E'}$ a performance indicator is plotted against the fracture energy (G_{Ic}) to compare the four different a-C:H:Cr coatings to an extensive list of thin film materials gathered from the literature [114,127,148–162] in Figure 5-11. As an indicator of cracking resistance, the a-C:H:Cr coatings present the largest yield strength over Young's modulus ratio with tunable G_{Ic} in range of 5 - 125 J/m^2.

Higher G_{Ic} and K_{Ic} values for 20 mTorr samples can be directly related to their larger fracture strain and plastic process zone size which is more than 2 times larger than in 5 mTorr films. Thus, by increasing the plastic process zone size, due to enhanced crack tip plasticity, the crack tip will be more blunted, and more energy will be needed to grow damage in the fracture process zone before material separation [231].

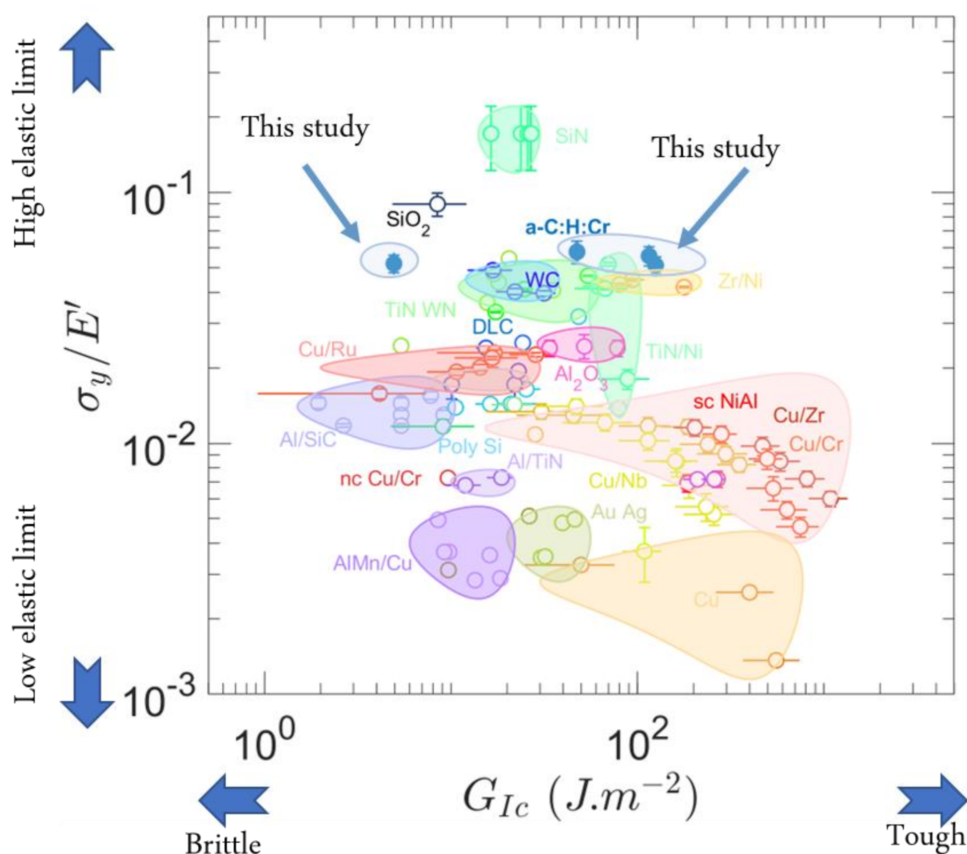

Figure 5-11. Materials property map presenting the ratio yield strength over Young's modulus against critical energy release rate. The results are obtained from the literature and compared to the four a-C:H:Cr thin films produced in this study [114,127,148–162].

Accordingly, a-C:H:Cr coatings maintain a hardness that is substantially higher than that of elastomers while withstanding significant elastic deformation without showing signs of plasticity or failure. Also,

the deposition conditions influence the film toughness, and a relatively high critical energy release rate can be reached. This is of particular interest for applications where no residual scratches or imprints must remain after the contact. Protecting magnetic storage media from wear and corrosion due to their superior scratch resistance, bearings, gears, seals, engine components, oil media, and operation under ultra-high vacuum conditions are just a few of these applications [109–111]. Thus, according to the discussed properties, coatings with lower deposition pressure are attractive in applications where better adhesion and higher scratch resistance are needed. On the other hand, coatings with higher deposition pressure are beneficial for applications under extreme tension since they will exhibit larger fracture strain and fracture toughness.

5.4. Conclusions

The coating community often works to improve coating performances with different techniques using a trial-and-error approach. To the best of our knowledge, no rational material selection technique has been used yet to guide the optimization of a-C:H:Cr films based on targeted performance indices. In this work, we report a first effort in this direction to select the PECVD conditions in view of expected performances.

To this end, we evaluated the mechanical properties of four selected films deposited under different conditions (5 mTorr, 20 mTorr sputtering pressure, floating or -100V bias voltage). Application of bias voltage was found dominant in terms of increasing the resistance to plastic deformation and wear resistance. Higher deposition pressure (20 mTorr) showed excellent resistance to cracking under tension, whatever the bias voltage.

The coating demonstrated a higher elastic limit (approximately 5%) compared to a similar class of coatings in the industry. Additionally, it exhibited tunable fracture energy, which can be categorized into three distinct regimes: low (<10 J/m^2), mid (10-100 J/m^2), and high (>100 J/m^2) levels.

Finally, this study proves that instead of focusing on specific parameters, it will be more beneficial to mix and match the mechanical properties in order to meet different lists of requirements associated with different types of applications.

Chapter 6.

6. Vein pattern vs. columnar fracture shape in Cu-Zr thin film metallic glasses: Driving force and mechanism

This chapter sheds light on the main driving force and mechanism of different fracture shapes in amorphous thin films.

Abstract

Numerous studies have been published in the past showing the presence of vein-like or columnar fracture shapes in thin film metallic glasses (TFMGs), while the reason behind the different features remains poorly understood. This study uncovers the reason behind this phenomenon in Cu-Zr TFMGs' by considering experimental evidence and analysis. Oxidation during deposition is the reason for the presence of the columnar feature after the cleavage, as shear banding cannot raise the temperature enough for the regional melting process to end up in the vein pattern. In several studies, unnoticed or unreported oxygen is proposed to be the reason for reporting metallic glasses' columnar cross-sections.

Keywords: Cu-Zr metallic glass, vein pattern, shear band.

This chapter has been published as a scientific paper in the journal of Materialia:

***Bagherpour A**, Haye E, Moskovkin P, Lucas S. Vein pattern vs. columnar fracture shape in Cu-Zr thin film metallic glasses: Driving force and mechanism. Materialia. 2023 Dec 1;32:101914.*

6.1. Main Text

Shear bands, localized regions of intense shearing strain, are common in various materials but are particularly prominent in metallic glasses due to their work-softening behavior below the glass transition temperature (Tg) [232,233]. The occurrence of shear bands limits the structural potential of metallic glasses as they lead to plastic instability and catastrophic failure under tension [234–236]. During shear banding, the stored elastic energy converts into kinetic energy within the bands, resulting in a temperature rise. The fracture of metallic glasses (MGs) exhibits distinct features such as spark formation, liquid droplets, and river-like patterns, indicating a significant temperature increase (thousands of degrees) during fracture [237–240]. Among the MGs, Cu-Zr based TFMGs caught much interest, especially due to their high Glass Forming Ability (GFA), ease of production, superior mechanical properties, high biocompatibility, and low manufacturing cost [241–243].

When metallic coatings are deposited by Physical Vapor Deposition (PVD), they usually exhibit columnar cross-section on cleaved silicon substrates when observed by Scanning Electron Microscopy (SEM). Nevertheless, in the cases of cross-sectional observation of Cu-Zr TFMGs, possible vein patterns together with columnar features are observed and are not well understood (see Figure 6-1).

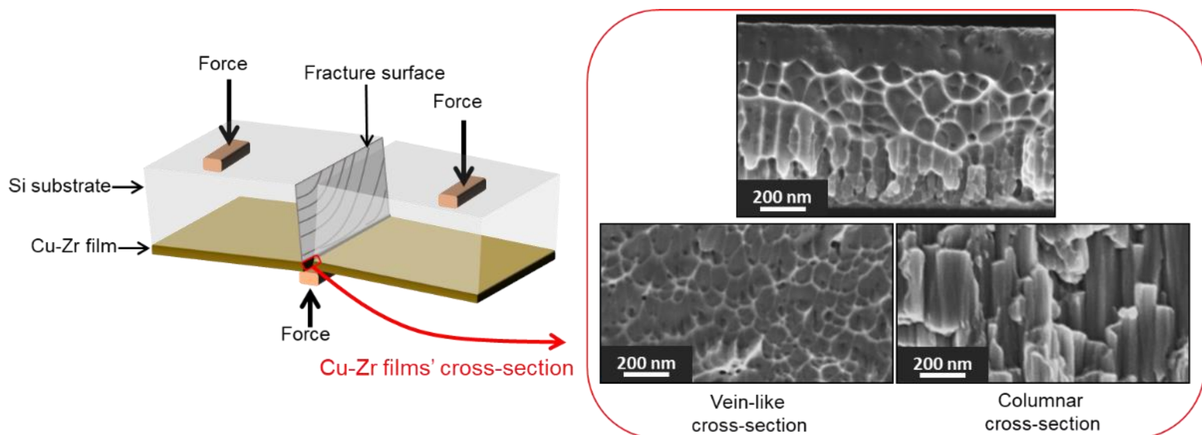

Figure 6-1. Schematic representation of the crack propagation configuration for Cu-Zr TFMGs deposited on the Si wafer with two different patterns observed by SEM. The loading configuration resembles a three-point bending test.

According to our knowledge, no dedicated studies have been taken to understand the cause or the initial driving force for the appearance of the venous and columnar patterns after the film fracture in the same sample. Therefore, we hypothesize that vein patterns form during the breaking of the pure metallic glass sample, regardless of the initial growth shape. Using DC-magnetron sputtering in a semi-industrial chamber (D&M Vacuum system), films were deposited on silicon (100) wafers with a base pressure of 10^{-6} Torr prior to the deposition. PVD machine was equipped with a pure metallic Cu target (7.5x35cm,

purity 99.95 %, Neyco) and Zr target (7.5x35cm, purity 99.4 %, Nova fabrica). Cu-Zr films have been sputtered (after 10 min of target cleaning with 400-800 W power) under different deposition conditions (150 sccm Ar, 5 mTorr, 20 mTorr sputtering pressure, floating or -100V bias voltage). Another set of samples has been sputtered in Ar and oxygen atmosphere (150 sccm Ar / 3, 5, 7 sccm O_2) under 5 mTorr / -100 V bias condition to simulate the pure metal oxidation condition. The gas flow rate was controlled by FloTron multi-channel reactive gas monitoring system. To ensure uniform coating, 2-fold sample rotation around the Z axis and 2 rpm table rotation speed were employed. Fracture analysis was performed by cracking Si wafers using cleaving pliers from a shallow notch induced by a diamond tip on the back face. The crack finally propagated into the Cu-Zr film.

Figure 6-2 shows the SEM (ZEISS Ultra 55) cross-section of two independent samples deposited in different conditions (a&c; 5 mTorr, Cu_{power} = 400W, Zr_{power} = 600W and b&d; 5 mTorr, Cu_{power} = 210-470W, Zr_{power} = 1000W). More detail about characterization (especially XPS depth profiling) is given in the supporting information.

Very interestingly, venous and columnar fracture shapes were observed for these two samples in the cross-section imaging even though deposition conditions were different, and these observations could be reproduced numerous times.

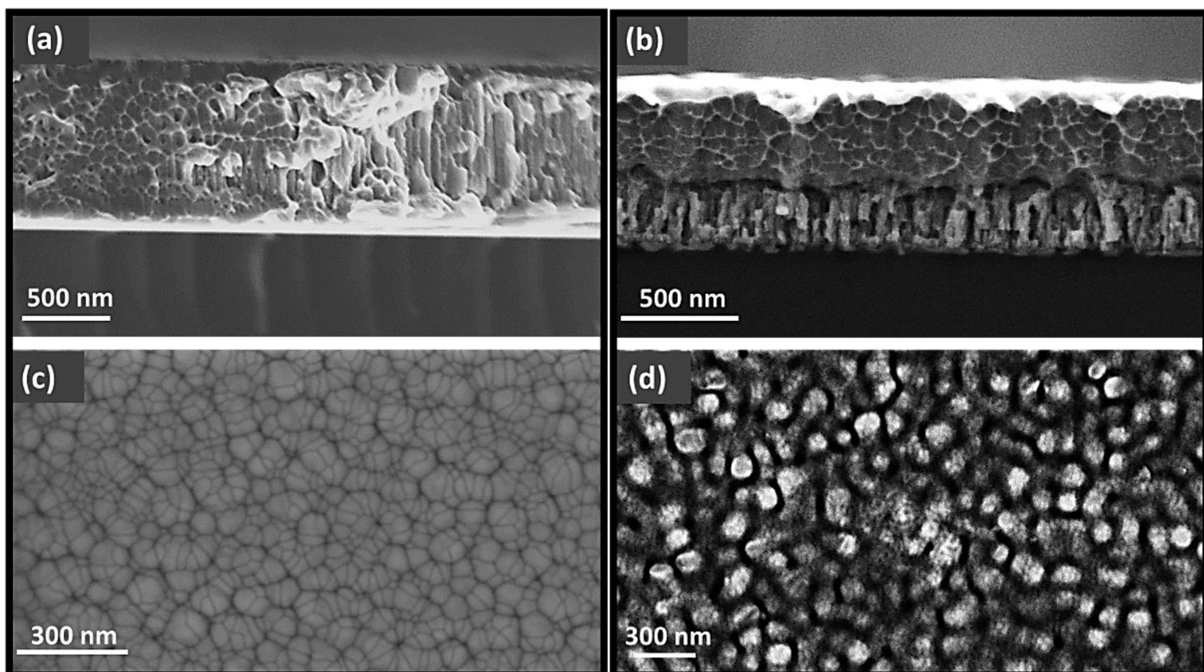

Figure 6-2. (a,b) cross-sectional SEM micrograph of the columnar and vein-like patterns simultaneously in two samples deposited in different conditions with the (c,d) same initial columnar growth evident on the top-view.

The vein patterns run from the top to a given depth of the samples through the whole thickness after the fracture. Also, top-view observation reveals typical metallic film growth with columnar morphology. The cross-section morphology of the films also reveals cases for which columnar growth is observed at the vicinity of the sample surface, for later being in a vein pattern morphology across the remaining film thickness. No process interruption takes place during the deposition, and this vein/column mixture exhibits well-separated and identified interfaces that seem to result from a rapid, instantaneous phenomenon that cannot be related to the deposition process. Indeed, the approximate value of the released elastic energy during the cleavage was calculated as $1.18 \times 10^{20}\ eV.cm^{-3}$ using the equation (1) [244]

$$\Delta U_c = {\sigma_y^2}/{2E}\ , \tag{1}$$

Where ΔU_c is the released elastic energy per unit volume, σ_y the yield strength, and E is the Youngs' modulus of the film. with σ_y and E for the 5 mTorr/-100V sample equal to 2.04 ± 0.09 GPa and 110 ± 4.7 GPa, respectively. It is noteworthy that calculations have also been done for the rest of the samples, and the released elastic energy values are in the same range between $1.18 \times 10^{20}\ to\ 1.3 \times 10^{20}\ \ eV.cm^{-3}$.

We can compare this value to the amount of energy deposited by condensing atoms. Each deposited atom has an energy of ~ 10 eV [245–247]. Due to the thermal conductivity [248], the energy is quickly spread to a volume determined by the film's thermal diffusivity. One can estimate the volume where the energy is spread as follows

$$l = \sqrt{6kt}\,, \tag{2}$$

$$V = {4}/{3}\,\pi l^3\ . \tag{3}$$

Then, the energy deposited by condensing atoms is $U_a = \frac{10\ \text{eV}}{V}$, where l is the diffusivity length, $k = {\varkappa}/{C_p}$ is thermal diffusivity, $\varkappa$ is thermal conductivity, C_p is volumetric heat capacity ($\sim 3\,J/K.cm^3$ here), and t is characteristic time ($10t_{vibration}$, with $t_{vibration} = 10^{-12}s$). U_a calculated between $10^{15} - 10^{19}\ eV.cm^{-3}$ depending on the thermal conductivity of the film.

This is evidence of the inability to reach the same temperature as cleaving to create a vein pattern by melting the underlayers during deposition. Also, it is worth mentioning that energy brought by depositing atoms is deposited only in the first top layer of the film, and thus, it cannot modify the columnar structure of the film in depth under the surface.

Breaking samples initiates cracks and crack propagation due to stress concentration and the release of stored elastic energy in the sample. Since shear bands are highly localized regions of intense deformation, massive energy dissipation of shear propagation can lead to a temperature increase, causing a viscosity drop and shear softening phenomenon due to internal friction and deformation processes within the material, as approved in previous studies. Since this process is so fast and happens in a few hundred nanoseconds, the temperature rises above T_g, leading to regional softening, melting, and fast solidification due to the thermal gradient of the sample and environment [237,249,250].

However, the melting/solidification process only occurs if the local material has a melting point below the temperature reached during the breaking and shear propagation process. It is known that the melting point is first influenced by the composition [251] and the oxygen content [252] but also in a complicated manner by residual stress [253]. For example, pure copper and zirconium have melting points of $1084^{\circ C}$ and $1855^{\circ C}$, respectively, while their oxides have a much higher melting point [254]. Therefore, both patterns can be observed if the oxygen composition evolves through coating thickness.

Consequently, with our hypothesis, the high-temperature melting region, like the one containing oxygen, should not undergo a morphology change during sample cleavage, while the one with low melting temperature, i.e., almost pure metallic, should.

Figure 6-3, with the XPS analysis (ThermoFisher K-alpha spectrometer), shows a gradient of oxygen at the beginning of the deposition in the cross-section, going from 40 at% down to zero, which fits the evolution of the morphology perfectly. The corresponding explanation of depth profiling is explained in more detail in [255,256]. The region where oxygen is incorporated during the film growth does not undergo a transformation from a columnar to a vein-like morphology.

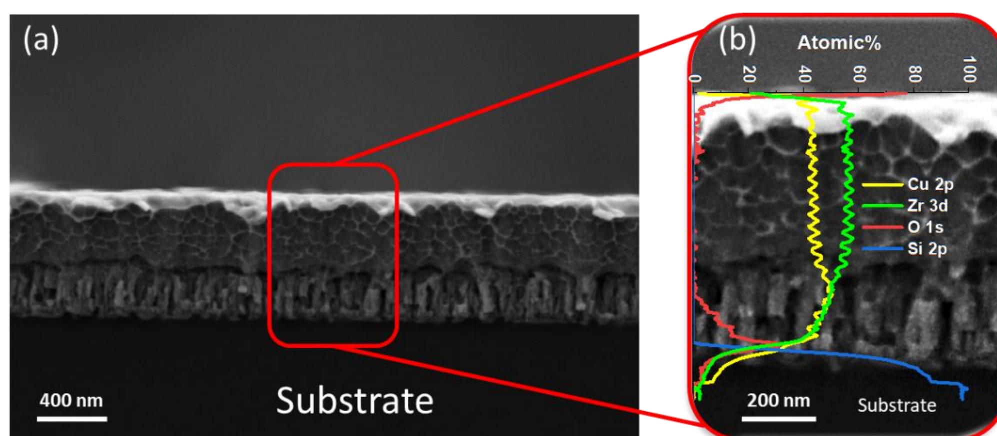

Figure 6-3. a) SEM micrograph of columnar / vein pattern, and b) XPS graph integrated with SEM cross-section as proof of oxygen influence on fracture shape.

To further validate or invalidate this hypothesis, experiments were designed to vary the oxygen integration in the films during the deposition. There are different ways to do that: if one has an ultra-high vacuum deposition system with a very low amount of oxygen impurities and not contaminated sidewalls, a good control injection of oxygen during film growth is the way to go. Unfortunately, in an industrial system like the one used for this study, the oxygen content in the gas phase during deposition can be such that there is a tiny amount of oxygen incorporated into the films during the growth because of the outgassing of the walls of the coater even though the base pressure is 1×10^{-6} Torr. This is certainly the case for the coatings incorporating highly reactive Zr. It is further known in the field that biasing the substrate reduces the amount of oxygen content in the film compared to a floating mode. Another explanation is that the target was heavily oxidized, and the target cleaning was insufficient, leading to oxygen incorporation into the coating.

The effect of such an experimental design is summarized in Figure 6-4 for samples deposited at 5 mTorr and 20 mTorr sputtering pressure, floating or -100V bias voltage.

If one looks at the oxygen content as measured versus depth by XPS, one can observe that the content is modulated as expected in between samples because the ones deposited with a bias of –100 V (Figure 4.c & e) do not contain oxygen across the film thickness for low and high pressure. On the contrary, the ones deposited in floating conditions contain about 10 % for both (Figure 4.b & d).

All samples are amorphous, as shown by the XRD (PANalytical X'Pert PRO) graphs (Figure 6-4.a). However, the cross-sections exhibit different morphological patterns: the ones with no oxygen detected are vein-like, while the two others are columnar-like, confirming our hypothesis that the vein-like structure is only observed in the sample with low temperature-melting zone after cleavage.

To further confirm that hypothesis and validate that the observations are not related to a difference in density or special film growth mode during the process induced by substrate biasing, another set of experiments was performed with a bias of –100 V, a collateral benefit being that the oxygen content in the film is below the XPS detection limit. Then a small flow of oxygen (3, 5, and 7 sccm) can be injected during the deposition process to determine an oxygen concentration threshold for which the transition venous/columnar morphology during the sample cleavage is affected, as shown in Figure 6-5.

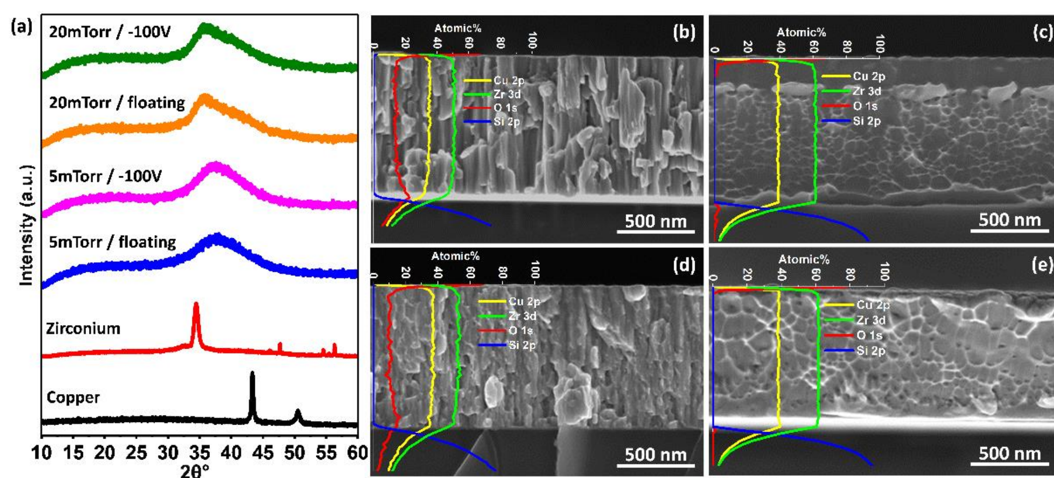

Figure 6-4. (a) XRD analysis of amorphous Cu-Zr TFMGs and SEM topography of b) 5 mTorr/floating, c) 5 mTorr/-100V, d) 20 mTorr/floating, e) 20 mTorr/-100V with XPS analysis inset to the figs.

As can be seen from SEM images (see Figure 6-5 b-e), in the sample with no oxygen nor contamination (pure metallic glass, Figure 5.b), a vein pattern is still observed in the fracture cross-section. However, for any oxygen flowrate larger than 3 sccm (Figure 6-5.c-e), a columnar morphology is observed in the films even for oxygen content in the film as low as 3-4 at. % (Figure 6-5.c), while again, all the films are amorphous (Figure 6-5.a). The formation of a dual peak in the XRD pattern of the sample with the highest oxygen content indicates a marked local order but with extended average bond lengths. The high oxygen percentage can induce changes in covalent bond behavior, local ordering, and geometrical distortion [65,257,258], before (in terms of oxygen content), the oxide formation.

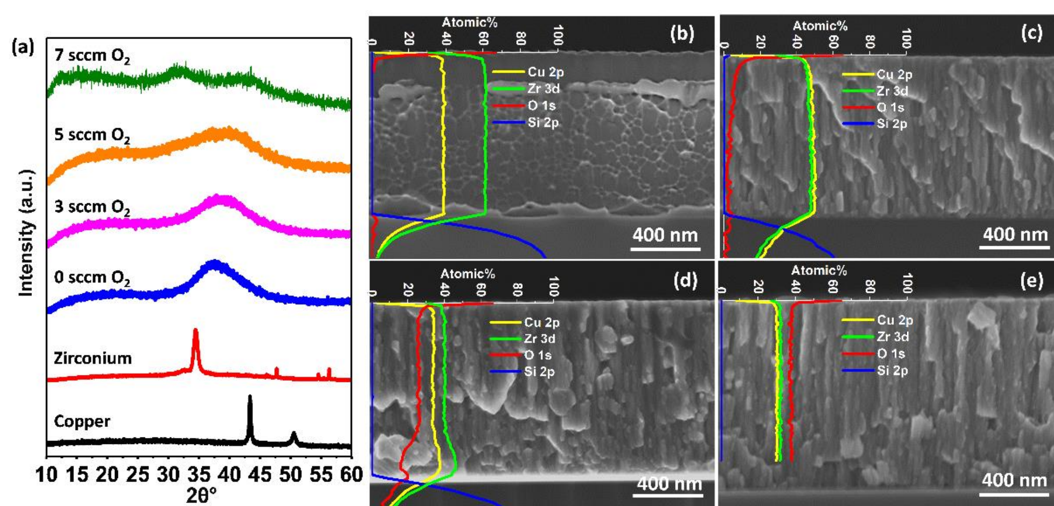

Figure 6-5. (a) XRD analysis of amorphous Cu-Zr TFMGs and SEM topography of (b) 0 sccm, (c) 3 sccm, (d) 5 sccm, (e) 7 sccm, with XPS analysis inset to the figs.

This further confirms our hypothesis that a low amount of oxygen incorporation in the films probably induces the creation of small ZrO_2 crystallites, raising the melting temperature locally and preventing vein fracture shape creation during sample cleavage [259–262].

The top smooth layer in Figure 6-4.c and Figure 6-5.b is where stable shear deformation occurs. Despite the possibility that the shear fracture may not occur simultaneously, this region proves that every part of the radial shear band will fracture with approximately the same amount of shear. The thickness of this region represents the maximum shear amount before fracture. The thinner, smooth region indicates that the film experienced a higher local strain rate [263,264].

6.2. Conclusion

In conclusion, SEM cross-section analysis revealed venous and columnar fractures in samples deposited under different conditions. These findings indicate a distinct phenomenon independent of the deposition process. The theory suggests that columnar morphology transforms into vein patterns due to deformation, energy dissipation, localized temperature rise, and melting caused by shear bands and friction upon the sample cleavage. Experimental evidence supports this concept, highlighting the role of oxygen content in fracture morphology during deposition. These discoveries significantly affect material design and engineering applications, enhancing our understanding of metallic film fractures.

Chapter 7.

7. General conclusions

This thesis aimed to understand the mechanical behavior of thin films, especially a-C:H:Cr and Cu-Zr TFMGs with an amorphous nature. The main scientific question we answered through this thesis was: can we tailor and modify the fracture behavior of the amorphous thin films only by manipulating and fine-tuning the deposition parameters and precursor gas in the PVD and PECVD process? To answer this question, this Ph.D. thesis has focused on two key research areas.

In the first part, the author addressed a gap in the current practices within the coating community by introducing a systematic material selection technique for optimizing a-C:H:Cr films based on targeted performance indices. We demonstrated that the prevailing trial-and-error approach can be improved by employing a comprehensive evaluation methodology. To achieve this objective, we selected four films out of several coatings produced under different conditions, specifically varying sputtering pressures (5 mTorr, 20 mTorr) and bias voltages (floating or -100V), using the PECVD technique and then extensively evaluated the mechanical properties of these films.

The study's findings indicate that the application of bias voltage is crucial in enhancing the film's resistance to plastic deformation and wear resistance. Furthermore, higher deposition pressure significantly improved the films' resistance to cracking under tension, regardless of the bias voltage applied. One notable outcome of the investigations is that these films exhibited a higher elastic limit, approximately 5%, compared to coatings within a similar industry class. Additionally, the films displayed tunable fracture toughness, falling into three distinct regimes: low (<10 J/m²), mid (10-100 J/m²), and high (>100 J/m²) levels.

In the second part, the SEM cross-section analysis conducted on the Cu-Zr TFMG samples deposited under various conditions unveiled the presence of venous and columnar fractures. Surprisingly, these fractures appeared to be independent of the specific deposition process employed. This intriguing observation points to a distinct phenomenon that is not solely influenced by the deposition parameters. The proposed theory suggests that the columnar morphology of the films undergoes a transformation into vein patterns when subjected to deformation. This transformation is attributed to several factors, including energy dissipation, localized temperature rise, and melting caused by SBs and friction during sample cleavage. Experimental evidence further supports this concept, emphasizing the significant role played by the oxygen content in shaping the fracture morphology during the deposition process. These compelling discoveries hold great implications for material design and engineering applications. They provide valuable insights into the fracture behavior of amorphous coatings, shedding light on the underlying mechanisms and processes involved. By deepening our understanding of film fractures and their influencing factors, we can better tailor material properties and optimize deposition techniques for improved performance and reliability in various engineering applications.

Both sections highlighted the importance of comprehensive evaluation and the need to avoid a trial-and-error approach. By proceeding with our proposed approach, scientists are now aware of their amorphous coatings' purity and knowledge of fine-tuning them to meet the exact requirements of the industry.

Our study also emphasizes that the optimization process should not solely focus on specific parameters but instead involve combining and customizing mechanical properties to meet the diverse requirements associated with different types of applications. By adopting this perspective, the author suggests that amorphous coatings with tailored properties can be developed, enhancing coating performances across various technological applications.

Chapter 8.

8. Perspectives

The current thesis posed several fresh concerns, the solutions of which may hold the key to intriguing advancements in the mechanical characteristics of thin films.

New findings in the study frequently give rise to fresh concerns. This was also the case when working on this thesis, and it was not feasible to follow up on every one of them due to time limitations. In the short term, Particularly with regard to the Cu-Zr TFMGs, there are still a number of unresolved issues whose examination might support the conclusions previously published and broaden the field of study.

The a-C:H:Cr coatings have been deposited with the constant (10 at%) Cr throughout the coatings, and their mechanical properties have been evaluated. Different amounts of Cr content could be studied further to determine the effect of doping elements besides the deposition parameters since the addition of Cr affects the residual stress, wear adhesion, and fracture toughness that we investigated during this thesis study.

In this study, we studied the tensile behavior on the flexible substrate, also some attempts have been conducted to study the mechanical properties with the lab-on-chip technique since it allows us to develop thousands of elementary testing concepts on a single Si wafer, however, due to the large residual compressive stress, pile-off process was not successful. It can be interesting to modify the residual stress and compare the mechanical properties, specifically the fracture toughness of the free-standing coatings with the results we achieved in this thesis. By this, we will be able to develop general information regarding the mechanical properties of amorphous coatings in different testing conditions and provide a reference for future works in this field.

Thin film thickness as the influencing factor of mechanical properties has not been studied deeply in this thesis, and the optimum thickness of 1 μm has been kept for all coatings. So, it is interesting to study the effect of coating thickness on the fracture behavior of the Cu-Zr TFMGs since scholarly works have been done showing the contribution of the coating thickness on the fracture behavior of metallic glass coatings. In this study, we proposed the deposition parameters where the fine-tuned fracture properties were achieved, and it can be interesting to continue investigations by tuning the total film thickness and modulation of multilayer thickness besides the specified parameters in this study.

This thesis study has made a novel claim regarding the fracture behavior of Cu-Zr TFMGs. Depper studies are under progress to investigate the Cu-rich and Zr-rich regions for the fracture cross-section with the high-resolution TOF-SIMS with depth resolution of 1nm and lateral resolution of 50nm. We hope to observe the composition map of the vein pattern to experimentally prove the segregation of Cu and Zr during the cleavage. There are not yet reported results. It is interesting to continue the fundamental investigations on Cu-Zr topic since there is a huge scientific potential and remaining discoveries for this topic.

On a longer-term view, a thorough study of the functional properties of TFMGs remains a very open scientific field. In this study, we only focused on the mechanical properties, specifically the fracture

toughness of the amorphous coatings. However, a more complete study of the corrosion behavior of the coatings will be interesting since the Cu-Zr based coatings are increasingly being used as anti-corrosion coatings. Recent studies show an extraordinary corrosion resistance of the $Cu_{40}Zr_{60}$ TFMGs [265], even in the long term. In this thesis study, we have produced the same composition under different deposition conditions. Studying the corrosion resistance of the already prepared samples and developing the novel Cu-Zr TFMGs with modified mechanical and anti-corrosion properties can be interesting. This will help explore new domains that can increase the potential use of TFMGs for high-tech applications.

Chapter 9.

9. Annex

9.1. Thin film microstructure investigation

9.1.1. X-Ray Diffraction (XRD)

The principle of the methods is based on the diffraction of X-rays by periodic atomic planes and the angle or energy-resolved detection of the diffracted signal. The geometrical interpretation of the XRD phenomenon (constructive interferences) was given by W.L. Bragg in 1913 [266]. Certain directions are thus privileged, and a network of corresponding intense points appears in the reciprocal network. Bragg's Law plays a central role in XRD analysis by relating the angles at which diffraction peaks occur to the interplanar spacing of crystal lattice planes. In a polycrystalline, untextured material with fine grains, diffraction occurs for each lattice plane and direction that satisfies Bragg’s law in the case of constructive interferences [267].

9.1.2. X-Ray Photoelectron Spectroscopy (XPS)

X-Ray Photoelectron Spectroscopy (XPS) is a surface-sensitive (probe depth ~50 Å) analysis method for quantitative, qualitative, and chemical analysis. The XPS method relies on the detection of core electrons photoemitted (PE) from the surface by monochromatic X-rays with known energies of $\boldsymbol{E_{hv}}$. X-rays with a certain energy are used to irradiate the sample's surface to start the XPS process. These X-rays have sufficient energy to interact with core electrons (typically electrons in the innermost electron shells) of the atoms in the sample. An X-ray photon can transmit enough energy to a core electron during their interaction for the electron to be ejected from its atomic orbit. The photoelectric effect is what is happening here. The term "photoelectron" refers to the ejected electron. The ejected photoelectron contains information about the origin of the element and its energy. By measuring the kinetic energy ($\boldsymbol{E_k}$) of the photoelectron, which depends on the energy of the incident X-ray and the binding energy ($\boldsymbol{E_B}$) of the electron in its initial atomic orbit, it is possible to deduce the binding energy by using the following equation:

$$\boldsymbol{E_B = E_{hv} - E_K - \varphi_{spec},} \qquad [eV] \qquad \textbf{(9-1)}$$

where $\boldsymbol{E_{hv}}$ is the energy of the incident photon (X-ray in this case, which is a known and fixed value), and $\boldsymbol{\varphi_{spec}}$ is the spectrometer extraction work. In the XPS spectrum, the intensity is plotted versus the binding energy, calculated from the energy conservation law. The benefit of the technique is that the binding energy of an element may change if the chemical environment is modified [268].

9.1.3. Scanning Electron Microscopy (SEM)

SEM is widely used to investigate the microstructure and composition of various materials. The main components of the SEM include a source of electrons, electromagnetic lenses to focus electrons,

electron detectors, sample chambers, computers, and displays to view the images. Electrons, produced at the top of the column, are accelerated downwards, passing through lenses and apertures to produce a fine beam of electrons. The electron beam hits the sample's surface mounted on a movable stage under vacuum. This beam scanning enables information about a defined area of the sample. The interaction of the electron beam with the sample generates several signals, which appropriate detectors can then detect. The advantages of SEM include detailed three-dimensional (3D) topographical imaging and versatile information obtained from different detectors. The microscope is easy to operate, and the associated software is user-friendly. SEM can also be used to analyze the film's morphology and directly measure its thickness when looking at the film's cross-section [269].

9.1.4. Transmission Electron Microscopy (TEM)

The microscopy method known as transmission electron microscopy (TEM) involves transmitting an electron beam through a very thin material while having the electrons interact with it. Electrons transported through the material interact with one another, creating a picture. The picture is enlarged and focussed onto a layer of photographic film, a fluorescent screen, or a sensor like a charge coupled device (CCD). The TEM functions similarly to a light microscope but uses electrons instead of light. The best resolution feasible for TEM pictures is many orders of magnitude better than that from a light microscope because the wavelength of electrons is significantly less than that of light. Consequently, TEMs may provide the most precise data about interior structure, perhaps even down to the level of individual atoms [270].

9.1.5. Raman Spectroscopy

Raman spectroscopy is an effective, non-destructive characterization method that examines the rotation and vibration of molecules. In an experiment, the sample is exposed to a monochromatic incoming beam that is generally in the visible spectrum, and the radiation that is scattered from the sample is then measured. Although some photons in the scattered light have been dispersed inelastically, most of the photons in the scattered light have the same frequency as the input radiation (Rayleigh Scattering). Only about 1 in 10^7 photons emerge with a change in frequency, and this scattering is called Raman scattering. Figure 9-1 shows the principle of Raman scattering [271].

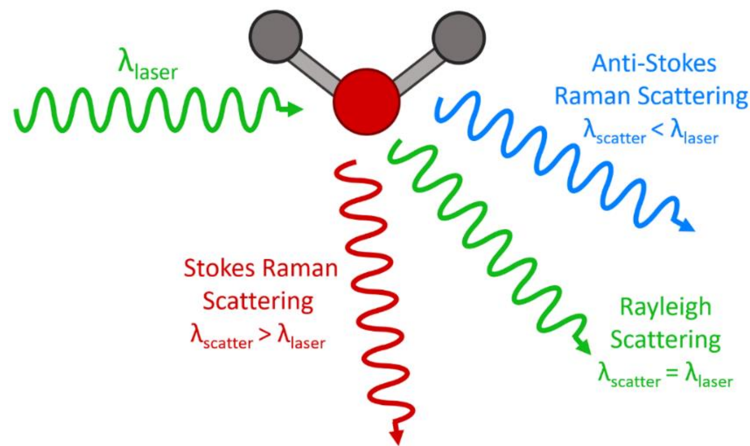

Figure 9-1. Diagram of the Rayleigh and Raman scattering processes [271].

9.1.6. Atomic Force Microscopy (AFM)

Atomic force microscopy (AFM) allows for the imaging of nearly any surface, including polymers, ceramics, composites, glass, and biological materials. Adhesion strength, magnetic forces, and mechanical characteristics are just a few of the various forces that may be measured and localized with AFM. In this method, a laser beam reflected by a cantilever that holds the AFM tip is focused onto a photodiode to monitor the movement of the AFM tip in response to tip-surface interactions. Contact mode and tapping mode are two fundamental ways to use an AFM. The AFM tip constantly touches the surface while operating in contact mode [272].

In contrast, the AFM cantilever vibrates above the sample surface in the tapping mode, resulting in only occasional contact between the tip and the surface. In doing this, the shear pressures brought on by tip movement are lessened. Therefore, the suggested method for AFM imaging is tapping mode, which is often employed. The highest height the AFM can detect is on the order of micrometers, and the largest scanning area is around 150 by 150 micrometers [272]. The Schematic of the AFM device is seen in Figure 9-2.

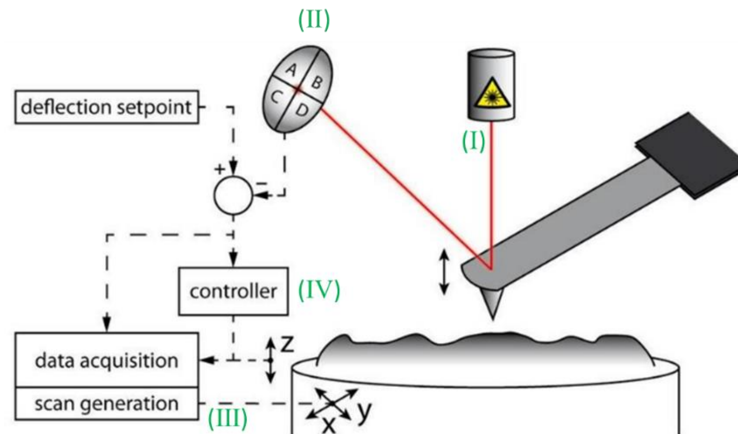

Figure 9-2. Schematic of an atomic force microscope with (I) laser beam reflected by a cantilever, (II) position sensitive photodetector to measure the deflection, (III) piezoelectric scanner to position the sample with Å accuracy, (IV) sample's Z-axis controller [273].

9.2. Thin film mechanical properties

9.2.1. Nanoindentation and micro-scratch test

Nanoindentation is the most used technique to determine the nano and micro-sized materials' mechanical properties, such as hardness, elastic modulus, fracture toughness, creep, and dynamic properties, such as storage and loss moduli [274].

The nanoindentation technique is quite simple: it utilizes a diamond tip that is in contact with the material's surface, and by increasing the force, the tip begins to penetrate the surface and make an impression [275]. By continuously applying the force, the displacement sensor positioned close to the indenter tip measures the indenter's vertical displacement as it penetrates the material's surface. Then, the load-displacement curve will be plotted. Then, the final result from the indentation test is the amount of hardness, which is then calculated as the force applied to the material's surface divided by the projected area of the contact surface between the tip and the sample.

Not only can nanoindentation measure the hardness and elastic modulus, but it also can be used to estimate the yield strength of a material. This method has its own drawbacks reported in the literature, such as substrate pile-up and sink-in effects [276].

Below is the calculation formula for the nanoindentation hardness of a material

$$H = \frac{Fmax}{A_p}, \quad (9\text{-}2)$$

where H is the sample hardness, F_{max} is the maximum pre-defined load during the indentation test, and A_p is the projected contact area between the indenter tip and the sample at maximum load. F_{max} is measured directly by nanoindentation; however, it is not obvious for the device to calculate the contact area, A_p. For this purpose, the well-established Oliver-Pharr method calculates the A_p. A detailed description of this method is available in the literature, and here the procedure is mentioned [170,171]. Firstly, contact stiffness, S, is calculated in this method which shows the maximum depth at the time that force is applied to the sample's surface. For this purpose, a power-law curve fit was performed on the unloading segment of the force-displacement curve in the form

$$F = A(h - h_f)^m, \tag{9-3}$$

Here F is load as a function of h, which is the displacement into the surface, h_f is the x-intercept of the unloading curve, as labeled in Figure 9-3.

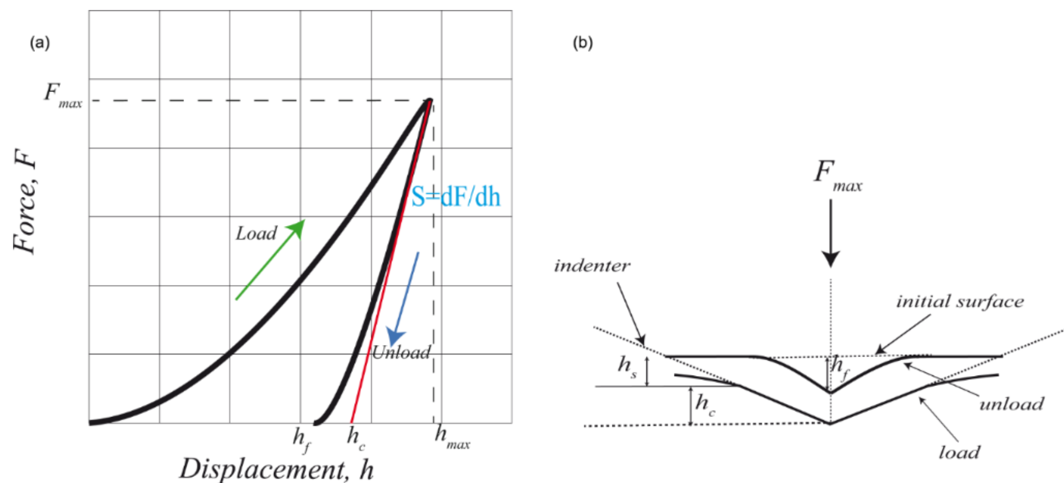

Figure 9-3. The schematic of a load-displacement curve for indentation [69].

Then according to the mentioned formula, $S = \frac{dF}{dh}$ the contact stiffness is calculated at h_{max}, where h_{max} is the maximum displacement into the sample. Next, contact depth, h_c can be calculated. Calculation of this parameter is related to the shape of the indenter and remaining features on the surface. If the shape of the indenter is three-dimensional, during the tip and the sample touch each other, the contact depth is the height of this surface along the sample surface normal. In order to determine the contact depth, Sneddon's expression is used as

$$h_c = h_{max} - \varepsilon(\frac{F_{max}}{s}), \tag{9-4}$$

Therefore, A_p can be calculated from equation (2.7), which is a direct and obvious relationship between the contact depth of the indenter and the projected area of the contact, and the geometry of the indenter itself defines this relation. Here due to the usage of the Berkovich tip, A_p can be defined as

$$A_p = 24.5{h_c}^2. \tag{9-5}$$

The key point for calculating the mechanical properties of thin film materials is to minimize the effect of the substrate on the measurement. For this purpose, the indentation depth has to be limited to less than 10% of the film thickness. However, this district rule is not always reliable, especially if the elastic mismatch between film and substrate is large. Also, another problem is that the 10% rule is not useful for very thin films when experimental issues make it difficult to obtain accurate results for very shallow indentations [275].

9.2.2. Tensile testing on polymer substrate

The most practical material characterization test currently available may be the uniaxial tensile test. It measures the force necessary to stretch a test specimen over time in increasing increments until it cracks. Elasticity, plasticity, and ultimate strength are three crucial material qualities measured by the test. In addition, it produces stress-strain curves, a quantitative representation of a material's mechanical characteristics. The stress-strain curve obtained from the tensile test is shown in Figure 9-4.

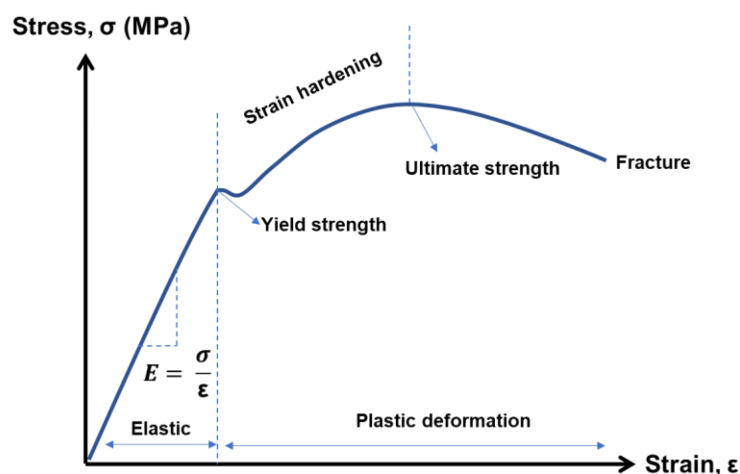

Figure 9-4. Stress-Strain diagram.

The stress and strain develop linearly throughout a tensile test until they reach the proportional limit just below the yielding point. Youngs's modulus (E) is one of the characteristics of the material that can be extracted from the slope of the curve up to this point. When the stress and strain reach the elastic limit, also known as the yield strength point, the material's behavior changes from elastic to plastic.

Before the stress reaches a final stress point, the nonlinear stress lowers to a smaller yield, symbolizing the dislocations of atoms. The term "strain hardening" refers to this area. Beyond the point of ultimate strength, the stress decreases due to necking to a final fracture of the specimen. If the stress (and therefore strain) applied to a material is below the yield strength, both the stress and strain will recover to zero by removing the applied force. However, if the elastic limit is exceeded, only the elastic strain will be recovered, and the plastic strain will remain as a permanent set. Since it is usually undesirable to experience a permanent set in a component, engineers would like to design parts so that the expected service stress is less than the elastic limit or modify the material to increase the stress where plastic deformation begins by some reasonable factor of safety.

9.3. Additional findings about Cu-Zr TFMGs

In the course of this Ph.D. investigation, I have contributed to elucidating the underlying mechanism and determining the predominant driving forces responsible for various fracture characteristics observed in Cu-Zr TFMGs. Furthermore, I have successfully engineered a multilayer coating consisting of four distinct, identifiable layers characterized by vein-like and columnar fracture patterns, all encapsulated within a single specimen (see Figure 9-5). In order to gain a comprehensive understanding of the influence of each parameter on the material's mechanical properties, it is imperative to conduct a thorough examination of the effects stemming from variations in sublayer thickness, the number of layers, and different compositional configurations within such a multilayered film.

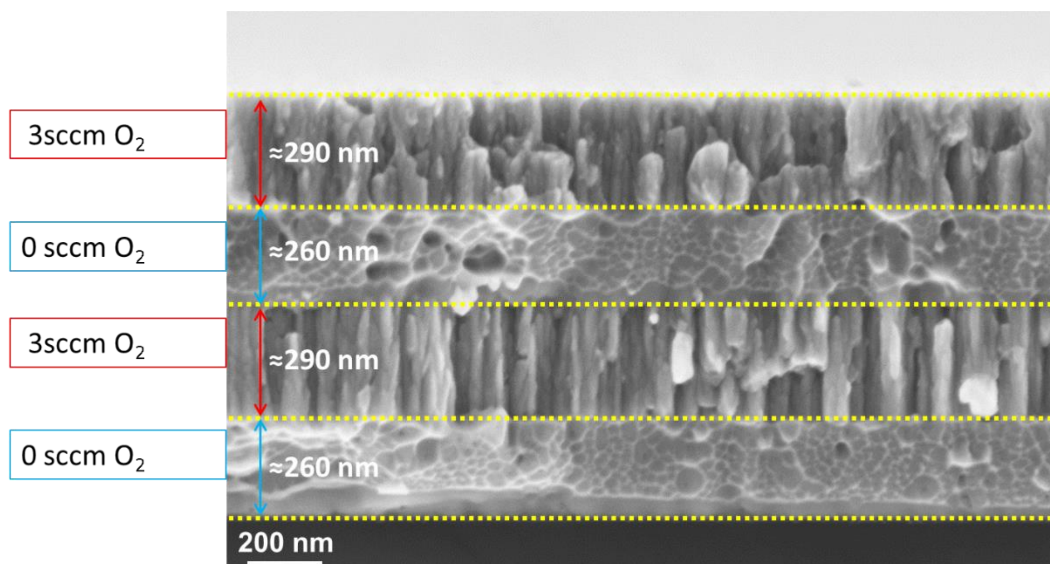

Figure 9-5. SEM micrograph of multilayered Cu-Zr TFMG with and without oxygen.

In the scope of this thesis, we studied the mechanical properties of a couple of samples in this group, which the comparison is inserted in Table 9-1 and Table 9-2. In this table single layer without oxygen

injection during the deposition is named (SL0), the single layer with 3 sccm of oxygen injection as (SL3), and the multilayered sample with and without oxygen injection is named (ML0/3).

Table 9-1. Comparison in mechanical properties of single layer (SL) and multilayer (ML) with and without oxygen injection during the deposition process. (a) SL0 (b) SL3, and (c) ML0/3.

	H (GPa)	E' (GPa)	H/E'	H^3/E'^2 (GPa)	σ_y (GPa)	σ_y/E
a	4.8 ± 0.3	110 ± 4.7	$4.36 \pm 0.3\text{x}10^{-2}$	$9.14 \pm 0.6\ \text{x}10^{-3}$	2.04 ± 0.09	0.018
b	5.09 ± 0.2	134 ± 5.4	$3.78 \pm 0.2\text{x}10^{-2}$	$7.29 \pm 0.4\ \text{x}10^{-3}$	2.12 ± 0.07	0.016
c	3.9 ± 0.1	110 ± 1.1	$3.56 \pm 0.1\text{x}10^{-2}$	$5.03 \pm 0.1\ \text{x}10^{-3}$	1.6 ± 0.03	0.015

Table 9-2. Comparison in fracture behavior of single layer (SL) and multilayer (ML) with and without oxygen injection during deposition. (a) SL0 (b) SL3, and (c) ML0/3 extracted from vein patterns width.

	Vein width (nm)	K_{Ic} (MPa.$\sqrt{m}$)	G_{Ic} (J/m^2)	Process zone size (nm)
a	53.8 ± 3	3 ± 0.2	81.5 ± 7.8	685 ± 57.5
c	38 ± 2.9	2 ± 0.1	36.4 ± 6.9	484 ± 40.2

These comparisons show a slight increase in hardness and yield strength of the sample by injection of tiny amounts of oxygen that seems to be due to oxide nucleation and dispersion, as discussed in detail in [119,277,278]. However, a deeper understanding is needed based on microstructure and chemical characterization.

Fracture toughness and fracture energy release rate have been compared with the literature and results show a good agreement with other works also, effect of multilayering is obvious. Increase in fracture toughness with decreasing the

Table 9-3. Comparison of fracture toughness and fracture energy release rate.

Study	Fracture toughness ($\boldsymbol{MPa.\sqrt{m}}$)	Fracture energy (J/m^2)
[123]	3.84	157.9
[126]	2.7±0.5	60
[128]	3.7 ± 0.4	147.2
5 mTorr/-100V with 225nm sublayer thickness	4.73±0.66	151.3
5 mTorr/-100V with 150nm sublayer thickness	4.49±0.58	133.5
5 mTorr/-100V with 40nm sublayer thickness	5.04±0.71	176.1
5 mTorr/-100V with 20nm sublayer thickness	4.34±0.44	127.3

5 mTorr/-100V with 10nm sublayer thickness	4.21±0.26	130.0
5 mTorr/-100V with Mono-layer	3.00±0.21	81.5
20 mTorr/-100V with Mono-layer	3.74±0.21	119.5

While numerous studies have focused on the mechanical properties and improvements of Cu-Zr TFMGs using various methods, there has been a lack of comprehensive investigations specifically targeting the fracture behavior of these coatings in different deposition conditions.

Besides that, we were able to mimic vein-like fracture features even with the presence of oxygen, which can be called reverse engineering, by using the laser beam for the regional melting process (approximately above 2000 °C) and solidification (see Figure 9-6).

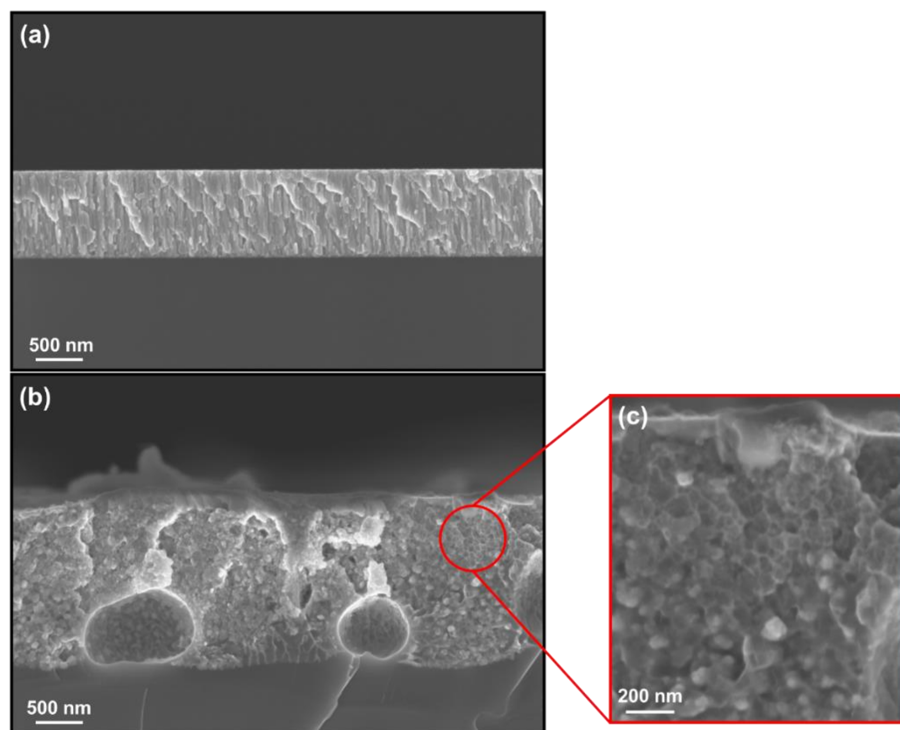

Figure 9-6. Conversion of (a) columnar fracture patterns to (b) vein-like feature after laser treatment. (c) shows higher magnification of the fracture cross-section with vein patterns.

This experiment shows the ability to customize the Cu-Zr TFMGs produced in this project; however, it needs a deeper understanding and study of microscopic phenomena behind each occurrence.

9.4. In-situ SEM tensile tests

Thin film fracture happens in three steps: crack initiation, crack propagation, and crack enlargement. Figure 9-7 shows the crack propagation and enlargement during the tensile testing for different samples where the evolution of saturation crack density inserted in Table 5-3 has been calculated at $\varepsilon = 25\%$.

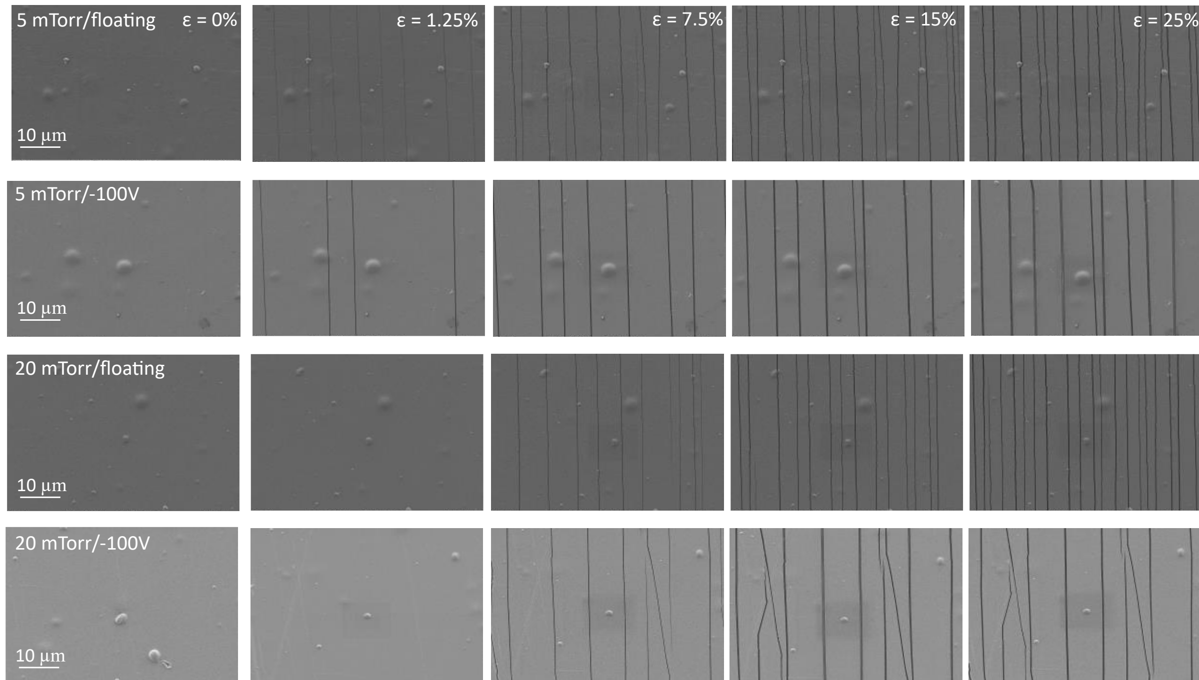

Figure 9-7. Fragmentation mechanism of a-C:H:Cr films on polymer substrate during tensile testing.

Chapter 10.

10. References

[1] E. Acosta, Thin Films/Properties and Applications, in: Thin Films, IntechOpen, 2021. https://doi.org/10.5772/intechopen.95527.

[2] K. Wasa, M. Kitabatake, H. Adachi, Thin film materials technology: sputtering of compound materials, William Andrew Pub. ; Springer, Norwich, NY : Heidelberg, 2004.

[3] K.L. Chopra, I. Kaur, Thin Film Technology: An Introduction, in: K.L. Chopra, I. Kaur (Eds.), Thin Film Device Appl., Springer US, Boston, MA, 1983: pp. 1–54. https://doi.org/10.1007/978-1-4613-3682-2_1.

[4] Thin Film Coatings Market - Global Industry Analysis by Type, Application, Region and Forecast (2022-2029), MAXIMIZE Mark. Res. (n.d.). https://www.maximizemarketresearch.com/market-report/global-thin-film-coatings-market/102853/ (accessed September 20, 2023).

[5] M. Sathish, N. Radhika, B. Saleh, A critical review on functionally graded coatings: Methods, properties, and challenges, Compos. Part B Eng. 225 (2021) 109278. https://doi.org/10.1016/j.compositesb.2021.109278.

[6] V.H. de Vargas, L.D.F. Marczak, S.H. Flôres, G.D. Mercali, Advanced Technologies Applied to Enhance Properties and Structure of Films and Coatings: a Review, Food Bioprocess Technol. 15 (2022) 1224–1247. https://doi.org/10.1007/s11947-022-02768-6.

[7] Coatings | Free Full-Text | Coating a Sustainable Future, (n.d.). https://www.mdpi.com/2079-6412/10/8/713 (accessed September 7, 2023).

[8] L. Freund, S. Suresh, Thin film materials: stress, defect formation and surface evolution, 2004. https://books.google.com/books?hl=en&lr=&id=9UNnzNYAkboC&oi=fnd&pg=PR16&dq=Freund+LB,+Suresh+S+(2003)+Thin+film+materials:+stress,+defect+formation,+and+surface+evolution.+Cambridge+University+Press,+Cambridge&ots=Ne0GJvVSvI&sig=j8MK9hv_e10_g9S6pWP0JchjwRc.

[9] F. Spaepen, A.L. Shull, Mechanical properties of thin films and multilayers, Curr. Opin. Solid State Mater. Sci. 1 (1996) 679–683. https://doi.org/10.1016/S1359-0286(96)80051-9.

[10] W.D. Nix, Mechanical properties of thin films, Metall. Trans. A 20 (1989) 2217. https://doi.org/10.1007/BF02666659.

[11] P. Cavaliere, Mechanical Properties of Thin Films and Coatings, in: P. Cavaliere (Ed.), Fatigue Fract. Nanostructured Mater., Springer International Publishing, Cham, 2021: pp. 333–366. https://doi.org/10.1007/978-3-030-58088-9_8.

[12] N. Ding, Y. Qin, G. Yang, F. Wei, Z. Yang, Y. Su, S. Hu, Y. Chen, C.-M. Chan, W. Chen, J. Yi, W. Zhao, X. Wang, Z. Liu, H.-T. Zheng, J. Chen, Y. Liu, J. Tang, J. Li, M. Sun, Parameter-efficient fine-tuning of large-

scale pre-trained language models, Nat. Mach. Intell. 5 (2023) 220–235. https://doi.org/10.1038/s42256-023-00626-4.

[13] Z. Zhang, J. Yuan, Z. Jing, Y. Cheng, X. Liang, Research Progress and Development Trend of Amorphous and Nanocrystalline Composite Coatings: A Review, JOM 74 (2022) 4597–4611. https://doi.org/10.1007/s11837-022-05527-2.

[14] K.A. Lee, D.J. Jung, D.Y. Park, W.G. Kang, J.K. Lee, H.J. Kim, Study on the fabrication and physical properties of cold-sprayed, Cu-based amorphous coating, J. Phys. Conf. Ser. 144 (2009) 012113. https://doi.org/10.1088/1742-6596/144/1/012113.

[15] Y. Li, L.-Y. Zhang, C. Zhang, Z.-R. Zhang, L. Liu, Bioinspired antifouling Fe-based amorphous coating via killing-resisting dual surface modifications, Sci. Rep. 12 (2022) 819. https://doi.org/10.1038/s41598-021-04746-y.

[16] Y. Ma, M. Li, F. Zu, The Tribological Behaviors in Zr-Based Bulk Metallic Glass with High Heterogeneous Microstructure, Materials 15 (2022) 7772. https://doi.org/10.3390/ma15217772.

[17] H. Okamoto, Cu-Zr (Copper-Zirconium), J. Phase Equilibria Diffus. 33 (2012) 417–418. https://doi.org/10.1007/s11669-012-0077-1.

[18] J. Zhu, C. Gu, K.W. Xu, P. Huang, F. Wang, T.J. Lu, Effects of size and amorphous layer structure on the strength and plasticity of Cu/CuZr nanolaminates, Mater. Sci. Eng. A 738 (2018) 219–228. https://doi.org/10.1016/j.msea.2018.09.071.

[19] S.H. Zhou, R.E. Napolitano, Phase stability for the Cu–Zr system: First-principles, experiments and solution-based modeling, Acta Mater. 58 (2010) 2186–2196. https://doi.org/10.1016/J.ACTAMAT.2009.12.004.

[20] M.-Y. Bai, Y.-C. Chang, J.P. Chu, Preclinical studies of non-stick thin film metallic glass-coated syringe needles, Sci. Rep. 10 (2020) 20313. https://doi.org/10.1038/s41598-020-77008-y.

[21] Y. Cui, O.T. Abad, F. Wang, P. Huang, T.-J. Lu, K.-W. Xu, J. Wang, Plastic Deformation Modes of CuZr/Cu Multilayers, Sci. Rep. 6 (2016) 23306. https://doi.org/10.1038/srep23306.

[22] C. Casiraghi, J. Robertson, A.C. Ferrari, Diamond-like carbon for data and beer storage, Mater. Today 10 (2007) 44–53. https://doi.org/10.1016/S1369-7021(06)71791-6.

[23] P. Bruno, G. Cicala, A.M. Losacco, P. Decuzzi, Mechanical properties of PECVD hydrogenated amorphous carbon coatings via nanoindentation and nanoscratching techniques, Surf. Coat. Technol. 180–181 (2004) 259–264. https://doi.org/10.1016/j.surfcoat.2003.10.035.

[24] C. Kranz, ed., Carbon-Based Nanosensor Technology, Springer International Publishing, Cham, 2019. https://doi.org/10.1007/978-3-030-11864-8.

[25] S. Neuville, New application perspective for tetrahedral amorphous carbon coatings, QScience Connect 2014 (2014) 8. https://doi.org/10.5339/CONNECT.2014.8.

[26] A. Jilani, M.S. Abdel-wahab, A. HosnyHammad, A. Jilani, M.S. Abdel-wahab, A. HosnyHammad, Advance Deposition Techniques for Thin Film and Coating, in: Mod. Technol. Creat. Thin-Film Syst. Coat., IntechOpen, 2017. https://doi.org/10.5772/65702.

[27] Y. Hamedani, P. Macha, T.J. Bunning, R.R. Naik, M.C. Vasudev, Y. Hamedani, P. Macha, T.J. Bunning, R.R. Naik, M.C. Vasudev, Plasma-Enhanced Chemical Vapor Deposition: Where we are and the Outlook for the Future, in: Chem. Vap. Depos. - Recent Adv. Appl. Opt. Sol. Cells Solid State Devices, IntechOpen, 2016. https://doi.org/10.5772/64654.

[28] M. Hapgood, Linking Space Weather Science to Impacts—The View From the Earth, in: Extreme Events Geosp., Elsevier, 2018: pp. 3–34. https://doi.org/10.1016/B978-0-12-812700-1.00001-7.

[29] D.G. Rickerby, A.M. Serventi, Nanostructured Metal Oxide Gas Sensors for Air-Quality Monitoring, in: Environanotechnology, Elsevier, 2010: pp. 99–136. https://doi.org/10.1016/B978-0-08-054820-3.00006-X.

[30] M.A. Lieberman, A.J. Lichtenberg, Principles of Plasma Discharges and Materials Processing: Lieberman/Plasma 2e, John Wiley & Sons, Inc., Hoboken, NJ, USA, 2005. https://doi.org/10.1002/0471724254.

[31] L. Aissani, A. Alhussein, A.W. Zia, G. Mamba, S. Rtimi, Magnetron Sputtering of Transition Metal Nitride Thin Films for Environmental Remediation, Coatings 12 (2022) 1746. https://doi.org/10.3390/coatings12111746.

[32] J.D. Musgraves, J. Hu, L. Calvez, eds., Springer Handbook of Glass, Springer International Publishing, Cham, 2019. https://doi.org/10.1007/978-3-319-93728-1.

[33] B. Rauschenbach, Low-Energy Ion Irradiation of Materials: Fundamentals and Application, Springer International Publishing, Cham, 2022. https://doi.org/10.1007/978-3-030-97277-6.

[34] M. Ohring, Materials Science of Thin Films, Elsevier, 2002. https://doi.org/10.1016/b978-0-12-524975-1.x5000-9.

[35] R.J. Shul, S.J. Pearton, Handbook of Advanced Plasma Processing Techniques, Springer Science & Business Media, 2011.

[36] J.T. Gudmundsson, Physics and technology of magnetron sputtering discharges, Plasma Sources Sci. Technol. 29 (2020) 113001. https://doi.org/10.1088/1361-6595/abb7bd.

[37] K. Wasa, I. Kanno, H. Kotera, eds., Handbook of sputter deposition technology: fundamentals and applications for functional thin films, nanomaterials and MEMS, 2nd ed, William Andrew, Waltham, MA, 2012.

[38] Introduction to Surface Engineering and Functionally Engineered Materials, in: Introd. Surf. Eng. Funct. Eng. Mater., John Wiley & Sons, Inc., Hoboken, NJ, USA, 2011: pp. i–xv. https://doi.org/10.1002/9781118171899.fmatter.

[39] D. Yang, Applications of Laser Ablation: Thin Film Deposition, Nanomaterial Synthesis and Surface Modification, BoD – Books on Demand, 2016.

[40] A. Anders, A structure zone diagram including plasma-based deposition and ion etching, Thin Solid Films 518 (2010) 4087–4090. https://doi.org/10.1016/j.tsf.2009.10.145.

[41] J.A. Thornton, High Rate Thick Film Growth, Annu. Rev. Mater. Sci. 7 (1977) 239–260. https://doi.org/10.1146/annurev.ms.07.080177.001323.

[42] J.A. Thornton, Influence of apparatus geometry and deposition conditions on the structure and topography of thick sputtered coatings, J. Vac. Sci. Technol. 11 (1974) 666–670. https://doi.org/10.1116/1.1312732.

[43] E. Kusano, Structure-Zone Modeling of Sputter-Deposited Thin Films: A Brief Review, Appl. Sci. Converg. Technol. 28 (2019) 179–185. https://doi.org/10.5757/ASCT.2019.28.6.179.

[44] P. Ossi, Disordered Materials: An Introduction, Springer Science & Business Media, 2010.

[45] P. Chaudhari, D. Turnbull, Structure and Properties of Metallic Glasses, Science 199 (1978) 11–21. https://doi.org/10.1126/science.199.4324.11.

[46] Y. Yue, The hardest amorphous material, Natl. Sci. Rev. 9 (2021) nwab203. https://doi.org/10.1093/nsr/nwab203.

[47] X. Liu, J. Bi, Z. Meng, Y. Ke, R. Li, T. Zhang, Development of Co-Based Amorphous Composite Coatings Synthesized by Laser Cladding for Neutron Shielding, Materials 14 (2021) 279. https://doi.org/10.3390/ma14020279.

[48] J.K. Christie, Review: understanding the properties of amorphous materials with high-performance computing methods, Philos. Trans. R. Soc. Math. Phys. Eng. Sci. 381 (2023) 20220251. https://doi.org/10.1098/rsta.2022.0251.

[49] M.F. Thorpe, L. Tichý, eds., Properties and Applications of Amorphous Materials, Springer Netherlands, Dordrecht, 2001. https://doi.org/10.1007/978-94-010-0914-0.

[50] Z.-Q. Hu, A.-M. Wang, H.-F. Zhang, Amorphous Materials, in: Mod. Inorg. Synth. Chem., Elsevier, 2017: pp. 641–667. https://doi.org/10.1016/B978-0-444-63591-4.00022-7.

[51] Y.Q. Cheng, E. Ma, Atomic-level structure and structure–property relationship in metallic glasses, Prog. Mater. Sci. 56 (2011) 379–473. https://doi.org/10.1016/j.pmatsci.2010.12.002.

[52] A.L. Greer, Crystallization of Amorphous Alloys, Metall. Mater. Trans. A 27 (1996) 549–555. https://doi.org/10.1007/BF02648945.

[53] A.C. Ferrari, J. Robertson, M.G. Beghi, C.E. Bottani, R. Ferulano, R. Pastorelli, Elastic constants of tetrahedral amorphous carbon films by surface Brillouin scattering, Appl. Phys. Lett. 75 (1999) 1893. https://doi.org/10.1063/1.124863.

[54] V. Negri, J. Pacheco-Torres, D. Calle, P. López-Larrubia, Carbon Nanotubes in Biomedicine, Top. Curr. Chem. 378 (2020) 15. https://doi.org/10.1007/s41061-019-0278-8.

[55] Z. Zhai, H. Shen, J. Chen, Y. Jiang, Q. Tang, Investigation of substrate temperature and cooling method on the properties of amorphous carbon films by hot-filament CVD with acetylene, Carbon 117 (2017) 322–330. https://doi.org/10.1016/j.carbon.2017.03.006.

[56] A. Fauroux, C. Vandenabeele, A. Pflug, S. Lucas, Experimental and theoretical study of a magnetron DC-PECVD acetylene discharge: Determination of the main species and reactions taking place in the plasma, Elsevier B.V, 2020. https://doi.org/10.1016/j.surfcoat.2020.126195.

[57] J. Robertson, Diamond-like amorphous carbon, 2002. https://doi.org/10.1016/s0927-796x(02)00005-0.

[58] A.C. Ferrari, J. Robertson, M.G. Beghi, C.E. Bottani, R. Ferulano, R. Pastorelli, Elastic constants of tetrahedral amorphous carbon films by surface Brillouin scattering, Appl. Phys. Lett. 75 (1999) 1893. https://doi.org/10.1063/1.124863.

[59] P. Koidl, Ch. Wild, B. Dischler, J. Wagner, M. Ramsteiner, Plasma Deposition, Properties and Structure of Amorphous Hydrogenated Carbon Films, Mater. Sci. Forum 52–53 (1991) 41–70. https://doi.org/10.4028/www.scientific.net/MSF.52-53.41.

[60] A.C. Popescu, G.E. Stan, L. Duta, C. Nita, C. Popescu, V.-A. Surdu, M.-A. Husanu, B. Bita, R. Ghisleni, C. Himcinschi, V. Craciun, The Role of Ambient Gas and Pressure on the Structuring of Hard Diamond-Like Carbon Films Synthesized by Pulsed Laser Deposition, Mater. 2015 Vol 8 Pages 3284-3305 8 (2015) 3284–3305. https://doi.org/10.3390/MA8063284.

[61] I.-S. Kim, C.-E. Shim, S.W. Kim, C.-S. Lee, J. Kwon, K.-E. Byun, U. Jeong, Amorphous Carbon Films for Electronic Applications, Adv. Mater. n/a (n.d.) 2204912. https://doi.org/10.1002/adma.202204912.

[62] D.G. McCulloch, D.R. McKenzie, C.M. Goringe, Ab initio simulations of the structure of amorphous carbon, Phys. Rev. B 61 (2000) 2349–2355. https://doi.org/10.1103/PhysRevB.61.2349.

[63] A. Brognara, J.P. Best, P. Djemia, D. Faurie, G. Dehm, M. Ghidelli, Effect of composition and nanostructure on the mechanical properties and thermal stability of Zr100-xCux thin film metallic glasses, Mater. Des. 219 (2022) 110752. https://doi.org/10.1016/j.matdes.2022.110752.

[64] C.-C. Yu, C.M. Lee, J.P. Chu, J.E. Greene, P.K. Liaw, Fracture-resistant thin-film metallic glass: Ultra-high plasticity at room temperature, APL Mater. 4 (2016) 116101. https://doi.org/10.1063/1.4966932.

[65] M. Ghidelli, A. Orekhov, A.L. Bassi, G. Terraneo, P. Djemia, G. Abadias, M. Nord, A. Béché, N. Gauquelin, J. Verbeeck, J.-P. Raskin, D. Schryvers, T. Pardoen, H. Idrissi, Novel class of nanostructured metallic glass films with superior and tunable mechanical properties, Acta Mater. (2021) 116955. https://doi.org/10.1016/j.actamat.2021.116955.

[66] Z.Q. Liu, W.H. Wang, M.Q. Jiang, Z.F. Zhang, Intrinsic factor controlling the deformation and ductile-to-brittle transition of metallic glasses, Philos. Mag. Lett. 94 (2014) 658–668. https://doi.org/10.1080/09500839.2014.955548.

[67] W.H. Wang, J.J. Lewandowski, A.L. Greer, Understanding the Glass-forming Ability of $Cu_{50}Zr_{50}$ Alloys in Terms of a Metastable Eutectic, J. Mater. Res. 20 (2005) 2307–2313. https://doi.org/10.1557/jmr.2005.0302.

[68] Q. Guo, L. Zhang, A.S. Zeiger, Y. Li, K.J. Van Vliet, C.V. Thompson, Compositional dependence of Young's moduli for amorphous Cu–Zr films measured using combinatorial deposition on microscale cantilever arrays, Scr. Mater. 64 (2011) 41–44. https://doi.org/10.1016/j.scriptamat.2010.08.061.

[69] A. Rauf, C.Y. Guo, Y.N. Fang, Z. Yu, B.A. Sun, T. Feng, Binary Cu-Zr thin film metallic glasses with tunable nanoscale structures and properties, J. Non-Cryst. Solids 498 (2018) 95–102. https://doi.org/10.1016/j.jnoncrysol.2018.06.015.

[70] M. Apreutesei, P. Steyer, A. Billard, L. Joly-Pottuz, C. Esnouf, Zr-Cu thin film metallic glasses: An assessment of the thermal stability and phases' transformation mechanisms, J. Alloys Compd. 619 (2015) 284–292. https://doi.org/10.1016/j.jallcom.2014.08.253.

[71] P. Coddet, F. Sanchette, J.C. Rousset, O. Rapaud, C. Coddet, On the elastic modulus and hardness of co-sputtered Zr-Cu-(N) thin metal glass films, Surf. Coat. Technol. 206 (2012) 3567–3571. https://doi.org/10.1016/j.surfcoat.2012.02.036.

[72] M. Apreutesei, P. Steyer, L. Joly-Pottuz, A. Billard, J. Qiao, S. Cardinal, F. Sanchette, J.M. Pelletier, C. Esnouf, Microstructural, thermal and mechanical behavior of co-sputtered binary Zr-Cu thin film metallic glasses, Thin Solid Films 561 (2014) 53–59. https://doi.org/10.1016/j.tsf.2013.05.177.

[73] H.W. Sheng, W.K. Luo, F.M. Alamgir, J.M. Bai, E. Ma, Atomic packing and short-to-medium-range order in metallic glasses, Nature 439 (2006) 419–425. https://doi.org/10.1038/nature04421.

[74] M. Ghidelli, S. Gravier, J.-J. Blandin, T. Pardoen, J.-P. Raskin, F. Mompiou, Compositional-induced structural change in ZrxNi100−x thin film metallic glasses, J. Alloys Compd. 615 (2014) S348–S351. https://doi.org/10.1016/j.jallcom.2013.12.054.

[75] M. Leocmach, H. Tanaka, Roles of icosahedral and crystal-like order in the hard spheres glass transition, Nat. Commun. 3 (2012) 974. https://doi.org/10.1038/ncomms1974.

[76] Y. Jiang, P. Peng, Correlation between the chemical order and nature property of Cu-centered Cu-Zr icosahedral clusters, Mater. Res. Express 5 (2018) 046302. https://doi.org/10.1088/2053-1591/aab8e8.

[77] J. Du, B. Wen, R. Melnik, Y. Kawazoe, Phase stability, elastic and electronic properties of Cu–Zr binary system intermetallic compounds: A first-principles study, J. Alloys Compd. 588 (2014) 96–102. https://doi.org/10.1016/j.jallcom.2013.11.018.

[78] Y. Saito, S. Hatayama, W. Hsin Chang, N. Okada, T. Irisawa, F. Uesugi, M. Takeguchi, Y. Sutou, P. Fons, Discovery of a metastable van der Waals semiconductor via polymorphic crystallization of an amorphous film, Mater. Horiz. 10 (2023) 2254–2261. https://doi.org/10.1039/D2MH01449A.

[79] K.A. Jackson, B. Chalmers, Kinetics of solidification, Can. J. Phys. 34 (1956) 473–490. https://doi.org/10.1139/p56-054.

[80] P.K. Galenko, V. Ankudinov, K. Reuther, M. Rettenmayr, A. Salhoumi, E.V. Kharanzhevskiy, Thermodynamics of rapid solidification and crystal growth kinetics in glass-forming alloys, Philos. Trans. R. Soc. Math. Phys. Eng. Sci. 377 (2019) 20180205. https://doi.org/10.1098/rsta.2018.0205.

[81] Y. Liu, S. Liu, C. Zhang, Y. Du, J. Wang, Y. Li, Experimental Investigation and Thermodynamic Description of the Cu-Zr System, J. Phase Equilibria Diffus. 38 (2017) 121–134. https://doi.org/10.1007/s11669-017-0522-2.

[82] C.A. Schuh, T.C. Hufnagel, U. Ramamurty, Mechanical behavior of amorphous alloys, Acta Mater. 55 (2007) 4067–4109. https://doi.org/10.1016/j.actamat.2007.01.052.

[83] L. Fast, J.M. Wills, B. Johansson, O. Eriksson, Elastic constants of hexagonal transition metals: Theory, Phys. Rev. B 51 (1995) 17431–17438. https://doi.org/10.1103/PhysRevB.51.17431.

[84] G. Ghosh, First-principles calculations of structural energetics of Cu–TM (TM=Ti, Zr, Hf) intermetallics, Acta Mater. 55 (2007) 3347–3374. https://doi.org/10.1016/j.actamat.2007.01.037.

[85] K.J. Zeng, M. Hämäläinen, H.L. Lukas, A new thermodynamic description of the Cu-Zr system, J. Phase Equilibria 15 (1994) 577–586. https://doi.org/10.1007/BF02647618.

[86] N. Wang, C. Li, Z. Du, F. Wang, W. Zhang, The thermodynamic re-assessment of the Cu–Zr system, Calphad 30 (2006) 461–469. https://doi.org/10.1016/j.calphad.2006.06.002.

[87] N. Saunders, Phase diagram calculations for eight glass forming alloy systems, Calphad 9 (1985) 297–309. https://doi.org/10.1016/0364-5916(85)90001-X.

[88] O.J. Kleppa, S. Watanabe, Thermochemistry of alloys of transition metals: Part III. Copper-Silver, -Titanium, Zirconium, and -Hafnium at 1373 K, Metall. Trans. B 13 (1982) 391–401. https://doi.org/10.1007/BF02667755.

[89] D. Turnbull, Under what conditions can a glass be formed?, Contemp. Phys. 10 (1969) 473–488. https://doi.org/10.1080/00107516908204405.

[90] C. Suryanarayana, A. Inoue, Bulk Metallic Glasses, 2nd ed., CRC Press, Boca Raton, 2017. https://doi.org/10.1201/9781315153483.

[91] C. Suryanarayana, ed., Non-equilibrium processing of materials, 1st ed, Pergamon, Amsterdam ; New York, 1999.

[92] M. Sathish, N. Radhika, B. Saleh, Current Status, Challenges, and Future Prospects of Thin Film Coating Techniques and Coating Structures, J. Bio- Tribo-Corros. 9 (2023) 35. https://doi.org/10.1007/s40735-023-00754-9.

[93] A.S. Rajan, S. Sampath, A.K. Shukla, An in situ carbon-grafted alkaline iron electrode for iron-based accumulators, Energy Environ. Sci. 7 (2014) 1110–1116. https://doi.org/10.1039/C3EE42783H.

[94] Y. Zhang, Y. Wang, S. Wang, W. Wei, X. Ge, B. Zhu, J. Shao, Y. Wang, Comparison of Carbon Thin Films with Low Secondary Electron Yield Deposited in Neon and Argon, Coatings 10 (2020) 884. https://doi.org/10.3390/coatings10090884.

[95] Y. Wang, W. Guan, C.B. Fischer, S. Wehner, R. Dang, J. Li, C. Wang, W. Guo, Microstructures, mechanical properties and tribological behaviors of amorphous carbon coatings in-situ grown on polycarbonate surfaces, Appl. Surf. Sci. 563 (2021) 150309. https://doi.org/10.1016/j.apsusc.2021.150309.

[96] X. Wei, X. Chen, X. Ren, Q. Lu, L. Zhang, F. Wang, Polymeric amorphous carbon films with high hardness, Diam. Relat. Mater. 73 (2017) 253–259. https://doi.org/10.1016/J.DIAMOND.2016.10.005.

[97] L. Krämer, Y. Champion, R. Pippan, From powders to bulk metallic glass composites, Sci. Rep. 7 (2017) 6651. https://doi.org/10.1038/s41598-017-06424-4.

[98] J.T. Zhao, J.Y. Zhang, L.F. Cao, Y.Q. Wang, P. Zhang, K. Wu, G. Liu, J. Sun, Zr alloying effect on the microstructure evolution and plastic deformation of nanostructured Cu thin films, Acta Mater. 132 (2017) 550–564. https://doi.org/10.1016/j.actamat.2017.05.007.

[99] J. Chakraborty, T. Oellers, R. Raghavan, A. Ludwig, G. Dehm, Microstructure and residual stress evolution in nanocrystalline Cu-Zr thin films, J. Alloys Compd. 896 (2022) 162799. https://doi.org/10.1016/j.jallcom.2021.162799.

[100] A. Bagherpour, E. Haye, P. Moskovkin, S. Lucas, Vein pattern vs. columnar fracture shape in Cu-Zr thin film metallic glasses: Driving force and mechanism, Materialia (2023) 101914. https://doi.org/10.1016/j.mtla.2023.101914.

[101] P. Zeman, M. Zítek, Zuzjaková, R. Čerstvý, Amorphous Zr-Cu thin-film alloys with metallic glass behavior, J. Alloys Compd. 696 (2017) 1298–1306. https://doi.org/10.1016/j.jallcom.2016.12.098.

[102] W. Tillmann, N.F. Lopes Dias, C. Franke, D. Kokalj, D. Stangier, C.A. Thomann, J. Debus, Mechanical properties and adhesion behavior of amorphous carbon films with bias voltage controlled TixCy interlayers on Ti6Al4V, Diam. Relat. Mater. 115 (2021) 108361. https://doi.org/10.1016/j.diamond.2021.108361.

[103] E. Filova, M. Vandrovcova, M. Jelinek, J. Zemek, J. Houdkova, Jan Remsa, T. Kocourek, L. Stankova, L. Bacakova, Adhesion and differentiation of Saos-2 osteoblast-like cells on chromium-doped diamond-like carbon coatings, J. Mater. Sci. Mater. Med. 28 (2016) 17. https://doi.org/10.1007/s10856-016-5830-2.

[104] Z. Li, G. Ma, Z. Xing, Q. Yong, H. Zhao, Y. Huang, W. Guo, Z. Zhang, H. Wang, The effects of Cr and B doping on the mechanical properties and tribological behavior of multi-layered hydrogenated diamond-like carbon films, Surf. Coat. Technol. 431 (2022) 127977. https://doi.org/10.1016/j.surfcoat.2021.127977.

[105] X. Shuhua, R. Zhaoxing, Ions Bombardment in Thin Films and Surface Processing, Plasma Sci. Technol. 5 (2003) 1841. https://doi.org/10.1088/1009-0630/5/3/015.

[106] H. Zegtouf, N. Saoula, M. Azibi, L. Bait, N. Madaoui, M.R. Khelladi, M. Kechouane, Influence of substrate bias voltage on structure, mechanical and corrosion properties of ZrO2 thin films deposited by Reactive Magnetron Sputter Deposition, Surf. Coat. Technol. 393 (2020) 125821. https://doi.org/10.1016/j.surfcoat.2020.125821.

[107] N.-T. Do, V.-H. Dinh, L.V. Lich, H.-H. Dang-Thi, T.-G. Nguyen, Effects of Substrate Bias Voltage on Structure of Diamond-Like Carbon Films on AISI 316L Stainless Steel: A Molecular Dynamics Simulation Study, Materials 14 (2021) 4925. https://doi.org/10.3390/ma14174925.

[108] W. Tillmann, H. Ulitzka, N.F. Lopes Dias, D. Stangier, C.A. Thomann, H. Moldenhauer, J. Debus, Effects of acetylene flow rate and bias voltage on the structural and tribo-mechanical properties of sputtered a-C:H films, Thin Solid Films 693 (2020) 137691. https://doi.org/10.1016/j.tsf.2019.137691.

[109] M. Keunecke, K. Bewilogua, J. Becker, A. Gies, M. Grischke, CrC/a-C:H coatings for highly loaded, low friction applications under formulated oil lubrication, Surf. Coat. Technol. 207 (2012) 270–278. https://doi.org/10.1016/j.surfcoat.2012.06.085.

[110] H. Ronkainen, S. Varjus, K. Holmberg, Friction and wear properties in dry, water- and oil-lubricated DLC against alumina and DLC against steel contacts, Wear 222 (1998) 120–128. https://doi.org/10.1016/S0043-1648(98)00314-7.

[111] C. Meunier, P. Alers, L. Marot, J. Stauffer, N. Randall, S. Mikhailov, Friction properties of ta-C and a-C:H coatings under high vacuum, Surf. Coat. Technol. 200 (2005) 1976–1981. https://doi.org/10.1016/j.surfcoat.2005.08.013.

[112] Y. Xia, Y. Hirai, T. Tsuchiya, Effect of alternating a-C:H multilayer full coating on fracture behavior of single-crystal silicon-based microstructure in tensile and toughness tests, Mater. Sci. Eng. A 827 (2021) 142054. https://doi.org/10.1016/j.msea.2021.142054.

[113] Y. Xia, Y. Hirai, T. Tsuchiya, Fracture behavior of single-crystal silicon microstructure coated with stepwise bias-graded a-C:H film, Surf. Coat. Technol. 405 (2021) 126559. https://doi.org/10.1016/j.surfcoat.2020.126559.

[114] K. Jonnalagadda, S.W. Cho, I. Chasiotis, T. Friedmann, J. Sullivan, Effect of intrinsic stress gradient on the effective mode-I fracture toughness of amorphous diamond-like carbon films for MEMS, J. Mech. Phys. Solids 56 (2008) 388–401. https://doi.org/10.1016/j.jmps.2007.05.013.

[115] Z.T. Wang, K.Y. Zeng, Y. Li, The correlation between glass formation and hardness of the amorphous phase, Scr. Mater. 65 (2011) 747–750. https://doi.org/10.1016/j.scriptamat.2011.06.043.

[116] M. Abboud, A. Motallebzadeh, N. Verma, S. Özerinç, Nanoscratch Behavior of Metallic Glass/Crystalline Nanolayered Composites, Jom 71 (2019) 593–601. https://doi.org/10.1007/s11837-018-3270-9.

[117] M. Abboud, S. Özerinç, Size-independent strength of amorphous-HCP crystalline metallic nanolayers, J. Mater. Res. 34 (2019) 2275–2284. https://doi.org/10.1557/jmr.2019.74.

[118] M. Abboud, S. Özerinç, Size-independent strength of amorphous-HCP crystalline metallic nanolayers, J. Mater. Res. 34 (2019) 2275–2284. https://doi.org/10.1557/jmr.2019.74.

[119] S. Hashmi, Comprehensive Materials Processing, (n.d.) 5474.

[120] U. Jeong, J. Han, K.P. Marimuthu, Y. Lee, H. Lee, Evaluation of mechanical properties of Zr–Cu–Al–Ni TFMG using nanoindentation, J. Mater. Res. Technol. 12 (2021) 2368–2382. https://doi.org/10.1016/j.jmrt.2021.04.030.

[121] Q. Sun, D.M. Miskovic, M. Ferry, Film thickness effect on formation of ultrastable metallic glasses, Mater. Today Phys. 18 (2021) 100370. https://doi.org/10.1016/j.mtphys.2021.100370.

[122] M.C. Liu, J.C. Huang, Y.T. Fong, S.P. Ju, X.H. Du, H.J. Pei, T.G. Nieh, Assessing the interfacial strength of an amorphous-crystalline interface, Acta Mater. 61 (2013) 3304–3313. https://doi.org/10.1016/j.actamat.2013.02.019.

[123] C.-L. Li, J.P. Chu, J.-W. Lee, Measuring notch toughness of thin film metallic glasses using focused ion beam-based microcantilever method: Comparison with Ti and TiN crystalline films, Mater. Sci. Eng. A 698 (2017) 104–109. https://doi.org/10.1016/j.msea.2017.05.002.

[124] K. Hellan, H. Saunders, Introduction to Fracture Mechanics, J. Vib. Acoust. Stress Reliab. Des. 109 (1987) 325–326. https://doi.org/10.1115/1.3269443.

[125] L. Zhang, H. Yang, X. Pang, K. Gao, A.A. Volinsky, Microstructure, residual stress, and fracture of sputtered TiN films, Surf. Coat. Technol. 224 (2013) 120–125. https://doi.org/10.1016/j.surfcoat.2013.03.009.

[126] V. Schnabel, B. Nagamani Jaya, M. Köhler, D. Music, C. Kirchlechner, G. Dehm, D. Raabe, J.M. Schneider, Electronic hybridisation implications for the damage-tolerance of thin film metallic glasses metallic glass thin films, which cover the OPEN, Nat. Publ. Group (2016). https://doi.org/10.1038/srep36556.

[127] M. Ghidelli, S. Gravier, J.J. Blandin, P. Djemia, F. Mompiou, G. Abadias, J.P. Raskin, T. Pardoen, Extrinsic mechanical size effects in thin ZrNi metallic glass films, Acta Mater. 90 (2015) 232–241. https://doi.org/10.1016/j.actamat.2015.02.038.

[128] S.Y. Liu, Q.P. Cao, X. Qian, C. Wang, X.D. Wang, D.X. Zhang, X.L. Hu, W. Xu, M. Ferry, J.Z. Jiang, Effects of substrate temperature on structure, thermal stability and mechanical property of a Zr-based metallic glass thin film, Thin Solid Films 595 (2015) 17–24. https://doi.org/10.1016/j.tsf.2015.10.049.

[129] A. Jabed, M.N. Bhuiyan, W. Haider, I. Shabib, Distinctive Features and Fabrication Routes of Metallic-Glass Systems Designed for Different Engineering Applications: A Review, Coatings 13 (2023) 1689. https://doi.org/10.3390/coatings13101689.

[130] W.E.S.S. Viana, A.E. Elzubair, M.M. Wysard, D.F. Franceschini, S.S. Camargo, Comparison of the properties of a-C:H films deposited from methane and heptane precursors: study of the mechanical, chemical and structural properties, Thin Solid Films 695 (2020) 137733. https://doi.org/10.1016/j.tsf.2019.137733.

[131] X. Wang, X. Sui, S. Zhang, M. Yan, J. Yang, J. Hao, W. Liu, Effect of deposition pressures on uniformity, mechanical and tribological properties of thick DLC coatings inside of a long pipe prepared by PECVD method, Surf. Coat. Technol. 375 (2019) 150–157. https://doi.org/10.1016/j.surfcoat.2019.07.030.

[132] L. Xiao, Y. Yan, S. Yang, Uniformity improvement of a-C: H films prepared by PECVD, in: 2015 China Semicond. Technol. Int. Conf., 2015: pp. 1–3. https://doi.org/10.1109/CSTIC.2015.7153412.

[133] S.Y. Choi, T.K. Won, J.M. White, Method of improving the uniformity of PECVD-deposited thin films, US7754294B2, 2010. https://patents.google.com/patent/US7754294B2/en (accessed October 13, 2023).

[134] R. Snyders, D. Hegemann, D. Thiry, O. Zabeida, J. Klemberg-Sapieha, L. Martinu, Foundations of plasma enhanced chemical vapor deposition of functional coatings, Plasma Sources Sci. Technol. 32 (2023) 074001. https://doi.org/10.1088/1361-6595/acdabc.

[135] X. Zhou, I. Toda, K. Komatsu, H. Muramatsu, S. Ohshio, H. Saitoh, Amorphous Hydrogenated Carbon Films Deposited with Benzene by Plasma Enhanced Chemical Vapor Deposition, (2014).

[136] H. Luo, H. Sun, F. Gao, A. Billard, Mechanical properties, thermal stability and oxidation resistance of HfC/a-C:H films deposited by HiPIMS, J. Alloys Compd. 847 (2020) 156538. https://doi.org/10.1016/j.jallcom.2020.156538.

[137] A. Alamgir, A. Bogatov, T. Jõgiaas, M. Viljus, T. Raadik, J. Kübarsepp, F. Sergejev, A. Lümkemann, J. Kluson, V. Podgursky, High-Temperature Oxidation Resistance and Tribological Properties of Al2O3/ta-C Coating, Coatings 12 (2022) 547. https://doi.org/10.3390/coatings12040547.

[138] H.W. Yoon, H.C. Lee, S.Y. Shin, S.H. Kwon, K.I. Moon, Preparation of Zr-Al-Mo-Cu Single Targets with Glass Forming Ability and Deposition of Thin Film Metallic Glass, Coatings 10 (2020) 398. https://doi.org/10.3390/coatings10040398.

[139] J.-F. Tang, P.-Y. Huang, J.-H. Lin, T.-W. Liu, F.-C. Yang, C.-L. Chang, Microstructure and Antimicrobial Properties of Zr-Cu-Ti Thin-Film Metallic Glass Deposited Using High-Power Impulse Magnetron Sputtering, Materials 15 (2022) 2461. https://doi.org/10.3390/ma15072461.

[140] J. Antonowicz, P. Zalden, K. Sokolowski-Tinten, K. Georgarakis, R. Minikayev, A. Pietnoczka, F. Bertram, M. Chaika, M. Chojnacki, P. Dłużewski, K. Fronc, A.L. Greer, C. Jastrzębski, D. Klinger, Ch. Lemke, O.M. Magnussen, B. Murphy, K. Perumal, U. Ruett, J. Warias, R. Sobierajski, Devitrification of thin film Cu–Zr metallic glass via ultrashort pulsed laser annealing, J. Alloys Compd. 887 (2021) 161437. https://doi.org/10.1016/j.jallcom.2021.161437.

[141] J.Y. Zhang, Z.Q. Zhou, Z.B. Zhang, M.H. Park, Q. Yu, Z. Li, J. Ma, A.D. Wang, H.G. Huang, M. Song, B.S. Guo, Q. Wang, Y. Yang, Recent development of chemically complex metallic glasses: from accelerated compositional design, additive manufacturing to novel applications, Mater. Futur. 1 (2022) 012001. https://doi.org/10.1088/2752-5724/ac4558.

[142] L. Chen, Y. Yang, G. Wang, Y. Wang, S.O. Adede, M. Zhang, C. Jiao, D. Wang, D. Yan, Y. Liu, D. Chen, W. Wang, Design and Fabrication of a Sandwichlike Zn/Cu/Al–Zr Coating for Superior Anticorrosive Protection Performance of ZM5 Mg Alloy, ACS Appl. Mater. Interfaces 13 (2021) 41120–41130. https://doi.org/10.1021/acsami.1c11920.

[143] M. Nabizadeh, K. Marcoen, E.A. Mernissi Cherigui, T. Kolberg, D. Schatz, H. Terryn, T. Hauffman, Unraveling the formation mechanism of hybrid Zr conversion coating on advanced high strength stainless steels, Surf. Coat. Technol. 441 (2022) 128567. https://doi.org/10.1016/j.surfcoat.2022.128567.

[144] J.D. Castro, M.J. Lima, S. Carvalho, Corrosion resistance of Cu-Zr(O) N films in a simulated seawater environment, Surf. Coat. Technol. 451 (2022) 129050. https://doi.org/10.1016/j.surfcoat.2022.129050.

[145] K. Chen, D. Seo, S.H. Lee, E. Byon, A physics-based model of temperature-exposure-dependent interfacial fracture toughness of thermal barrier coatings, J. Phys. Commun. 2 (2018) 125005. https://doi.org/10.1088/2399-6528/aaf602.

[146] M.V. Tavares da Costa, E.K. Gamstedt, Energy-release rates and opening of cracks in thin barrier coatings on polymer substrates subjected to tensile loading, Eng. Fract. Mech. 235 (2020) 107151. https://doi.org/10.1016/j.engfracmech.2020.107151.

[147] M.F. Ashby, Materials selection in mechanical design, 4th ed, Butterworth-Heinemann, Burlington, MA, 2011.

[148] R. Treml, D. Kozic, R. Schöngrundner, O. Kolednik, H.-P. Gänser, R. Brunner, D. Kiener, Miniaturized fracture experiments to determine the toughness of individual films in a multilayer system, Extreme Mech. Lett. 8 (2016) 235–244. https://doi.org/10.1016/j.eml.2016.01.004.

[149] L.W. Yang, C.R. Mayer, N. Chawla, J. LLorca, J.M. Molina-Aldareguía, Nanomechanical characterization of the fracture toughness of Al/SiC nanolaminates, Extreme Mech. Lett. 40 (2020) 100945. https://doi.org/10.1016/j.eml.2020.100945.

[150] G. Triani, J.A. Campbell, P.J. Evans, J. Davis, B.A. Latella, R.P. Burford, Low temperature atomic layer deposition of titania thin films, Thin Solid Films 518 (2010) 3182–3189. https://doi.org/10.1016/j.tsf.2009.09.010.

[151] H. Hirakata, O. Nishijima, N. Fukuhara, T. Kondo, A. Yonezu, K. Minoshima, Size effect on fracture toughness of freestanding copper nano-films, Mater. Sci. Eng. A 528 (2011) 8120–8127. https://doi.org/10.1016/j.msea.2011.07.071.

[152] J.M. Jungk, B.L. Boyce, T.E. Buchheit, T.A. Friedmann, D. Yang, W.W. Gerberich, Indentation fracture toughness and acoustic energy release in tetrahedral amorphous carbon diamond-like thin films, Acta Mater. 54 (2006) 4043–4052. https://doi.org/10.1016/j.actamat.2006.05.003.

[153] B. Merle, M. Göken, Fracture toughness of silicon nitride thin films of different thicknesses as measured by bulge tests, Acta Mater. 59 (2011) 1772–1779. https://doi.org/10.1016/j.actamat.2010.11.043.

[154] Y. Hu, J.-H. Huang, J.-M. Zuo, In situ characterization of fracture toughness and dynamics of nanocrystalline titanium nitride films, J. Mater. Res. 31 (2016) 370–379. https://doi.org/10.1557/jmr.2016.4.

[155] I. Chasiotis, S.W. Cho, K. Jonnalagadda, Fracture Toughness and Subcritical Crack Growth in Polycrystalline Silicon, J. Appl. Mech. 73 (2005) 714–722. https://doi.org/10.1115/1.2172268.

[156] V. Hatty, H. Kahn, A.H. Heuer, Fracture Toughness , Fracture Strength , and Stress Corrosion Cracking of Silicon Dioxide Thin Films, 17 (2008) 943–947.

[157] S.Z. Han, J. Kang, S.-D. Kim, S.-Y. Choi, H.G. Kim, J. Lee, K. Kim, S.H. Lim, B. Han, Reliable and cost effective design of intermetallic Ni2Si nanowires and direct characterization of its mechanical properties, Sci. Rep. 5 (2015) 15050. https://doi.org/10.1038/srep15050.

[158] A. Karimi, Y. Wang, T. Cselle, M. Morstein, Fracture mechanisms in nanoscale layered hard thin films, Thin Solid Films 420–421 (2002) 275–280. https://doi.org/10.1016/S0040-6090(02)00944-6.

[159] S. Massl, W. Thomma, J. Keckes, R. Pippan, Investigation of fracture properties of magnetron-sputtered TiN films by means of a FIB-based cantilever bending technique, Acta Mater. 57 (2009) 1768–1776. https://doi.org/10.1016/j.actamat.2008.12.018.

[160] S. Frank, U.A. Handge, S. Olliges, R. Spolenak, The relationship between thin film fragmentation and buckle formation: Synchrotron-based in situ studies and two-dimensional stress analysis, Acta Mater. 57 (2009) 1442–1453. https://doi.org/10.1016/j.actamat.2008.11.023.

[161] M. Nasim, Y. Li, C. Wen, Length-scale dependent deformation, strengthening, and ductility of fcc/fcc Ni/Al nanolaminates using micropillar compression testing, Acta Mater. 193 (2020) 318–328. https://doi.org/10.1016/j.actamat.2020.04.043.

[162] Z. Liu, M.A. Monclús, L.W. Yang, M. Castillo-Rodríguez, J.M. Molina-Aldareguía, J. LLorca, Tensile deformation and fracture mechanisms of Cu/Nb nanolaminates studied by in situ TEM mechanical tests, Extreme Mech. Lett. 25 (2018) 60–65. https://doi.org/10.1016/j.eml.2018.10.007.

[163] A.S. Grenadyorov, A.A. Solovyev, K.V. Oskomov, V.S. Sypchenko, Thermal stability of a-C:H:SiOx thin films in hydrogen atmosphere, Thin Solid Films 690 (2019) 137531. https://doi.org/10.1016/j.tsf.2019.137531.

[164] Y. Ma, H. Chen, H. Li, S. Dang, Influence Mechanism of Ageing Parameters of Cu-Cr-Zr Alloy on Its Structure and Properties, Materials 15 (2022) 7605. https://doi.org/10.3390/ma15217605.

[165] J. Hu, Y. Tian, H. Yu, G. Ling, S. Li, M. Jiang, H. Li, G. Qin, Optimizing strength and electrical conductivity of Cu-Cr-Zr alloy by two-stage aging treatment, Mater. Lett. 315 (2022) 131937. https://doi.org/10.1016/j.matlet.2022.131937.

[166] D.J. Morgan, Imaging XPS for industrial applications, J. Electron Spectrosc. Relat. Phenom. 231 (2019) 109–117. https://doi.org/10.1016/j.elspec.2017.12.008.

[167] N.M. Forsyth, P. Coxon, Use of parallel imaging XPS to perform rapid analysis of polymer surfaces with spatial resolution >5 µm, Surf. Interface Anal. 21 (1994) 430–434. https://doi.org/10.1002/sia.740210619.

[168] U. Vohrer, C. Blomfield, S. Page, A. Roberts, Quantitative XPS imaging—new possibilities with the delay-line detector, Appl. Surf. Sci. 252 (2005) 61–65. https://doi.org/10.1016/j.apsusc.2005.01.114.

[169] J. Végh, The Shirley background revised, J. Electron Spectrosc. Relat. Phenom. 151 (2006) 159–164. https://doi.org/10.1016/j.elspec.2005.12.002.

[170] W.C. Oliver, G.M. Pharr, An improved technique for determining hardness and elastic modulus using load and displacement sensing indentation experiments, J. Mater. Res. 7 (1992) 1564–1583. https://doi.org/10.1557/JMR.1992.1564.

[171] J. Hay, B. Crawford, Measuring substrate-independent modulus of thin films, J. Mater. Res. 26 (2011) 727–738. https://doi.org/10.1557/jmr.2011.8.

[172] C.D. Gu, J.S. Lian, Q. Jiang, W.T. Zheng, Experimental and modelling investigations on strain rate sensitivity of an electrodeposited 20 nm grain sized Ni, J. Phys. Appl. Phys. 40 (2007) 7440–7446. https://doi.org/10.1088/0022-3727/40/23/027.

[173] P. Baral, G. Guillonneau, G. Kermouche, J.M. Bergheau, J.L. Loubet, A new long-term indentation relaxation method to measure creep properties at the micro-scale with application to fused silica and PMMA, Mech. Mater. 137 (2019) 103095. https://doi.org/10.1016/j.mechmat.2019.103095.

[174] P. Baral, A. Orekhov, R. Dohmen, M. Coulombier, J.P. Raskin, P. Cordier, H. Idrissi, T. Pardoen, Rheology of amorphous olivine thin films characterized by nanoindentation, Acta Mater. 219 (2021) 117257. https://doi.org/10.1016/j.actamat.2021.117257.

[175] K. Kim, H. Luo, A.K. Singh, T. Zhu, S. Graham, O.N. Pierron, Environmentally Assisted Cracking in Silicon Nitride Barrier Films on Poly(ethylene terephthalate) Substrates, ACS Appl. Mater. Interfaces 8 (2016) 27169–27178. https://doi.org/10.1021/acsami.6b06417.

[176] J. Dundurs, Edge-bonded dissimilar orthogonal elastic wedges under normal and shear loading, J. Appl. Mech. Trans. ASME 36 (1964) 650–651. https://doi.org/10.1115/1.3564739.

[177] R. Huang, J.H. Prévost, Z.Y. Huang, Z. Suo, Channel-cracking of thin films with the extended finite element method, Eng. Fract. Mech. 70 (2003) 2513–2526. https://doi.org/10.1016/S0013-7944(03)00083-3.

[178] K. Fu, L. Chang, B. Zheng, Y. Tang, Y. Yin, Analysis on cracking in hard thin films on a soft substrate under Berkovich indentation, Vacuum 112 (2015) 29–32. https://doi.org/10.1016/j.vacuum.2014.11.013.

[179] W. Zhao, Y. Li, S. Wang, X. He, Y. Shang, Q. Peng, C. Wang, S. Du, X. Gui, Y. Yang, Q. Yuan, E. Shi, S. Wu, W. Xu, A. Cao, Elastic improvement of carbon nanotube sponges by depositing amorphous carbon coating, Carbon 76 (2014) 19–26. https://doi.org/10.1016/j.carbon.2014.04.032.

[180] M.F. Ashby, A.L. Greer, Metallic glasses as structural materials, Scr. Mater. 54 (2006) 321–326. https://doi.org/10.1016/J.SCRIPTAMAT.2005.09.051.

[181] C.P.O. Treutler, Industrial use of plasma-deposited coatings for components of automotive fuel injection systems, Surf. Coat. Technol. 200 (2005) 1969–1975. https://doi.org/10.1016/J.SURFCOAT.2005.08.012.

[182] W. Tillmann, N.F. Lopes Dias, D. Stangier, C. Schaak, S. Höges, Heat treatment of binder jet printed 17–4 PH stainless steel for subsequent deposition of tribo-functional diamond-like carbon coatings, Mater. Des. 213 (2022) 110304. https://doi.org/10.1016/j.matdes.2021.110304.

[183] V. Job, J. Laloy, V. Maloteau, E. Haye, S. Lucas, S. Penninckx, Investigation of the Antibacterial Properties of Silver-Doped Amorphous Carbon Coatings Produced by Low Pressure Magnetron Assisted Acetylene Discharges, Int. J. Mol. Sci. 23 (2022) 563. https://doi.org/10.3390/ijms23010563.

[184] J. Zhang, B. Zhang, Q. Xue, Z. Wang, Ultra-elastic recovery and low friction of amorphous carbon films produced by a dispersion of multilayer graphene, Diam. Relat. Mater. 23 (2012) 5–9. https://doi.org/10.1016/j.diamond.2011.12.011.

[185] A. Vanhulsel, F. Velasco, R. Jacobs, L. Eersels, D. Havermans, E.W. Roberts, I. Sherrington, M.J. Anderson, L. Gaillard, DLC solid lubricant coatings on ball bearings for space applications, Tribol. Int. 40 (2007) 1186–1194. https://doi.org/10.1016/j.triboint.2006.12.005.

[186] D. Thiry, A. De Vreese, F. Renaux, J.L. Colaux, S. Lucas, Y. Guinet, L. Paccou, E. Bousser, R. Snyders, Toward a Better Understanding of the Influence of the Hydrocarbon Precursor on the Mechanical Properties of a-C:H Coatings Synthesized by a Hybrid PECVD/PVD Method, Plasma Process. Polym. 13 (2016) 316–323. https://doi.org/10.1002/ppap.201500050.

[187] A. Michelmore, J.D. Whittle, R.D. Short, The importance of ions in low pressure PECVD plasmas, Front. Phys. 3 (2015) 3. https://doi.org/10.3389/fphy.2015.00003.

[188] F.F. Conde, J.A. ávila Diaz, G.F. Da Silva, A.P. Tschiptschin, Dependence of wear and mechanical behavior of nitrocarburized/Crn/Dlc layer on film thickness, Mater. Res. 22 (2019). https://doi.org/10.1590/1980-5373-MR-2018-0499.

[189] N.T. Panagiotopoulos, G. Karras, E. Lidorikis, D.C. Koutsogeorgis, C. Kosmidis, P. Patsalas, Photosensitivity and optical performance of hydrogenated amorphous carbon films processed by picosecond laser beams, Surf. Coat. Technol. 206 (2011) 734–741. https://doi.org/10.1016/J.SURFCOAT.2011.02.019.

[190] Y. Tachimoto, M. Noborisaka, A. Shirakura, C. Kuroyanagi, T. Suzuki, Gas Barrier Properties of Diamond-like Carbon Films Synthesized by Using Remote Type Microwave Plasma CVD under Sub-ambient Atmospheric Pressure, J. Phys. Conf. Ser. 417 (2013) 012043. https://doi.org/10.1088/1742-6596/417/1/012043.

[191] S. Tamulevičius, Š. Meškinis, T. Tamulevičius, H.-G. Rubahn, Diamond like carbon nanocomposites with embedded metallic nanoparticles, Rep. Prog. Phys. 81 (2018) 024501. https://doi.org/10.1088/1361-6633/AA966F.

[192] A.C. Popescu, G.E. Stan, L. Duta, C. Nita, C. Popescu, V.-A. Surdu, M.-A. Husanu, B. Bita, R. Ghisleni, C. Himcinschi, V. Craciun, The Role of Ambient Gas and Pressure on the Structuring of Hard Diamond-Like Carbon Films Synthesized by Pulsed Laser Deposition, Mater. 2015 Vol 8 Pages 3284-3305 8 (2015) 3284–3305. https://doi.org/10.3390/MA8063284.

[193] A.W. Zia, Z. Zhou, L.K.-Y. Li, Structural, mechanical, and tribological characteristics of diamond-like carbon coatings, in: Nanomater.-Based Coat., Elsevier, 2019: pp. 171–194. https://doi.org/10.1016/B978-0-12-815884-5.00007-7.

[194] M. Zawischa, V. Weihnacht, J. Kaspar, M. Zimmermann, Effect of doping elements to hydrogen-free amorphous carbon coatings on structure and mechanical properties with special focus on crack resistance, Mater. Sci. Eng. A 857 (2022) 144086. https://doi.org/10.1016/j.msea.2022.144086.

[195] V. Singh, J.C. Jiang, E.I. Meletis, Cr-diamondlike carbon nanocomposite films: Synthesis, characterization and properties, Thin Solid Films 489 (2005) 150–158. https://doi.org/10.1016/J.TSF.2005.04.104.

[196] W. Dai, G. Wu, A. Wang, Structure and elastic recovery of Cr–C:H films deposited by a reactive magnetron sputtering technique, Appl. Surf. Sci. 257 (2010) 244–248. https://doi.org/10.1016/J.APSUSC.2010.06.076.

[197] C.A. Schuh, Nanoindentation studies of materials, Mater. Today 9 (2006) 32–40. https://doi.org/10.1016/S1369-7021(06)71495-X.

[198] A. Leyland, A. Matthews, On the significance of the H/E ratio in wear control: A nanocomposite coating approach to optimised tribological behaviour, Wear 246 (2000) 1–11. https://doi.org/10.1016/S0043-1648(00)00488-9.

[199] A. Fauroux, C. Vandenabeele, A. Pflug, S. Lucas, Experimental and theoretical study of a magnetron DC-PECVD acetylene discharge: Determination of the main species and reactions taking place in the plasma, Surf. Coat. Technol. 400 (2020) 126195. https://doi.org/10.1016/j.surfcoat.2020.126195.

[200] A. Fauroux, A. Pflug, S. Lucas, Experimental and theoretical study of a magnetron DC-PECVD acetylene discharge: Identification of the deposition precursors and film growth mechanisms, Surf. Coat. Technol. 421 (2021) 127472. https://doi.org/10.1016/j.surfcoat.2021.127472.

[201] S. Lucas, E. HAYE, J.-J. Pireaux, Tunable multifunctional carbon-based coatings, WO2022084519A1, 2022. https://patents.google.com/patent/WO2022084519A1/en (accessed August 18, 2022).

[202] C. Lopez-Santos, J.L. Colaux, J.C. Gonzalez, S. Lucas, Investigation of the Growth Mechanisms of a-CHx Coatings Deposited by Pulsed Reactive Magnetron Sputtering, J. Phys. Chem. C 116 (2012) 12017–12026. https://doi.org/10.1021/jp300697s.

[203] W. Dai, H. Zheng, G. Wu, A. Wang, Effect of bias voltage on growth property of Cr-DLC film prepared by linear ion beam deposition technique, Vacuum 85 (2010) 231–235. https://doi.org/10.1016/J.VACUUM.2010.06.001.

[204] L. Wang, L. Li, X. Kuang, Effect of substrate bias on microstructure and mechanical properties of WC-DLC coatings deposited by HiPIMS, Surf. Coat. Technol. 352 (2018) 33–41. https://doi.org/10.1016/j.surfcoat.2018.07.088.

[205] G. Zhou, L. Wang, X. Wang, Y. Yu, A. Mutzke, Effect of bias voltage on microstructure and optical properties of Al2O3 thin films prepared by twin targets reactive high power impulse magnetron sputtering, Vacuum 166 (2019) 88–96. https://doi.org/10.1016/j.vacuum.2019.04.060.

[206] Z. Shi, P. Shum, Z. Zhou, L.K.-Y. Li, Effect of bias voltage on the properties of CeO2−x coatings prepared by magnetron sputtering, Surf. Coat. Technol. 326 (2017) 411–416. https://doi.org/10.1016/j.surfcoat.2016.11.104.

[207] M. Rohrbeck, S. Körsten, C.B. Fischer, S. Wehner, B. Kessler, Diamond-like carbon coating of a pure bioplastic foil, Thin Solid Films 545 (2013) 558–563. https://doi.org/10.1016/j.tsf.2013.07.028.

[208] G. Kermouche, J.L. Loubet, J.M. Bergheau, Extraction of stress–strain curves of elastic–viscoplastic solids using conical/pyramidal indentation testing with application to polymers, Mech. Mater. 40 (2008) 271–283. https://doi.org/10.1016/j.mechmat.2007.08.003.

[209] A. van der Rest, H. Idrissi, F. Henry, A. Favache, D. Schryvers, J. Proost, J.-P. Raskin, Q. Van Overmeere, T. Pardoen, Mechanical behavior of ultrathin sputter deposited porous amorphous Al2O3 films, Acta Mater. 125 (2017) 27–37. https://doi.org/10.1016/j.actamat.2016.11.037.

[210] A.S. Argon, Inelastic behavior of non-polymeric glasses, Phys. Deform. Fract. Polym. (2013) 174–227. https://doi.org/10.1017/CBO9781139033046.009.

[211] X. Geng, Z. Zhang, E. Barthel, D. Dalmas, Mechanical behavior of stiff coating on glass under sliding contact, Wear 269 (2010) 351–361. https://doi.org/10.1016/j.wear.2010.04.016.

[212] S.N. Kassavetis, S. Logothetidis, G.M. Matenoglou, Near-surface mechanical properties and surface morphology of hydrogenated amorphous carbon thin films, (2005). https://doi.org/10.1016/j.surfcoat.2005.11.010.

[213] P.V. Brande, S. Lucas, R. Winand, A. Weymeersch, L. Renard, Determination of the chemical and physical properties of hydrogenated carbon deposits produced by d.c. magnetron reactive sputtering, Surf. Coat. Technol. 68–69 (1994) 656–661. https://doi.org/10.1016/0257-8972(94)90233-X.

[214] V. De Vriendt, F. Maseri, A. Nonet, S. Lucas, Study of Nanoparticles Formation in a Pulsed Magnetron Discharge in Acetylene, Plasma Process. Polym. 6 (2009) S6–S10. https://doi.org/10.1002/ppap.200930105.

[215] V. De Vriendt, S.M. Miladinovic, J.L. Colaux, F. Maseri, C.L. Wilkins, S. Lucas, Growth Mechanisms Involved in the Synthesis of Smooth and Microtextured Films by Acetylene Magnetron Discharges, Langmuir 27 (2011) 8913–8922. https://doi.org/10.1021/la2003035.

[216] J.P. Wang, L.P. Tan, T.Y.F. Liew, T.S. Low, H.L. Wong, Y.K. Lee, Effects of DC Bias on the Thermal Stability of DC In-Line Sputtered CoCrTa/Cr Thin Film Media, MRS Proc. 517 (1998) 273. https://doi.org/10.1557/PROC-517-273.

[217] W.A. Harrison, Electronic Structure and the Properties of Solids: The Physics of the Chemical Bond, Courier Corporation, 2012.

[218] B. Bhushan, Chemical, mechanical and tribological characterization of ultra-thin and hard amorphous carbon coatings as thin as 3.5 nm: Recent developments, Diam. Relat. Mater. 8 (1999) 1985–2015. https://doi.org/10.1016/S0925-9635(99)00158-2.

[219] W. Dai, Y. Shi, Effect of Bias Voltage on Microstructure and Properties of Tantalum Nitride Coatings Deposited by RF Magnetron Sputtering, Coat. 2021 Vol 11 Page 911 11 (2021) 911. https://doi.org/10.3390/COATINGS11080911.

[220] X. Lu, M. Li, X. Tang, J. Lee, Micromechanical properties of hydrogenated diamond-like carbon multilayers, Surf. Coat. Technol. 201 (2006) 1679–1684. https://doi.org/10.1016/j.surfcoat.2006.02.052.

[221] M. Constantinou, P. Nikolaou, L. Koutsokeras, A. Avgeropoulos, D. Moschovas, C. Varotsis, P. Patsalas, P. Kelires, G. Constantinides, Metal (Ag/Ti)-Containing Hydrogenated Amorphous Carbon Nanocomposite Films with Enhanced Nanoscratch Resistance: Hybrid PECVD/PVD System and Microstructural Characteristics, Nanomaterials 8 (2018) 209. https://doi.org/10.3390/nano8040209.

[222] S. Nißen, J. Heeg, M. Wienecke, D. Behrend, M. Warkentin, Enhancing adhesion strength of a-C:H:Cu composite coatings on Ti6Al4V by graded copper deposition in a rf-PVD/PECVD hybrid process, Surf. Coat. Technol. 350 (2018) 659–671. https://doi.org/10.1016/j.surfcoat.2018.07.023.

[223] B.D. Beake, T.W. Liskiewicz, V.M. Vishnyakov, M.I. Davies, Development of DLC coating architectures for demanding functional surface applications through nano- and micro-mechanical testing, Surf. Coat. Technol. 284 (2015) 334–343. https://doi.org/10.1016/j.surfcoat.2015.05.050.

[224] P. Lemoine, J.P. Quinn, P. Maguire, J.A. McLaughlin, Comparing hardness and wear data for tetrahedral amorphous carbon and hydrogenated amorphous carbon thin films, Wear 257 (2004) 509–522. https://doi.org/10.1016/j.wear.2004.01.010.

[225] Q. Chen, C. Zeng, M. Xu, H. Yuan, H. Lv, Z. Wang, X. Wang, Effect of SiNx interlayer thickness on adhesion and friction properties of diamond-like carbon films, Diam. Relat. Mater. 94 (2019) 186–193. https://doi.org/10.1016/j.diamond.2019.01.024.

[226] B.D. Beake, S.P. Lau, Nanotribological and nanomechanical properties of 5–80 nm tetrahedral amorphous carbon films on silicon, Diam. Relat. Mater. 14 (2005) 1535–1542. https://doi.org/10.1016/j.diamond.2005.04.002.

[227] B.D. Beake, S.R. Goodes, B. Shi, Nanomechanical and nanotribological testing of ultra-thin carbon-based and MoST films for increased MEMS durability, J. Phys. Appl. Phys. 42 (2009) 065301. https://doi.org/10.1088/0022-3727/42/6/065301.

[228] H. Idrissi, M. Ghidelli, A. Béché, S. Turner, S. Gravier, J.-J. Blandin, J.-P. Raskin, D. Schryvers, T. Pardoen, Atomic-scale viscoplasticity mechanisms revealed in high ductility metallic glass films, Sci. Rep. 9 (2019) 13426. https://doi.org/10.1038/s41598-019-49910-7.

[229] F. Bignoli, S. Rashid, E. Rossi, S. Jaddi, P. Djemia, G. Terraneo, A. Li Bassi, H. Idrissi, T. Pardoen, M. Sebastiani, M. Ghidelli, Effect of annealing on mechanical properties and thermal stability of ZrCu/O nanocomposite amorphous films synthetized by pulsed laser deposition, Mater. Des. 221 (2022) 110972. https://doi.org/10.1016/j.matdes.2022.110972.

[230] Y.X. Wang, S. Zhang, J.W. Lee, W.S. Lew, B. Li, Influence of bias voltage on the hardness and toughness of CrAlN coatings via magnetron sputtering, Surf. Coat. Technol. 206 (2012) 5103–5107. https://doi.org/10.1016/J.SURFCOAT.2012.06.041.

[231] E. Preiß, Fracture toughness of freestanding metallic thin films studied by bulge testing: = Charakterisierung der Bruchzähigkeit freistehender metallischer Dünnschichten mittels Bulge-Experimenten, FAU University Press, Erlangen, 2018.

[232] J.M. Gentile, D.D. Stauffer, D.C. Hofmann, J.R. Trelewicz, Shear localization and its dependence on microstructural length scales in metallic glass composites, Materialia 9 (2020) 100598. https://doi.org/10.1016/j.mtla.2020.100598.

[233] X.D. Wang, R.T. Qu, S.J. Wu, Z.W. Zhu, H.F. Zhang, Z.F. Zhang, Improving fatigue property of metallic glass by tailoring the microstructure to suppress shear band formation, Materialia 7 (2019) 100407. https://doi.org/10.1016/j.mtla.2019.100407.

[234] J.J. Lewandowski, A.L. Greer, Temperature rise at shear bands in metallic glasses, Nat. Mater. 5 (2006) 15–18. https://doi.org/10.1038/nmat1536.

[235] W.J. Wright, R.B. Schwarz, W.D. Nix, Localized heating during serrated plastic flow in bulk metallic glasses, Mater. Sci. Eng. A 319–321 (2001) 229–232. https://doi.org/10.1016/S0921-5093(01)01066-8.

[236] D.P. Wang, H.T. Zhang, P.Y. Guo, B.A. Sun, Y.X. Wang, Nanoscale periodic distribution of energy dissipation at the shear band plane in a Zr-based metallic glass, Scr. Mater. 197 (2021) 113784. https://doi.org/10.1016/j.scriptamat.2021.113784.

[237] C. Tang, J. Yi, W. Xu, M. Ferry, Temperature rise in shear bands in a simulated metallic glass, Phys. Rev. B 98 (2018) 224203. https://doi.org/10.1103/PhysRevB.98.224203.

[238] B. Yang, M.L. Morrison, P.K. Liaw, R.A. Buchanan, G. Wang, C.T. Liu, M. Denda, Dynamic evolution of nanoscale shear bands in a bulk-metallic glass, Appl. Phys. Lett. 86 (2005) 141904. https://doi.org/10.1063/1.1891302.

[239] A. Das, P. Kagebein, S. Küchemann, R. Maaß, Temperature rise from fracture in a Zr-based metallic glass, Appl. Phys. Lett. 112 (2018) 261905. https://doi.org/10.1063/1.5034762.

[240] B. Shi, Y. Xu, P. Jin, A way by inhomogeneous plastic deformation of metallic glasses to synthesize metallic nanoglasses: A brief review, Materialia 7 (2019) 100390. https://doi.org/10.1016/j.mtla.2019.100390.

[241] M. Malekan, R. Rashidi, M. Bozorg, N. Birbilis, Tailoring the glass forming ability, mechanical properties and corrosion resistance of Cu–Zr–Al bulk metallic glasses by yttrium addition, Intermetallics 158 (2023) 107906. https://doi.org/10.1016/j.intermet.2023.107906.

[242] A. Etiemble, C. Der Loughian, M. Apreutesei, C. Langlois, S. Cardinal, J.M. Pelletier, J.-F. Pierson, P. Steyer, Innovative Zr-Cu-Ag thin film metallic glass deposed by magnetron PVD sputtering for antibacterial applications, J. Alloys Compd. 707 (2017) 155–161. https://doi.org/10.1016/j.jallcom.2016.12.259.

[243] S. Comby-Dassonneville, T. Venot, A. Borroto, E. Longin, C. der Loughian, B. ter Ovanessian, M.-A. Leroy, J.-F. Pierson, P. Steyer, ZrCuAg Thin-Film Metallic Glasses: Toward Biostatic Durable Advanced Surfaces, ACS Appl. Mater. Interfaces 13 (2021) 17062–17074. https://doi.org/10.1021/acsami.1c01127.

[244] B.A. Sun, J. Tan, S. Pauly, U. Kühn, J. Eckert, Stable fracture of a malleable Zr-based bulk metallic glass, J. Appl. Phys. 112 (2012) 103533. https://doi.org/10.1063/1.4767327.

[245] A. Sharma, M. Zadorozhnyy, A. Stepashkin, A. Kvaratskheliya, A. Korol, D. Moskovskikh, S. Kaloshkin, V. Zadorozhnyy, Investigation of Thermophysical Properties of Zr-Based Metallic Glass-Polymer Composite, Metals 11 (2021) 1412. https://doi.org/10.3390/met11091412.

[246] A.-L. Thomann, A. Caillard, M. Raza, M. El Mokh, P.A. Cormier, S. Konstantinidis, Energy flux measurements during magnetron sputter deposition processes, Surf. Coat. Technol. 377 (2019) 124887. https://doi.org/10.1016/j.surfcoat.2019.08.016.

[247] J.T. Gudmundsson, Physics and technology of magnetron sputtering discharges, Plasma Sources Sci. Technol. 29 (2020) 113001. https://doi.org/10.1088/1361-6595/abb7bd.

[248] S.K. Deb Nath, Thermal conductivity and mechanical properties of ZrxCu90−xAl10 under tension using molecular dynamics simulations, Int. J. Mech. Sci. 144 (2018) 836–841. https://doi.org/10.1016/j.ijmecsci.2017.08.037.

[249] R.T. Qu, S.G. Wang, G.J. Li, R.F. Wang, X.D. Wang, S.J. Wu, Z.F. Zhang, Shear band fracture in metallic glass: Hot or cold?, Scr. Mater. 162 (2019) 136–140. https://doi.org/10.1016/j.scriptamat.2018.11.003.

[250] S.H. Nandam, Y. Ivanisenko, R. Schwaiger, Z. Śniadecki, X. Mu, D. Wang, R. Chellali, T. Boll, A. Kilmametov, T. Bergfeldt, H. Gleiter, H. Hahn, Cu-Zr nanoglasses: Atomic structure, thermal stability and indentation properties, Acta Mater. 136 (2017) 181–189. https://doi.org/10.1016/j.actamat.2017.07.001.

[251] C.R. Cao, D.W. Ding, D.Q. Zhao, E. Axinte, H.Y. Bai, W.H. Wang, Correlation between glass transition temperature and melting temperature in metallic glasses, Mater. Des. 60 (2014) 576–579. https://doi.org/10.1016/j.matdes.2014.04.021.

[252] Y. Ohishi, K. Kurokawa, Y. Sun, H. Muta, Thermophysical properties of molten Zr1−xOx (x=0.1, 0.2) measured by electrostatic levitation, J. Nucl. Mater. 528 (2020) 151873. https://doi.org/10.1016/j.jnucmat.2019.151873.

[253] G. Abadias, E. Chason, J. Keckes, M. Sebastiani, G.B. Thompson, E. Barthel, G.L. Doll, C.E. Murray, C.H. Stoessel, L. Martinu, Review Article: Stress in thin films and coatings: Current status, challenges, and prospects, J. Vac. Sci. Technol. Vac. Surf. Films 36 (2018) 020801. https://doi.org/10.1116/1.5011790.

[254] D.R. Lide, CRC Handbook of Chemistry and Physics, 85th Edition, CRC Press, 2004.

[255] R. Escobar Galindo, R. Gago, D. Duday, C. Palacio, Towards nanometric resolution in multilayer depth profiling: a comparative study of RBS, SIMS, XPS and GDOES, Anal. Bioanal. Chem. 396 (2010) 2725–2740. https://doi.org/10.1007/s00216-009-3339-y.

[256] A.J. Roberts, C.E. Moffitt, Trends in XPS instrumentation for industrial surface analysis and materials characterisation, J. Electron Spectrosc. Relat. Phenom. 231 (2019) 68–74. https://doi.org/10.1016/j.elspec.2018.03.002.

[257] E. Besozzi, D. Dellasega, V. Russo, C. Conti, M. Passoni, M.G. Beghi, Thermomechanical properties of amorphous metallic tungsten-oxygen and tungsten-oxide coatings, Mater. Des. 165 (2019) 107565. https://doi.org/10.1016/j.matdes.2018.107565.

[258] Synthesis, structural and mechanical characterization of sputtered tungsten oxide coatings, Thin Solid Films 510 (2006) 191–196. https://doi.org/10.1016/j.tsf.2005.12.299.

[259] K. Weller, Z.M. Wang, L.P.H. Jeurgens, E.J. Mittemeijer, Oxidation kinetics of amorphous AlxZr1−x alloys, Acta Mater. 103 (2016) 311–321. https://doi.org/10.1016/j.actamat.2015.09.039.

[260] Y. Xu, X. Liu, L. Gu, J. Wang, P. Schützendübe, Y. Huang, Y. Liu, Z. Wang, Natural oxidation of amorphous Cu Zr1- alloys, Appl. Surf. Sci. 457 (2018) 396–402. https://doi.org/10.1016/j.apsusc.2018.06.130.

[261] Y. Xu, Y. Chen, P. Schützendübe, S. Zhu, Y. Huang, Z. Ma, Y. Liu, Z. Wang, Thermal oxidation of amorphous Cu Zr1− alloys: Role of composition-dependent thermodynamic stability, Appl. Surf. Sci. 503 (2020) 144376. https://doi.org/10.1016/j.apsusc.2019.144376.

[262] D. Shin, Z.-K. Liu, Phase stability of hafnium oxide and zirconium oxide on silicon substrate, Scr. Mater. 57 (2007) 201–204. https://doi.org/10.1016/j.scriptamat.2007.04.011.

[263] R.-T. Qu, F.-F. Wu, Z.-F. Zhang, J. Eckert, Direct observations on the evolution of shear bands into cracks in metallic glass, J. Mater. Res. 24 (2009) 3130–3135. https://doi.org/10.1557/jmr.2009.0374.

[264] M.T. Asadi Khanouki, Temperature rise in shear bands and its effect on crystallization behavior in bulk metallic glasses, J. Alloys Compd. 936 (2023) 168198. https://doi.org/10.1016/j.jallcom.2022.168198.

[265] C. Xie, I. Milošev, F.U. Renner, A. Kokalj, P. Bruna, D. Crespo, Corrosion resistance of crystalline and amorphous CuZr alloys in NaCl aqueous environment and effect of corrosion inhibitors, J. Alloys Compd. 879 (2021) 160464. https://doi.org/10.1016/j.jallcom.2021.160464.

[266] W.H. Bragg, W.L. Bragg, The reflection of X-rays by crystals, Proc. R. Soc. Lond. Ser. Contain. Pap. Math. Phys. Character 88 (1997) 428–438. https://doi.org/10.1098/rspa.1913.0040.

[267] J.E. Chisholm, C. Hammond The Basics of Crystallography and Diffraction. International Union of Crystallography Texts on Crystallography, Oxford University Press, 1997. xi + 249 pp. Price £14.99 (Paperback) [Also available in hardback]. ISBN 0-19-855945-3., Mineral. Mag. 62 (1998) 131–131. https://doi.org/10.1180/002646198547422.

[268] G. Greczynski, L. Hultman, X-ray photoelectron spectroscopy: Towards reliable binding energy referencing, Prog. Mater. Sci. 107 (2020) 100591. https://doi.org/10.1016/j.pmatsci.2019.100591.

[269] A.K. Singh, Experimental Methodologies for the Characterization of Nanoparticles, in: Eng. Nanoparticles, Elsevier, 2016: pp. 125–170. https://doi.org/10.1016/B978-0-12-801406-6.00004-2.

[270] D.B. Williams, C.B. Carter, Transmission Electron Microscopy, Springer US, Boston, MA, 1996. https://doi.org/10.1007/978-1-4757-2519-3.

[271] Modern Raman Spectroscopy – A Practical Approach | Wiley Online Books, (n.d.). https://onlinelibrary.wiley.com/doi/book/10.1002/0470011831 (accessed April 19, 2023).

[272] S. Sinha Ray, Techniques for characterizing the structure and properties of polymer nanocomposites, in: Environ. Friendly Polym. Nanocomposites, Elsevier, 2013: pp. 74–88. https://doi.org/10.1533/9780857097828.1.74.

[273] G. Schitter, J. Steininger, F. Heuck, U. Staufer, Towards fast AFM-based nanometrology and nanomanufacturing, Int J Nanomanufacturing 8 (2012) 392–418. https://doi.org/10.1504/IJNM.2012.051109.

[274] F.D. Fischer, G. Reisner, E. Werner, K. Tanaka, G. Cailletaud, T. Antretter, A new view on transformation induced plasticity (TRIP), Int. J. Plast. 16 (2000) 723–748. https://doi.org/10.1016/S0749-6419(99)00078-9.

[275] M. ABBOUD, MICROMECHANICAL CHARACTERIZATION OF METALLIC GLASS — CRYSTALLINE NANOCOMPOSITE COATINGS, (n.d.). https://doi.org/10.1017/CBO9781107415324.004.

[276] M. Hardiman, T.J. Vaughan, C.T. McCarthy, A review of key developments and pertinent issues in nanoindentation testing of fibre reinforced plastic microstructures, Compos. Struct. 180 (2017) 782–798. https://doi.org/10.1016/j.compstruct.2017.08.004.

[277] S. Haratian, F.B. Grumsen, M. Villa, T.L. Christiansen, M.A.J. Somers, Surface hardening by gaseous oxidizing of (Zr55Cu30Al10Ni5)98Er2 bulk-metallic glass, J. Alloys Compd. 800 (2019) 456–461. https://doi.org/10.1016/j.jallcom.2019.06.042.

[278] X.P. Nie, X.H. Yang, L.Y. Chen, K.B. Yeap, K.Y. Zeng, D. Li, J.S. Pan, X.D. Wang, Q.P. Cao, S.Q. Ding, J.Z. Jiang, The effect of oxidation on the corrosion resistance and mechanical properties of a Zr-based metallic glass, Corros. Sci. 53 (2011) 3557–3565. https://doi.org/10.1016/j.corsci.2011.06.032.

Abbreviations list

MG: Metallic Glass

TFMG: Thin Film Metallic Glass

GFA: Glass Forming Ability

SB: Shear Band

T_g: Glass transition temperature

T_m: Melting temperature

STZ: Shear Transformation Zone

PVD: Physical vapor deposition

CVD: Chemical vapor deposition

MS: Magnetron Sputtering

RMS: Root Mean Square

SEM: Scanning electron microscopy

AFM: Atomic force spectroscopy

XRD: X-ray diffraction

TEM: Transmission Electron Microscope

SAED: Selected Area Electron Diffraction

EDXS: Energy Dispersive X-ray Spectroscopy

ERD: Elastic Recoil Detection

COF: Coefficient of Friction

DCM: Dynamic Contact Module

FWHM: Full Width at Half Maximum

List of publications

Journal articles

- **Bagherpour A**, Haye E, Moskovkin P, Lucas S. Vein pattern vs. columnar fracture shape in Cu-Zr thin film metallic glasses: Driving force and mechanism. Materialia. 2023 Sep 29:101914.
- **Bagherpour A**, Baral P, Colla MS, Orekhov A, Idrissi H, Haye E, Pardoen T, Lucas S. Tailoring Mechanical Properties of a-C:H:Cr Coatings. Coatings. 2023 Dec 14;13(12):2084.

Conference contributions

- Oral presentation entitled "Vein pattern vs. columnar fracture shape in Cu-Zr thin film metallic glasses: Driving force and mechanism", Namur, Belgium, NISM annual meeting, 2023
- Oral presentation entitled "Hydrogenated amorphous carbon (a-C:H) thin films deposited by low pressure plasma: study of the bias voltage and pressure dependencies of morphology and tensile behavior", Namur, Belgium, NISM annual meeting, 2020
- Oral presentation entitled "Dual-phase CuZr thin film metallic glasses (TFMGs) deposited by PVD magnetron sputtering: bias voltage and thickness dependency of structure, hardness, and wear resistance", Barcelona, Spain, SICT, 2021
- Poster presentation titled "Hydrogenated amorphous carbon (a-C:H) thin films deposited by lowpressure plasma: linking mechanical and fracture behavior to deposition conditions", Paris, France, SICT, 2021
- Poster presentation entitled "Surface Development for tomorrow's applications", Namur, Belgium, Institute day, 2021
- Poster presentation entitled "Dual-phase CuZr thin film metallic glasses (TFMGs) deposited by PVD magnetron sputtering: bias voltage and thickness dependency of structure, hardness, and wear resistance", Namur, Belgium, EFID, 2022
- Poster presentation entitled "Dual-phase CuZr thin film metallic glasses (TFMGs) deposited by PVD magnetron sputtering: bias voltage and thickness dependency of structure, hardness, and wear resistance", Namur, Belgium, NISM annual meeting, 2022

Poster presentation entitled "Dual-phase CuZr thin film metallic glasses (TFMGs) deposited by PVD magnetron sputtering: bias voltage and thickness dependency of structure, hardness, and wear resistance", Namur, Belgium, NANOWAL, 2023